Development and Characterization of Analytical Tools to Study Immunology Ex Vivo

Maura Comeau Belanger
Merrimack, New Hampshire

B.S. Chemistry, Roanoke College, 2014

A Dissertation presented to the Graduate Faculty of the University of Virginia in Candidacy for the Degree of Doctor of Philosophy

Department of Chemistry

University of Virginia
May 2020

ABSTRACT

Biological function is governed by well-defined chemical signals occurring with a high degree of spatial and temporal specificity. The field of bioanalytical chemistry is concerned with measuring these signals quantitatively. While simplifying the biological system to well-defined protein solutions, or cell cultures, allows for precise manipulation and detection, removing the signals from the tissue matrix also removes the biological context. *In vivo* measurements maintain the spatial distribution and other biological functions, such as fluid flow; however, they can be extremely complicated, often requiring genetic modifications. *Ex vivo* platforms maintain the spatial organization of *in vivo* while providing the increased experimental accessibility of *in vitro* studies. *Ex vivo* sections have been used to characterize functions of different tissues, including immune tissue.

Immunity is a highly dynamic and systemic process that is constantly working to clear the body of harmful pathogens. The immune system is generally separated into two components, the innate and adaptive responses. The innate response is immediate but non-specific, while the adaptive is slower but much more targeted. The success of the adaptive immune response is determined in a secondary immune organ, the lymph node. Measuring chemical signals within the lymph node tissue requires the development of novel analytical tools. **Chapter 2** describes the characterization of live lymph node tissue slices. These slices were viable and able to function as an acute culture platform to study immunological events. Lymph node slices processed whole-protein antigen and were able to respond to antigen challenge after vaccination. This work provided the platform that novel analytical tools were then developed for. **Chapters 3** and **4** are focused on these tools.

The work in **chapter 3** focuses on the development of a novel cell labelling reagent. Bright-blue polymer nanoparticles were generated in collaboration with the Fraser lab at UVA, and used to label phagocytic immune cells. The labelling did not affect cellular viability or function. The

bright-blue fluorescence allowed labelled cells to be easily distinguished from the tissue background for cell tracking. **Chapter 4** characterizes magnetic beads as an embedded platform for immunoassays. Beads were functionalized with model antibodies and polyethylene glycol (PEG) and delivered to lymph node slices. The addition of the PEG was critical to an even delivery of the beads within the tissue slices. The work in this dissertation focuses on setting the foundation for analytical measurements in lymph node tissue. In the future, we anticipate that these platforms will provide additional insight into immunological functions.

ACKNOWLEDGEMENTS

The work in this dissertation represents a labor of love and would not have been successful without the help of so many people. Firstly, I would like to thank my research advisor Dr. Rebecca Pompano. Being one of the first lab members and helping you set up the lab from scratch will always be a special opportunity that I wouldn't ever want to change. Working so closely with you to help direct the first wave of research within the lab was an incredible experience that I never thought I would get in graduate school. You were always willing to allow the research to flow and change as I learned what I was interested in, and what I was good at. Your enthusiasm for our science and your unwavering support made me excited to come into work. You have made me into a better scientist by improving my experimental design and communication skills. I would not be the scientist I am today without your guidance and support. Thank you for making these past 6 years some of the most memorable of my life.

I have had the distinct pleasure of working with many talented people as they come through the lab. Everyone who has come into the lab during my time has helped me to improve and are truly wonderful people doing excellent science. There are a few people who I would like to thank specifically. Dr. Ashley Ross was our first post doc and someone I consider a close friend. Ashely, your support and insight were always welcome and I appreciate all your help in navigating the chemistry department during my first years here. I have acted as a mentor to a number of undergraduates as they begin their research careers. A special thank you to Jacob Woodroof, Benjamin Groff, Drake Dixon, and Kristen Richey for their dedication and working with me as I learned how to mentor effectively. Megan Catterton has often acted as my better half in lab. You were always there when I needed to talk through my experiments, or needed a second set of eyes or hands in lab. You are one of my best friends and I cannot thank you enough for all your help, love, and support. Thank you so much for being my lab husband and making my time here that much richer.

Life outside of lab would have been much duller without the friends I have made both in Charlottesville and beyond. My friends were always ready to explore and try new things. Many a night was spent on a volleyball court or around a board game table. Likewise, weekends could be spent exploring central Virginia, or simply relaxing on the river. A special thank you to Dr. Elizabeth Duselis. I would not have survived my first years of graduate school without you. You always helped keep me grounded and are a constant source of inspiration with your hard work and dedication to everything you do. Those late-night discussions were so special to me and I want to thank you for all that you do.

Lastly, I'd like to take a moment to thank my family. My mom and dad are always so supportive of my goals and have been with me through this entire journey. While they haven't always understood the science behind what I am doing they have always had the utmost faith in my abilities, even when I didn't. My brother is always there to make me laugh, sometimes unintentionally. Additionally, my chosen family has been with me every step of the way. Some of these people have been with me through most of my life, while others are new additions. Each of them has helped me become the person I am today and I know I can count on their help through thick and thin.

Everyone I have had the pleasure of working and growing with during my last 6 years has made an impact on my life, and I hope I have influenced them for the better as well. My time at graduate school was so different from what I imagined I would be doing but; I wouldn't change it for the world.

TABLE OF CONTENTS

TABLE OF FIGURES

TABLE OF TABLES

1 INTRODUCTION

1.1 BIOANALYTICAL CHEMISTRY IN TISSUE

Spatial organization drives biological function; from embryonic development, including tissue organization, to systemic functions, such as immunity or endocrine signaling. Cells and molecules are meticulously arranged and communicate with strict temporal resolution. Quantifying the distribution of analytes within tissue remains a large challenge for the bioanalytical community. Classic methods in analytical chemistry were designed to characterize well-mixed aqueous solutions. In bioanalytical chemistry samples are often simplified, either by tissue homogenization or separation into component parts (e.g. cell supernatants and body fluid fractions) to facilitate the use of traditional analytical methods. However, as the field of bioanalytical chemistry expands our understanding of biology, it is clear that measurements within the tissue matrix are more meaningful than those collected with reductive or over-simplified methods.

Researchers studying complex biological systems often begin with simplified versions, such as proteins in aqueous solutions or well-developed cell cultures. Difficulties arise when moving towards measuring the intended analyte in its biological context. This transition can be outside the scope for more traditional chemistry and engineering labs, and its success is often determined by specific need-driven collaborations. Many chemical and physical scientists mimic *in vivo* conditions by fabricating *ex vivo* platforms, such as 3D hydrogels or other biofabrication scaffolds.[1–3] Many biomedical researchers are not prepared to fabricate these constructs, instead their experimental models often begin with more biologically complex platforms, such as *in vivo* systems or tissue sections.[4–6] This can make the translation from one collaborator to another difficult; highlighting the need for easily translatable methods to quantitatively analyze complex biological systems, to provide the clearest view of relevant functions.

Measuring analytes within intact tissue samples provides several advantages. The high cell density maintained in tissue maximizes the local concentration of analytes and can preserve density-dependent cell behavior.[7] Preserving the spatial organization that occurs *in vivo* also preserves natural cell-to-cell contacts and interactions with the extracellular matrix that are disrupted when homogenizing the tissue.[8,9] Additionally, rare cell types are persevered in intact tissue samples, as these cells are often lost during tissue dissociation. Studying dendritic cells from spleen tissue *in vitro* requires isolating a population that is less than 2% of all splenocytes, requiring sample enrichment or pooling across multiple animals.[10] These advantages allow intact tissue platforms to provide a more complete insight into the biological function of the tissue.

Intact tissue samples add to the complexity of analytical measurements. The extracellular matrix can hinder diffusion and increase the potential for off-target interactions. Researchers have attempted to limit the effects of a complex culture environment and extracellular matrix effects, while maintaining spatial organization, by analyzing thin slices of fixed tissue. The tissue is submerged in a fixative solution, resulting in cross-linked proteins which preserves the spatial organization for many years.[11–13] Fixed tissues are then embedded in wax and sliced to thicknesses of only a few microns. The fixed tissue does not require supplemented media, and the thin slices decrease treatment diffusion times through the sample, and minimize off-target binding effects. These slices however, cannot report on dynamic processes, as the tissue is non-functional.

The analysis of living tissue adds to the depth of the information available to researchers but adds to the complexity of the experimental system as well. Both *in vivo* and *ex vivo* methods must keep tissue samples alive, and as such they require optimized conditions to maximize viability and function. Parameters to consider when moving to live tissue platforms include: nutrient supplementation, temperature and gas composition. Nutrient supplementation can introduce unwanted interactions. Many medias are supplemented with serum proteins which can contain

proteases which would degrade other proteins in solution.[14] Controlling temperature and gas composition can complicate the experimental set-up compared to samples on a slide. However, live tissue systems allow for the observation of transient events such as protein-protein interactions with immunosensors, or cell-cell interactions guiding axon development in the brain.[15–17] Real-time monitoring of a single sample adds temporal context to the spatial. Assays using repeated-measures have been applied to live tissue samples including heart, and lymph node.[18,19]

Here I focus on developing analytical tools to study the immune system. Immunity is a highly dynamic and intricate process that occurs throughout the body. Many immunologists study immunity at peripheral sites, often focusing on the tumor microenvironment, the gut, the lungs, etc. However events within the lymph node, the main secondary organ of the immune system, dictate the effectiveness of the adaptive immune response.[20] Only a small subset of immunologists look in-depth into the functionality of the lymph node specifically. Many others measure incoming signals from peripheral sites or signals as they exit the lymph node, trafficking to the periphery. Therefore, the toolbox available to those interested in studying lymph node dynamics is currently limited. I am interested in measuring these interactions within the lymph node to gain a deeper understanding of how effective adaptive immune responses are generated, especially at the early stages.

1.2 Adaptive Immunity

The immune response can be broken down into two main components, the innate and the adaptive. The innate response is crucial within the first hours of exposure to an immunogenic stimulant. This response is not pathogen-specific and relies on the recognition of conserved motifs to initiate activation.[21,22] Activation of the innate response is required to start the adaptive response.[23] In contrast, the adaptive response is much slower to respond, often taking several days to reach its peak.[24] An adaptive immune response is highly specific to the pathogen that

initiated it.[25] The memory associated with an adaptive immune response means that a response to the same pathogen can be mounted much more quickly, resulting in more efficient elimination of the pathogen. Both the innate and adaptive immune responses are required for pathogen clearance and work together to prevent harmful infections.

1.2.1 The lymph node

The lymph node is a secondary organ of the immune system where much of the adaptive immune response is generated (Figure 1.1).[20,26,27] There are many lymph nodes found throughout an organism that work in combination, both with each other and circulating immune cells to fight infections.

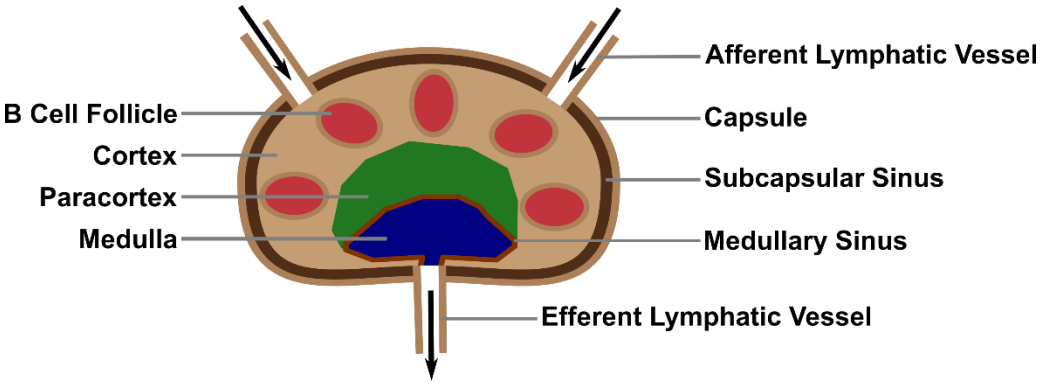

Figure 1.1: Schematic representation of the lymph node. Supporting stromal networks are found throughout the node. Macrophages and dendritic cells are found associated with the sinuses (subcapsular and medullary). Macrophages are also densely populated within the medulla and dendritic cells are distributed throughout. B cells are confined to the follicles and T cells are found mainly in the paracortex region. Fluid flows in through the afferent vessels and out by the efferent vessel in one direction.

The outside of the lymph node is surrounded by a collagenous capsule that provides structure, as well as a barrier to the outside of the body.[20] Both blood and lymphatic vessels are present to allow cells to enter and exit the lymph node to initiate and fulfill an immune response. Once within the lymph node fluid can flow through associated sinuses, such as the subcapsular sinus and the medullary sinus.

There are macrophages and dendritic cells (DCs) associated with these sinuses that scavenge any large particulate matter.[28–30] DCs are also interspersed within the body of the

node.[28] In the cortex the DCs provide support for the B cell follicles, which are located generally around the outside edge of the node.[31,32] The space in between the follicles allows for interactions between DCs, B cells and T cells.

The interior paracortex of the node is mainly populated by T cells and DCs and is where T cell activation can occur within the lymph node.[20,33] The final component of the lymph node is the medulla, which is a dense area of macrophages.[34] Throughout all of this structure there is a supporting network of stromal cells that can also play a key role in modulating an immune response.[35–37] All of these cell types work in connection with one another to generate an immune response such as the one detailed below.

1.2.2 The immune response

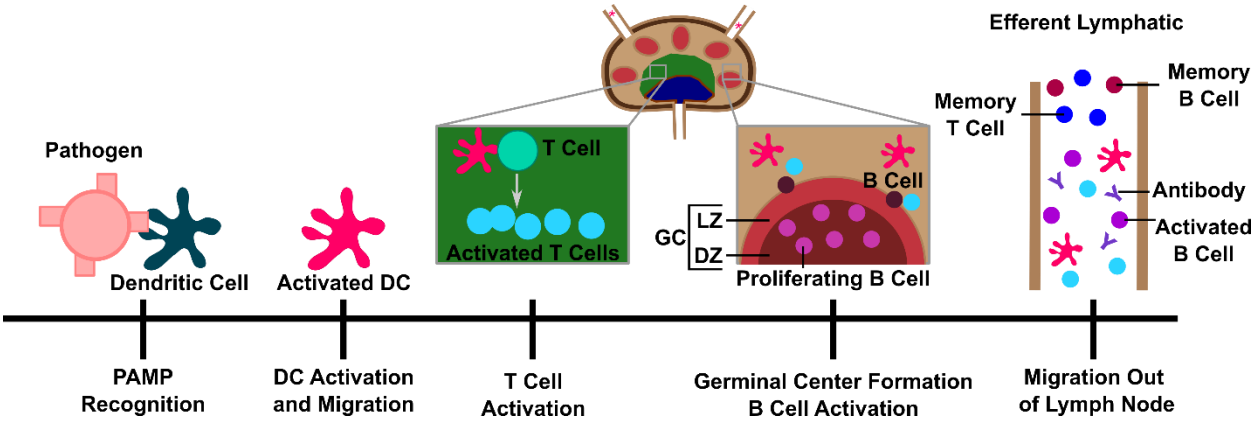

Figure 1.2: Schematic representation of an immune response. The response is begun in the periphery with recognition of pathogen-associated molecular patterns (PAMPs) by innate immune cells and dendritic cells. The dendritic cells then become activated and migrate to the lymph node through the afferent lymphatic vessels. There they interact with T cells to activate them. T cells can then become polarized and some will interact with B cells. The B cells will then become active and begin to generate a germinal center (GC). In the dark zone (DZ) of the germinal center B cells will proliferate and undergo somatic hypermutation. In the light zone (LZ) they interact with follicular helper T cells and follicular dendritic cells to move through affinity maturation. Activated DCs, T cells, and B cells and soluble antibodies can leave the lymph node to circulate throughout the body. Later in the immune response memory T and B cells can exit to populate other tissues such as the bone marrow.

In order to fully capture the dynamic and intricate nature of an immune response I will walk through a reaction to an inflammatory pathogen such as *E. coli* (Figure 1.2). Inflammatory pathogens are often recognized by certain molecular patterns on their surfaces (pathogen-associated molecular patterns, PAMPs).[26] Some canonical PAMPs include the peptidoglycan

layer of many bacterial species and lipopolysaccharide (LPS).[38,39] After recognition of the PAMPs by innate immune cells there is a massive recruitment of cells to the infected tissue.[22] This includes DCs which phagocytose (uptake) parts of the pathogen and process it for presentation to T cells.[40,41] Upon processing an immunogenic agent DCs become active and migrate throughout the body to nearby lymph nodes.[42] These activated DCs then present antigen to the T cells that populate the lymph node.[43–45]

DCs can interact with both CD8+ and CD4+ T cells, but here I will focus on CD4+-mediated immune responses.[41] Each T cell recognizes a specific peptide sequence through each cells' specific T cell receptor (TCR) and upon recognition of that sequence the T cell becomes activated, and will proliferate explosively (Figure 1.3).[46] During this proliferation the lymph node can expand and appear swollen. During T cell activation, depending on secondary and tertiary signals from surrounding cells, the T cell will polarize to various types of helper T cells.[47,48] These T cell types are characterized by the cytokines that they secrete and can be, generally, associated with different disease types.[49]

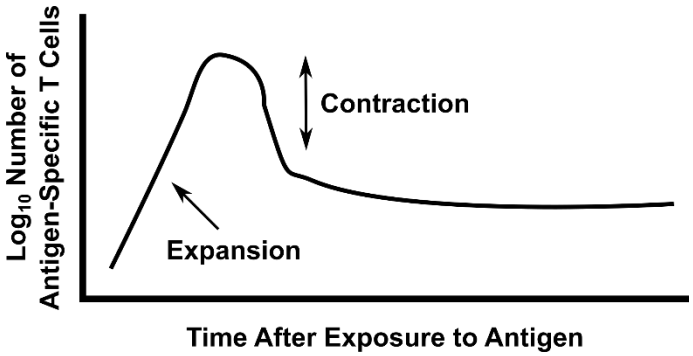

Figure 1.3: Representation of T cell expansion after recognition of specific antigen. The contraction phase does not return to baseline due to memory formation.

Some T cells exit the lymph node and traffic to the site of infection to facilitate immediate clearance of the pathogen, however others remain in the lymph node and interact with B cells. In the case of antibody-mediated immune responses (humoral immunity), B cells become activated through interactions with specialized T cells called follicular helper T cells.[50,51] These T cells, as the name suggests, help the cells in the B cell follicle to promote germinal center production. All naïve lymph nodes have B cell follicles but upon activation these follicles can mature into germinal centers.[20]

Each B cell generates a single clone of an antibody, so in order to mount an effective antibody-mediated response that B cell must proliferate very quickly.[26,27] This expansion causes the germinal center to distinguish itself into two zones, a light zone and a dark zone; so called based on their ability to scatter light through traditional contrast microscopy methods.[52,53] The dark zone lies in the middle of the germinal center and is where most of the proliferation and gene rearrangement occurs.[53] The light zone is around the outside and is where antibody affinity for the antigen is tested, to ensure that the most effective antibody is made in response to the antigen.[53] Through random gene rearrangements, antibody sequences can change and based on their relative affinity for the antigen the cells displaying that sequence will either proliferate or apoptose.[54] Antibodies produced by these B cells, as well as mature B cells themselves, can then leave the lymph node and traffic to the site of infection to aid in the immune response.[24]

After the initial response to a new antigen the immune system generates memory cells that can reside in the infected tissue, the lymph node, or the bone marrow.[55–58] These memory cells are then able to mount a secondary response to the same antigen much quicker and clear the infection faster (Figure 1.4). That is why vaccines are so important to generating immunity, as the initial response is introduced in a way that does not cause the host lasting harm.

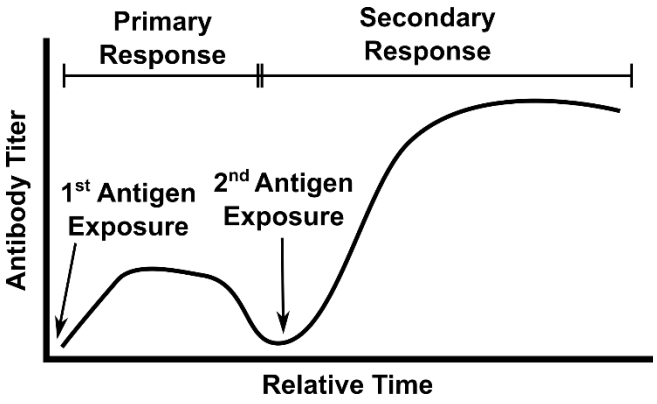

Figure 1.4: Representation of antibody titer during an immune response. The first exposure to antigen generates a modest response but the second exposure generates a much larger response much quicker.

As illustrated in the above example immunity is a systemic phenomenon. This can make it difficult to experimentally access the entire response outside of systemic read-outs, such as survival studies. This illustrates the need for tools that help expand our understanding of immunity as it occurs throughout the body. The developed techniques often focus on one small aspect of

an immune response to gain a very deep understanding, which is helpful in the determination of each step of an immune response. A completely ex vivo immune response has not yet been described but with the advent of many new technologies, including microfluidics, this could be on the horizon.

1.3 Traditional Analytical Methods for Immunology

An immune response such as the one described above has been elucidated by a combination of *in vivo* and *in vitro* assays. *Ex vivo* experimental platforms are less common but can include measurements in thin, fixed tissue sections as well as whole-lymph node explants. Each set of assays provides distinct and important information that is required to provide a complete picture of the immune response.

1.3.1 In vitro assays

An immunoassay requires the use of both an antigen and an antibody to measure concentration.[59] The high specificity of antibodies makes them perfect candidates for sandwich assays, like Enzyme-Linked Immunosorbent Assays (ELISA), as different clones can target different epitopes on the same antigen.[60,61] Briefly, ELISAs work by coating a surface with one antibody clone and introducing the analyte of interest. A second antibody that is specific to a different area of the antigen is used and an enzyme is added and used to induce a color change that is

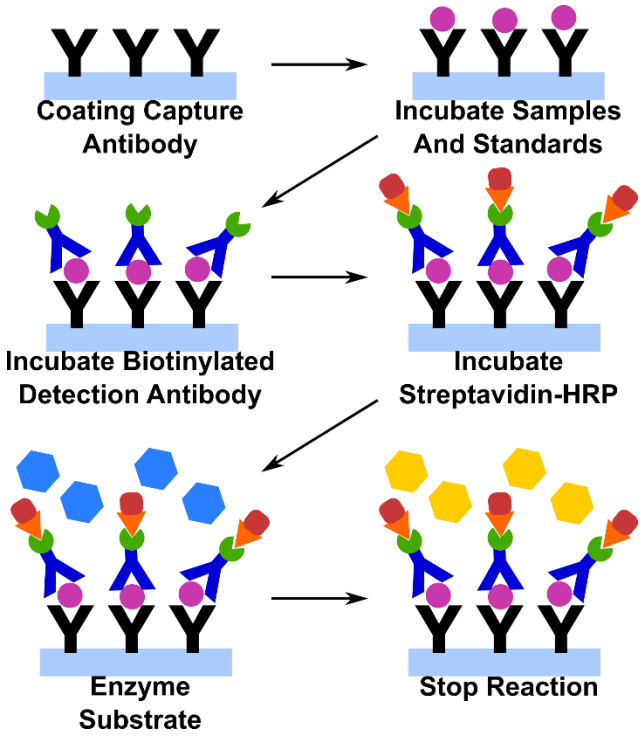

Figure 1.5: Schematic representation of an ELISA. This step-wise sandwich assay will report substrate concentration as a function of absorbance.

relative to the concentration of analyte. This can then be related back to a standard curve to get an absolute concentration (Figure 1.5).

Immunoassay sensitivity and limit of detection is often dictated by the antibody pairs, meaning that consistency is key when reproducing these assays. The time that the enzyme is allowed to interact with its substrate can also vary the signal greatly, so each plate requires its own standard curve. This makes comparisons across multiple plates difficult if the signal is close to the limit of detection for that specific plate. However, these assays are very powerful and provide excellent quantitative measurements of secreted molecules.

Flow cytometry is a technique that allows for the collection of a large amount of data, compared to microscopy. Many flow cytometers utilize sheath flow to focus the sample into a single line of cells, allowing for many cells to be analyzed quickly.[62] Flow cytometry utilizes laser-based excitation and separated detectors to extend the range of fluorophores available to interrogate the state of each cell as it passes by the laser (Figure 1.6). Many standard fluorescent microscopes are comprised of matched excitation and emission filters, limiting their ability to measure many fluorophores at the same time.

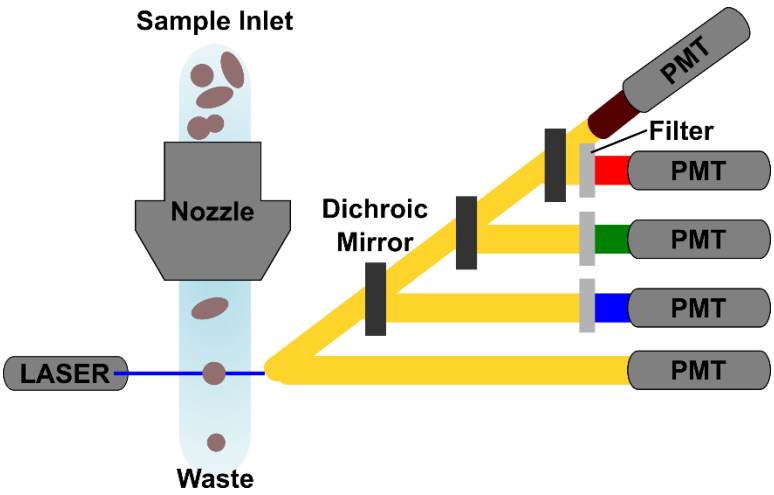

Figure 1.6: Schematic representation of flow cytometry. Samples flow through a focusing nozzle past a laser. Fluorescent signal is then directed to a variety of photo-multiplier tubes (PMTs). Each PMT is separated by a dichroic mirror and then a filter ensures each PMT is spectrally distinct. From this set-up four emission signals can be measured from a single excitation source. The additional PMT parallel to the laser collects light scatter data to inform on cell size and complexity.

Flow cytometers can have multiple lasers and detectors set-up in distinct patterns to allow up to 32 different parameters to be measured. However, this technique does not generally provide spatially relevant information, and those instruments that do require extensive sample preparation.[63]

Flow cytometry can also be used with fixed and permeabilized samples to determine the exact cell types producing a certain cytokine.[64] Cells are blocked from secreting the cytokine and then fixed, permeabilized and stained. Through the addition of cell-surface markers the exact surface phenotype of cells producing large amounts of cytokine during the response can be determined. This same process can be applied to other internal protein markers including transcription factors. Often T cells can have similar surface markers but are expressing different transcription factors that help differentiate their polarizations during the course of an immune response.[65]

Analysis of bulk cell cultures can also include analysis of gene expression. Often this is done through quantitative reverse transcriptase polymerase chain reaction (RT-qPCR).[66] RT-qPCR can give relative quantitative data regarding which genes are being expressed within the cell culture. After comparison to a standardized housekeeping gene the relative expression of a gene can be compared across samples. These techniques do require extensive preparation as well as expensive reagents. In order to get enough data to be statistically powerful these experiments can quickly become specialized interests.

1.3.2 In vivo assays

A second approach to immunology is to use *in vivo* models to study disease progression and cellular dynamics. To image cell dynamics and cell-cell interactions two-photon microscopy is often utilized.[67,68] Two-photon experiments have investigated antigen draining,[69] cell trafficking,[70,71] and cellular interactions[72,73] to and within the lymph node. Often these studies occur on skin-draining lymph nodes such as the popliteal node, located near the knee of the mouse.

This node offers great experimental accessibility due to its ease of exposure and small size.[74] In addition, all antigens injected into the footpad of the mouse drain directly to this lymph node reducing off-target transport events.[75] Footpad injections have become highly regulated due to the high risk of the mouse experiencing extreme discomfort.

Many vaccine-efficacy experiments investigate the levels of antibodies circulating within the organism after vaccine treatment.[76] This is done through whole-blood antibody titers. Briefly, blood is collected and serum proteins are separated by centrifugation. The protein fraction can then be tested through a modified ELISA to measure the concentration of a specific antibody.

Depending on the pathogen used the whole pathogenic load can also be investigated.[77] Organs or blood can be analyzed for viral,[78] bacterial,[79,80] or parasite[81,82] load to analyze the ability of the immune system to clear the pathogen from the body. Alternatively, whole-animal survival studies can test the ability of the immune system to clear infections and cancers.[83,84] In this set-up animals are either treated with the potential therapeutic or a vehicle control and infected with the target disease.[85] The survival of the animals is tracked over time and if the immune system can effectively clear the disease the animal survives.

1.3.3 Thin fixed slices

Basic lymph node biology was first understood with the use of thin slices of fixed tissue.[33] During the fixation process proteins are cross-linked to prevent movement of species within the tissue.[12,86] However this process can change protein structure and cause certain targets to be unrecognizable to certain antibody clones.[86,87] Fixation allows the tissue to be embedded in paraffin wax and sliced into very thin sections (10 μm) without structural damage.[13] Tissue can also be frozen to achieve a similar effect. Tissue slices can then be labeled with antibodies or other specific stains to determine distinct areas. Utilizing thin slices has allowed researchers to discover the elegant organization of the lymph node.

Even beyond the larger structures such as B cell follicles and the medulla, the dendritic cells also exhibit extensive organization.[28] By collecting slices at different times, researchers have been able to visualize distinct structural changes throughout the tissue.[88,89] Fixed and permeabilized samples have been used to look at the internal environment of the cells by staining for internal cytokines.[90] However, as the tissue is non-functioning, these slices cannot inform on dynamic biological processes. Many of the analytical assays and imaging tools we use regularly are inspired by early studies in thin tissue slices; including our own published method for immunostaining live tissue.[19]

1.3.4 Ex vivo assays

Immunological dynamics are of increasing interest to many research groups. Whole lymph node explants have been used in addition to live intra-vital imaging, providing a complex *ex vivo* system.[91,92] Slices of murine thymus tissue have also been used to monitor the dynamics of T cell development.[93] Lymphocyte viability and cytokine expression has been characterized in blocks of human tonsil tissue as a platform to study human immunity.[94] We have been able to capture similarly dynamic processes within lymph node slices, such as the transient expression of CD69 an activation marker on T cells.[19,95]

Working with *ex vivo* samples also provides an alternative route to the interior of the organ, compared to drainage. Stimulants or additional cell types can be added directly to the sample providing limited transport effects. This also allows for accurate dosing to be measured during experimental procedures. As with *in vitro* experiments *ex vivo* samples are exposed to the whole dose of experimental analyte. Dose-response relationships can be more accurately examined as the exact concentration of the stimulant is known and analyte concentration can be determined. Tissue sections allow for the added benefit of dosing directly to deep tissue areas that are excluded from intravital imaging due to their physical location.

It has been shown previously that cells overlaid on lymph node slices will home to areas of similar cell types.[93,96] Further investigation of the dynamics of an immune response, requires high-resolution microscopy to visualize individual cells within the tissue.[97] With fluorescent microscopy there is a risk of harming biological samples through phototoxicity in both high- and low-resolution imaging set-ups.[68,98,99] By removing the tissue from the animal, sample size can be increased without increasing the number of animals required for a given experiment.

1.4 Concluding Remarks

New immunological studies are constantly bringing to light the dynamic and regulated nature of immunity. With this understanding it is crucial to determine integral signals that lead to an effective adaptive immune response with a high degree of precision. Many of the established analytical methods used to study immunity are either highly reductive or highly complex. A biologically complex, experimentally accessible middle ground is becoming increasingly necessary. Existing analytical tools have not been characterized within this middle ground and will require extensive optimization to produce meaningful results; in some cases, new tools will need to be developed. This thesis will focus on the foundational work associated with developing novel analytical tools to study immunity within the lymph node.

Chapter 2 will describe the set-up of the lymph node slice platform. This acts as the foundation for many of the studies done in the Pompano lab. **Chapter 3** will detail a novel cell imaging technique which was achieved in collaboration with the Fraser lab. **Chapter 4** introduces a magnetic bead-based platform that can be used in future assay development. I will then conclude with a discussion of the impact and potential future work for these projects in **Chapter 5**.

1.5 REFERENCES

1 Tibbitt MW, Anseth KS. Hydrogels as extracellular matrix mimics for 3D cell culture. *Biotechnol Bioeng* 2009; **103**: 655–663.

2 Groll J, Boland T, Blunk T, Burdick JA, Cho D-W, Dalton PD *et al.* Biofabrication: reappraising the definition of an evolving field. *Biofabrication* 2016; **8**: 013001.

3 Ouyang L, Highley CB, Sun W, Burdick JA. A generalizable strategy for the 3D bioprinting of hydrogels from nonviscous photo-crosslinkable inks. *Adv Mater* 2017; **29**: 1604983.

4 Olinga P, Schuppan D. Precision-cut liver slices: A tool to model the liver ex vivo. *J Hepatol* 2013; **58**: 1252–1253.

5 Delmotte P, Sanderson MJ. Ciliary beat frequency is maintained at a maximal rate in the small airways of mouse lung slices. *Am J Respir Cell Mol Biol* 2006; **35**: 110–117.

6 Koerner JF, Cotman CW. A microperfusion chamber for brain slice pharmacology. *J Neurosci Methods* 1983; **7**: 243–251.

7 Hiscock TW, Miesfeld JB, Mosaliganti KR, Link BA, Megason SG. Feedback between tissue packing and neurogenesis in the zebrafish neural tube. *Development* 2018; **145**: dev157040.

8 Vaday GG, Lider O. Extracellular matrix moieties, cytokines, and enzymes: dynamic effects on immune cell behavior and inflammation. *J Leukoc Biol* 2000; **67**: 149–159.

9 Keller PJ, Ahrens MB. Visualizing whole-brain activity and development at the single-cell level using light-sheet microscopy. *Neuron* 2015; **85**: 462–483.

10 Duriancik DM, Hoag KA. The identification and enumeration of dendritic cell populations from individual mouse spleen and Peyer's patches using flow cytometric analysis. *Cytometry A* 2009; **75A**: 951–959.

11 Balgley BM, Guo T, Zhao K, Fang X, Tavassoli FA, Lee CS. Evaluation of archival time on shotgun proteomics of formalin-fixed and paraffin-embedded tissues. *J Proteome Res* 2009; **8**: 917–925.

12 Bachman J. Chapter Thirteen - Immunohistochemistry on freely floating fixed tissue sections. In: Lorsch J (ed). *Methods in Enzymology*. Academic Press, 2013, pp 207–215.

13 Kokkat TJ, Patel MS, McGarvey D, LiVolsi VA, Baloch ZW. Archived formalin-fixed paraffin-embedded (FFPE) blocks: A valuable underexploited resource for extraction of DNA, RNA, and protein. *Biopreservation Biobanking* 2013; **11**: 101–106.

14 Zheng X, Baker H, Hancock WS, Fawaz F, McCaman M, Pungor E. Proteomic analysis for the assessment of different lots of fetal bovine serum as a raw material for cell culture. Part IV. Application of proteomics to the manufacture of biological drugs. *Biotechnol Prog* 2006; **22**: 1294–1300.

15 Chao DL, Ma L, Shen K. Transient cell-cell interactions in neural circuit formation. *Nat Rev Neurosci* 2009; **10**: 262–271.

16 Prieto GA, Cotman CW. Cytokines and cytokine networks target neurons to modulate long-term potentiation. *Cytokine Growth Factor Rev* 2017; **34**: 27–33.

17 Murphy TW, Zhang Q, Naler LB, Ma S, Lu C. Recent advances in the use of microfluidic technologies for single cell analysis. *The Analyst* 2018; **143**: 60–80.

18 Wang K, Lee P, Mirams GR, Sarathchandra P, Borg TK, Gavaghan DJ *et al.* Cardiac tissue slices: preparation, handling, and successful optical mapping. *Am J Physiol Heart Circ Physiol* 2015; **308**: H1112-1125.

19 Groff BD, Kinman AWL, Woodroof JF, Pompano RR. Immunofluorescence staining of live lymph node tissue slices. *J Immunol Methods* 2018. doi:10.1016/j.jim.2018.10.010.

20 Grant SM, Lou M, Yao L, Germain RN, Radtke AJ. The lymph node at a glance – how spatial organization optimizes the immune response. *J Cell Sci* 2020; **133**. doi:10.1242/jcs.241828.

21 Alberts B, Johnson A, Lewis J, Raff M, Roberts K, Walter P. Innate Immunity. *Mol Biol Cell 4th Ed* 2002.https://www.ncbi.nlm.nih.gov/books/NBK26846/ (accessed 4 Apr2020).

22 Mogensen TH. Pathogen recognition and inflammatory signaling in innate immune defenses. *Clin Microbiol Rev* 2009; **22**: 240–273.

23 Iwasaki A, Medzhitov R. Control of adaptive immunity by the innate immune system. *Nat Immunol* 2015; **16**: 343–353.

24 Merlo LMF, Mandik-Nayak L. Chapter 3 - Adaptive immunity: B cells and antibodies. In: Prendergast GC, Jaffee EM (eds). *Cancer Immunotherapy (Second Edition)*. Academic Press: San Diego, 2013, pp 25–40.

25 Alberts B, Johnson A, Lewis J, Raff M, Roberts K, Walter P. The adaptive immune system. *Mol Biol Cell 4th Ed* 2002.https://www.ncbi.nlm.nih.gov/books/NBK21070/ (accessed 4 Apr2020).

26 Sompayrac L. *How the immune system works*. Fifth edition. John Wiley & Sons, Ltd: Chichester, West Sussex ; Ames, Iowa, 2016.

27 Murphy K, Travers P, Walport M, Janeway C. *Janeway's immunobiology*. 8th ed. Garland Science: New York, 2012.

28 Gerner MY, Kastenmuller W, Ifrim I, Kabat J, Germain RN. Histo-Cytometry: A method for highly multiplex quantitative tissue imaging analysis applied to dendritic cell subset microanatomy in lymph nodes. *Immunity* 2012; **37**: 364–376.

29 Junt T, Moseman EA, Iannacone M, Massberg S, Lang PA, Boes M *et al.* Subcapsular sinus macrophages in lymph nodes clear lymph-borne viruses and present them to antiviral B cells. *Nature* 2007; **450**: 110–114.

30 Bellomo A, Gentek R, Bajénoff M, Baratin M. Lymph node macrophages: Scavengers, immune sentinels and trophic effectors. *Cell Immunol* 2018; **330**: 168–174.

31 Allen CDC, Cyster JG. Follicular dendritic cell networks of primary follicles and germinal centers: phenotype and function. *Semin Immunol* 2008; **20**: 14–25.

32 Parmentier HK, Linden J a. VD, Krijen J, Wichen DFV, Rademakers LHPM, Bloem AC *et al.* Human follicular dendritic cells: Isolation and characteristics in situ and in suspension. *Scand J Immunol* 1991; **33**: 441–452.

33 Garside P. Visualization of specific B and T lymphocyte interactions in the lymph node. *Science* 1998; **281**: 96–99.

34 Gray EE, Cyster JG. Lymph node macrophages. *J Innate Immun* 2012; **4**: 424–436.

35 Chang JE, Turley SJ. Stromal infrastructure of the lymph node and coordination of immunity. *Trends Immunol* 2015; **36**: 30–39.

36 Mueller SN, Germain RN. Stromal cell contributions to the homeostasis and functionality of the immune system. *Nat Rev Immunol* 2009; **9**: 618–629.

37 Bajénoff M, Egen J, Koo LY, Laugier JP, Brau F, Glaichenhaus N *et al.* Stromal cell networks regulate lymphocyte entry, migration, and territoriality in lymph nodes. *Immunity* 2006; **25**: 989–1001.

38 Poltorak A. Defective LPS Signaling in C3H/HeJ and C57BL/10ScCr mice: Mutations in Tlr4 gene. *Science* 1998; **282**: 2085–2088.

39 Janeway CA. Approaching the asymptote? Evolution and revolution in immunology. *Cold Spring Harb Symp Quant Biol* 1989; **54**: 1–13.

40 Savina A, Amigorena S. Phagocytosis and antigen presentation in dendritic cells. *Immunol Rev* 2007; **219**: 143–156.

41 Steinman RM, Hemmi H. Dendritic cells: Translating innate to adaptive Immunity. In: Pulendran B, Ahmed R (eds). *From Innate Immunity to Immunological Memory*. Springer Berlin Heidelberg, 2006, pp 17–58.

42 Martín-Fontecha A, Sebastiani S, Höpken UE, Uguccioni M, Lipp M, Lanzavecchia A *et al.* Regulation of dendritic cell migration to the draining lymph node. *J Exp Med* 2003; **198**: 615–621.

43 Shakhar G, Lindquist RL, Skokos D, Dudziak D, Huang JH, Nussenzweig MC *et al.* Stable T cell-dendritic cell interactions precede the development of both tolerance and immunity in vivo. *Nat Immunol* 2005; **6**: 707–714.

44 Mempel TR, Henrickson SE, von Andrian UH. T-cell priming by dendritic cells in lymph nodes occurs in three distinct phases. *Nature* 2004; **427**: 154–159.

45 Stoll S, Delon J, Brotz TM, Germain RN. Dynamic imaging of T cell-dendritic cell interactions in lymph nodes. *Science* 2002; **296**: 1873–1876.

46 Lanzavecchia A, Iezzi G, Viola A. From TCR engagement to T cell activation. *Cell* 1999; **96**: 1–4.

47 Martinez-Sanchez ME, Huerta L, Alvarez-Buylla ER, Villarreal Luján C. Role of cytokine combinations on CD4+ T cell differentiation, partial polarization, and plasticity: Continuous network modeling approach. *Front Physiol* 2018; **9**. doi:10.3389/fphys.2018.00877.

48 Swain SL. T-cell subsets: Who does the polarizing? *Curr Biol* 1995; **5**: 849–851.

49 Cameron SB, Stolte EH, Chow AW, Savelkoul HFJ. T helper cell polarisation as a measure of the maturation of the immune response. *Mediators Inflamm* 2003; **12**: 285–292.

50 Vinuesa CG, Linterman MA, Yu D, MacLennan ICM. Follicular helper T cells. *Annu Rev Immunol* 2016; **34**: 335–368.

51 Crotty S. T follicular helper cell differentiation, function, and roles in disease. *Immunity* 2014; **41**: 529–542.

52 Allen CD, Okada T, Cyster JG. Germinal center organization and cellular dynamics. *Immunity* 2007; **27**: 190–202.

53 MacLennan IC. Germinal centers. *Annu Rev Immunol* 1994; **12**: 117–139.

54 Mishra AK, Mariuzza RA. Insights into the structural basis of antibody affinity maturation from next-generation sequencing. *Front Immunol* 2018; **9**. doi:10.3389/fimmu.2018.00117.

55 Sallusto F, Geginat J, Lanzavecchia A. Central memory and effector memory T cell subsets: function, generation, and maintenance. *Annu Rev Immunol* 2004; **22**: 745–763.

56 Kurosaki T, Kometani K, Ise W. Memory B cells. *Nat Rev Immunol* 2015; **15**: 149–159.

57 Steinbach K, Vincenti I, Merkler D. Resident-Memory T Cells in tissue-restricted immune responses: For better or worse? *Front Immunol* 2018; **9**. doi:10.3389/fimmu.2018.02827.

58 Xing Z, Afkhami S, Bavananthasivam J, Fritz DK, D'Agostino MR, Vaseghi-Shanjani M *et al.* Innate immune memory of tissue-resident macrophages and trained innate immunity: Re-vamping vaccine concept and strategies. *J Leukoc Biol* 2020. doi:10.1002/JLB.4MR0220-446R.

59 Darwish IA. Immunoassay methods and their applications in pharmaceutical analysis: Basic methodology and recent advances. *Int J Biomed Sci IJBS* 2006; **2**: 217–235.

60 The enzyme-linked immunosorbent assay (ELISA). *Bull World Health Organ* 1976; **54**: 129–139.

61 Baid A. ELISA- A mini review. *Res Rev J Pharm Anal* 2016; **5**.http://www.rroij.com/open-access/elisa-a-mini-review-.php?aid=83329 (accessed 23 Jul2019).

62 Shapiro HM. *Practical flow cytometry*. 4th ed. Wiley-Liss: New York, 2003.

63 Chang Q, Ornatsky OI, Siddiqui I, Loboda A, Baranov VI, Hedley DW. Imaging mass cytometry. *Cytometry A* 2017; **91**: 160–169.

64 Flow cytometry intracellular staining protocol | Abcam. https://www.abcam.com/protocols/flow-cytometry-intracellular-staining-protocol (accessed 30 Mar2020).

65 Evans CM, Jenner RG. Transcription factor interplay in T helper cell differentiation. *Brief Funct Genomics* 2013; **12**: 499–511.

66 Rio DC. Reverse transcription-polymerase chain reaction. *Cold Spring Harb Protoc* 2014; **2014**: 1207–1216.

67 Dzhagalov IL, Melichar HJ, Ross JO, Herzmark P, Robey EA. Two-photon imaging of the immune system. *Curr Protoc Cytom Editor Board J Paul Robinson Manag Ed Al* 2012; **0 12**: Unit12.26.

68 Germain RN, Miller MJ, Dustin ML, Nussenzweig MC. Dynamic imaging of the immune system: progress, pitfalls and promise. *Nat Rev Immunol* 2006; **6**: 497–507.

69 Stein JV, F. Gonzalez S. Dynamic intravital imaging of cell-cell interactions in the lymph node. *J Allergy Clin Immunol* 2017; **139**: 12–20.

70 Malide D. In vivo cell tracking using two-photon microscopy. In: Bai M (ed). *In Vivo Fluorescence Imaging: Methods and Protocols*. Springer New York: New York, NY, 2016, pp 109–122.

71 Takeda A, Miyasaka M, Umemoto E. Two-photon imaging of T-cell motility in lymph nodes: In vivo and ex vivo approaches. *Methods Mol Biol Clifton NJ* 2018; **1763**: 43–52.

72 Chtanova T, Han S-J, Schaeffer M, van Dooren GG, Herzmark P, Striepen B *et al.* Dynamics of T cell, antigen-presenting cell, and pathogen interactions during recall responses in the lymph node. *Immunity* 2009; **31**: 342–355.

73 Kobezda T, Ghassemi-Nejad S, Glant TT, Mikecz K. In vivo two-photon imaging of T cell motility in joint-draining lymph nodes in a mouse model of rheumatoid arthritis. *Cell Immunol* 2012; **278**: 158–165.

74 Zhang Z, Procissi D, Li W, Kim D-H, Li K, Han G *et al.* High resolution MRI for non-invasive mouse lymph node mapping. *J Immunol Methods* 2013; **0**. doi:10.1016/j.jim.2013.06.013.

75 Harrell MariaI, Iritani BM, Ruddell A. Lymph node mapping in the mouse. *J Immunol Methods* 2008; **332**: 170–174.

76 Spellberg B, Ibrahim AS, Lin L, Avanesian V, Fu Y, Lipke P *et al.* Antibody titer threshold predicts anti-candidal vaccine efficacy even though the mechanism of protection is induction of cell-mediated immunity. *J Infect Dis* 2008; **197**: 967–971.

77 Cunnington AJ. The importance of pathogen load. *PLoS Pathog* 2015; **11**. doi:10.1371/journal.ppat.1004563.

78 Hofer H, Watkins-Riedel T, Janata O, Penner E, Holzmann H, Steindl-Munda P *et al.* Spontaneous viral clearance in patients with acute hepatitis C can be predicted by repeated measurements of serum viral load. *Hepatol Baltim Md* 2003; **37**: 60–64.

79 Deng M, Scott MJ, Loughran P, Gibson G, Sodhi C, Watkins S *et al.* Lipopolysaccharide clearance, bacterial clearance, and systemic inflammatory responses are regulated by cell type–specific functions of TLR4 during sepsis. *J Immunol* 2013; **190**: 5152–5160.

80 Manderscheid PA, Bodkin RP, Davidson BA, Jensen E, Russo TA, Knight PR. Bacterial clearance and cytokine profiles in a murine model of postsurgical nosocomial pneumonia. *Clin Diagn Lab Immunol* 2004; **11**: 742–751.

81 White NJ. Malaria parasite clearance. *Malar J* 2017; **16**: 88.

82 White N. The parasite clearance curve. *Malar J* 2011; **10**: 278.

83 Laudanski K, Lapko N, Zawadka M, Zhou BX, Danet-Desnoyers G, Worthen GS. The clinical and immunological performance of 28 days survival model of cecal ligation and puncture in humanized mice. *PLoS ONE* 2017; **12**. doi:10.1371/journal.pone.0180377.

84 Strausberg RL. Tumor microenvironments, the immune system and cancer survival. *Genome Biol* 2005; **6**: 211.

85 Shimasaki N, Jain A, Campana D. NK cells for cancer immunotherapy. *Nat Rev Drug Discov* 2020; **19**: 200–218.

86 Howat WJ, Wilson BA. Tissue fixation and the effect of molecular fixatives on downstream staining procedures. *Methods San Diego Calif* 2014; **70**: 12–19.

87 Srinivasan M, Sedmak D, Jewell S. Effect of fixatives and tissue processing on the content and integrity of nucleic acids. *Am J Pathol* 2002; **161**: 1961–1971.

88 Turner VM, Mabbott NA. Structural and functional changes to lymph nodes in ageing mice. *Immunology* 2017; **151**: 239–247.

89 Angeli V, Ginhoux F, Llodrà J, Quemeneur L, Frenette PS, Skobe M *et al.* B cell-driven lymphangiogenesis in inflamed lymph nodes enhances dendritic cell mobilization. *Immunity* 2006; **24**: 203–215.

90 Amsen D, de Visser KE, Town T. Approaches to determine expression of inflammatory cytokines. *Methods Mol Biol Clifton NJ* 2009; **511**: 107–142.

91 Huang JH, Cárdenas-Navia LI, Caldwell CC, Plumb TJ, Radu CG, Rocha PN *et al.* Requirements for T lymphocyte migration in explanted lymph nodes. *J Immunol Baltim Md 1950* 2007; **178**: 7747–7755.

92 Matheu MP, Cahalan MD, Parker I. In situ lymph node imaging. *Cold Spring Harb Protoc* 2011; **2011**: pdb.prot5567-pdb.prot5567.

93 Ross JO, Melichar HJ, Halkias J, Robey EA. Studying T cell development in thymic slices. *Methods Mol Biol Clifton NJ* 2016; **1323**: 131–140.

94 Giger B, Bonanomi A, Odermatt B, Ladell K, Speck RF, Kojic D *et al.* Human tonsillar tissue block cultures differ from autologous tonsillar cell suspension cultures in lymphocyte subset activation and cytokine gene expression. *J Immunol Methods* 2004; **289**: 179–190.

95 Craston R, Koh M, Mc Dermott A, Ray N, Prentice HG, Lowdell MW. Temporal dynamics of CD69 expression on lymphoid cells. *J Immunol Methods* 1997; **209**: 37–45.

96 Salmon H, Rivas-Caicedo A, Asperti-Boursin F, Lebugle C, Bourdoncle P, Donnadieu E. Ex vivo imaging of T cells in murine lymph node slices with widefield and confocal microscopes. *J Vis Exp* 2011. doi:10.3791/3054.

97 Belanger MC, Kinman AWL, Catterton MA, Ball AG, Groff BD, Melchor SJ *et al.* Acute lymph node slices are a functional model system to study immunity ex vivo. *bioRxiv* 2019; : 865543.

98 Ge J, Wood DK, Weingeist DM, Prasongtanakij S, Navasumrit P, Ruchirawat M *et al.* Standard fluorescent imaging of live cells is highly genotoxic. *Cytom Part J Int Soc Anal Cytol* 2013; **83**: 552–560.

99 Artifacts of light. *Nat Methods* 2013; **10**: 1135–1135.

2 ACUTE LYMPH NODE SLICES ARE A FUNCTIONAL MODEL SYSTEM TO STUDY IMMUNITY EX VIVO

2.1 INTRODUCTION

Events in the lymph node (LN) determine whether a host successfully fights infection and responds to vaccines, whether a nascent tumor is recognized and destroyed, and whether host tissues remain safe from autoimmunity. These immune responses arise in large part from precise spatial organization of cells and proteins in the lymph node.[1–3] The structure of a lymph node can be roughly divided into an outer cortex containing B cell follicles, a T cell zone, or paracortex, and an inner medulla.[1,4] During an immune response, cells in these regions communicate through both physical contact and secreted signals. Diffusion and the formation of gradients of secreted cytokines through the extracellular matrix generate orchestrated cell migration,[5–7] and the local concentration of cytokines and other signals can drive strong positive feedback and divergent outcomes effecting the overall health of the host.[8] All of these features suggest that the organization of the node may be essential to its function,[2,9,10] and indeed, many similarly complex non-linear biological systems are exquisitely sensitive to spatial organization.[11]

Investigating the function of the lymph node with high spatial, temporal, and chemical resolution within a realistic microenvironment is challenging with existing experimental systems. Recent technological advances in immunological analysis have focused significantly on high-content single cell data using flow cytometry or mass cytometry,[12,13] analysis of single-cell secretion and gene expression using microfluidics,[14–20] and on bulk measurements such as metabolomics[21] and live cell metabolic analysis.[22] However, these cannot provide information on LN organization. Complementing this work, live in vivo imaging was developed over 15 years ago and continues to provide impressive insight into the dynamics of cell and tissue-level behavior in the native environment.[23–27] Yet, it is challenging to experimentally manipulate tissues in vivo without prior genetic modification (e.g. optogenetics) or invasive injection. Approaches that retain

the tissue's spatial organization via fixation have revealed distinct regional subpopulations of cells,[28–30] but fixed tissue is not amenable to experimental manipulation. While existing technologies can reveal important aspects of LN biology, a single approach that maintains the biological complexity of the organ while providing dynamic experimental access close to that of traditional cell cultures is still largely missing from the immunologist's toolbox.[31]

Live ex vivo slices of lymph node tissue may provide a necessary middle-out approach, in a manner complementary to in vitro and in vivo work. Decades of work with brain slices[32–35] set a precedent for both acute[34,36] and long-term experimentation[37], which informed protocols for other tissues such as the pancreas,[38] liver,[39] lung,[40] and heart[41]. Unlike in vitro cell culture, slices cultured ex vivo preserve the extracellular microenvironment and any stromal and matrix-bound signals, which are essential to proper cellular positioning and motility.[2,6,42–44] Furthermore, all cell types are retained in their correct ratios, whereas standard tissue dissociation (crushing and filtering) selectively depletes matrix-bound populations such as dendritic cells.[45] In contrast to in vivo work, using tissue slices simplifies timecourse analysis via repeated measurements of the same tissue sample, especially after ex vivo stimulation.[46–51] Slices also allow for precise stimulation of the organ interior, because precise quantities of drugs or other agents can be added at known concentrations and at known times.[52,53] Furthermore, slices can be coupled together or co-cultured to generate a simplified model of inter-organ communication, akin to multi-organ organ-on-chip systems used to model pharmacokinetics and disease mechanisms.[54,55] In the field of immunology, slices of the thymus have been used extensively to study T cell development.[56,57] Live spleen[58,59] and tonsillar[60,46,61] slices were demonstrated 20 years ago, and continue to be a valuable tool to study immune function and viral infection. Most of the reported uses of live murine lymph node tissue slices have been to study T cell motility,[62–66] but otherwise this system has seen limited use.

At this time, unanswered questions regarding the viability, level of immune activation, and retention of function appear as potential obstacles to the broad adoption of live lymph node slices. To address this issue, here we describe a systematic evaluation of the procedures surrounding the slicing, handling, and analyzing of live murine lymph nodes in short-term cultures, towards establishing lymph node slices as a robust experimental platform. We comprehensively assess 24-hr viability, the extent of inflammation due to slicing, and retention of acute function. Finally, we validate the use of acute murine lymph node slices to quantify antigen-specific T cell responses ex vivo.

2.2 MATERIALS AND METHODS

2.2.1 Generating lymph node tissue slices

All animal work was approved by the Institutional Animal Care and Use Committee at the University of Virginia under protocol #4042, and was conducted in compliance with guidelines the Office of Laboratory Animal Welfare at the National Institutes of Health (United States). Male and female C57BL/6 mice ages 6-12 weeks (Jackson Laboratory, USA) were housed in a vivarium and given water and food ad libitum. On the day of the experiment, animals were anesthetized with isoflurane followed by cervical dislocation. The axial, inguinal, and brachial lymph nodes were removed quickly and cleaned of any fat. It was critical to harvest the organ without deforming or puncturing it. Lymph nodes were placed in ice-cold DPBS without calcium or magnesium (Lonza, Walkersville MD, USA, #17-512F) supplemented with 2 % heat-inactivated fetal bovine serum (FBS, Gibco, Fisher Scientific, 100 % US Origin, 1500-500 Lot 106B14). Lymph nodes were embedded in 6 % w/v low melting point agarose (Lonza, Walkersville MD, USA) in 1X PBS. Agarose was melted in a microwave and allowed to cool until the temperature was comfortable in the hand. Further optimization showed that maintaining the melted agarose at 50 °C in a water bath after microwaving provided a more reproducible approach. Liquid agarose was poured into a 35 mm Petri dish, and lymph nodes were embedded in the liquid agarose close to the bottom

of the dish. All lymph nodes were oriented to allow for the largest cross-section when slicing, i.e. a cut along the transverse plane. The dish was then rested at room temperature for approximately 2 minutes and allowed to harden on ice for the next 3 minutes. Once hardened, a 10 mm tissue punch (World Precision Instruments) was used to extract a section of agarose containing the lymph node. The block was inverted so the node was at the top of the section and glued onto a small mounting stage with Duro® Super Glue (cyanoacrylate) and immediately submerged in a buffer tray containing ice-cold 1X PBS unless otherwise noted. Up to 6 lymph nodes were mounted on a single stage and sliced simultaneously.

A Leica VT1000S vibratome (Bannockburn, IL, USA) set to a speed of 90 (0.17 mm/s) and frequency of 3 (30 Hz) was used to slice 300-µm thick sections. A fan-shaped paint brush was used to remove the slices. Slices were immediately placed in a 6-well plate containing 3 mL per well of “complete RPMI”: RPMI (Lonza, 16-167F) supplemented with 10 % FBS (VWR, Seradigm USDA approved, 89510-186) 1x L-glutamine (Gibco Life Technologies, 25030-081), 50 U/mL Pen/Strep (Gibco), 50 µM beta-mercaptoethanol (Gibco, 21985-023), 1 mM sodium pyruvate (Hyclone, GE USA), 1x non-essential amino acids (Hyclone, SH30598.01), and 20 mM HEPES (VWR, 97064-362). Slices were rested in a sterile incubator at 37 °C with 5 % CO_2 for at least one hour prior to use.

2.2.2 Activation of cell suspensions and tissue samples

Primary lymphocyte cell cultures were prepared by passing 6 peripheral nodes (axial, brachial, and inguinal) through a single 70-µm nylon mesh filter (Thermo Fisher, USA) with the rubber tip of the plunger from either a 1- or 3-mL syringe. Cells were plated in a 96-well cell-culture treated plate (Costar, VWR, USA) at a density of $1x10^6$ cells/mL in a 300 µL final volume. To obtain inflamed lymphocytes as positive controls, aluminum hydroxide gel adjuvant (Alhydrogel®, 10 mg/mL alum, Invivogen) was added to the wells for a final concentration of 1

mg/mL alum. Cells were cultured for 3.5 hours in a cell culture incubator (37 °C, 5% CO_2) and prepared for flow as described below.

To compare activation of slices versus cell suspensions, peripheral lymph nodes (axial, brachial, inguinal) were randomly assigned to be sliced or crushed for lymphocyte culture. For the sliced condition, nodes were sliced 300 µm thick and each slice was placed into 500 µL complete media. For lymphocyte culture condition, nodes were crushed through a filter as described above. Lymphocyte suspensions were cultured in 500 µL aliquots at cell densities matched to tissue slice samples, where 1X culture was 1.7 $x10^6$ cells/mL, and 2X culture was 3.4 $x10^6$ cells/mL. Slices and lymphocyte cell culture were incubated for 20 hours at 37 °C, 5% CO_2, with anti-mouse/human CD3Ɛ (Biolegend, clone: 145-2C11, Purified grade) at 1, 0.5, or 0 µg/mL, with R848 (Resiquimod, InvivoGen, San Diego, CA) at 10 1, 0.1, or 0 µg/mL, or F(ab')2 goat anti-mouse IgM (µ chain specific, Jackson ImmunoResearch) at 10 µg/mL.

2.2.3 Flow cytometry

To prepare samples for flow cytometry, tissue slices were separated from the surrounding agarose through careful mechanical manipulation with a paint brush; individual tissue slices or groups of slices were then crushed through a 70-µm nylon mesh filter (Thermo Fisher, USA) using the rubber tip of a 1 or 3 mL syringe plunger to generate cell suspensions. Unsliced lymph nodes were similarly crushed through 70-µm filters, according to standard methods, for comparison. Cell suspensions were stained with Pacific Blue-B220, Brilliant Violet 421-CD3, Alexa Fluor 488-CD80, PE-CD11c, PE-Cy7-CD69, APC-Cy7-CD4 (all from Biolegend, USA, details provided in Table 2.1) and DilC1 (Thermo Fisher, USA). After staining, 2 µM propidium iodide (PI, Sigma Aldrich, USA) was added. Stained samples were washed and resuspended in 500 µL of 1x PBS with 2% FBS (flow buffer). Antibody compensation controls were run with OneComp eBeads™ (eBiosciences, USA) according to manufacturer protocol. Viability compensation controls, including PI and DilC1, were run on primary lymphocyte populations. PI controls were run with

mixed live and killed cells; cells were killed with 35% ethanol for 10 minutes at room temperature. Live cells were stained with DilC1 for 30 minutes at 4 °C, washed and mixed with unstained live cells in a 1:1 ratio to act as a single stain compensation control. Stained suspensions were analyzed on a CyAn APD LX cytometer (Beckman Coulter, USA) unless otherwise noted. Analysis was completed using FlowJo 7 or FCS Express as noted.

Table 2.1: Product information for antibodies used in flow cytometry

Target	Clone	Fluorophore	Product Number	Vendor
B220	RA3-6B2	Pacific Blue	103230	Biolegend
CD3	17A2	Brilliant Violet 421	100227	Biolegend
CD3	17A2	Brilliant Violet 510	100233	Biolegend
CD80	16-10A1	Alexa Fluor 488	104715	Biolegend
CD11c	N418	PE	117307	Biolegend
CD69	H1.2F3	PE-Cy7	104511	Biolegend
CD69	H1.2F3	PE	104507	Biolegend
CD4	GK1.5	APC-Cy7	100525	Biolegend
CD8	53-6.7	Alexa Fluor 488	100726	Biolegend
CD25	PC61	Brilliant Violet 421	102033	Biolegend

2.2.4 ELISA

Culture supernatant was collected and analyzed by sandwich ELISA for the cytokines IFNγ, IL-2, IL-4, and TNFα. A high-binding plate (Corning Costar 96 well ½ area, #3690; Fisher Scientific) was coated with 1 µg/mL anti-IFNγ XMG1.2, 1 µg/mL anti-IL-2 JES6-1A12, ELISA MAX capture anti-IL-4 (previous antibodies from Biolegend) or capture TNFα (R&D systems, cat: DY410-05) in PBS overnight at 4°C, then washed. All washing steps were performed in triplicate with 0.05% Tween-20 in PBS. Wells were blocked for 2 hours with 1% BSA and 0.05% Tween-20 (Fisher Scientific) in PBS (block solution). Serial dilutions of recombinant murine IFNγ, IL-2 (Peprotech, Rocky Hill, NJ), IL-4 (ELISA MAX standard, Biolegend) and TNFα (R&D Systems) were prepared in a 1:1 v/v mixture of block solution and complete media, and supernatant samples were diluted 1:1 v/v with block solution. Samples were added to the plate in duplicate

and incubated for 2 hours, then washed. Biotinylated anti-IFNγ R46A2 (0.5 µg/mL), anti-IL-2 JES6-5H4 (1 µg/mL), ELISA MAX detection anti-IL-4 (Biolegend), or detection TNFα (R&D Systems) were prepared in blocking solution and added to the plate. Avidin-HRP (1X) (Fisher Scientific) in blocking solution was added to the plate and incubated for 30 minutes, then washed. Plates were developed using TMB substrate (Fisher Scientific), stopped with 1M sulfuric acid (Fisher Scientific), and absorbance values were read at 450 nm on a plate reader (CLARIOstar; BMG LabTech, Cary, NC). To determine concentration of sample solutions, calibration curves were generated using a four-parameter logistic curve fit:

$$Y = min + (X^{HillSlope}) \times \frac{(max - min)}{(X^{HillSlope} + EC50^{HillSlope})} \qquad \text{Equation 2.1}$$

Limit of Detection (LOD) was calculated from the average of the blank + 3x standard deviation of the blank.

2.2.5 Inflammatory gene expression array

Axial, brachial, and inguinal lymph nodes from four mice were mixed and randomly distributed into two groups: 12 nodes for slicing and 12 nodes for cell suspensions. Approximately 24 slices were collected as described above and cultured individually at 37 °C with 5% CO_2 overnight. Meanwhile, lymphocyte suspensions from whole nodes were generated by passing the lymph nodes through a 70-µm filter. The lymphocytes were pooled and resuspended at 0.86 x10^6 cells/mL (mean cellular density matched to the lymph node slices) then cultured overnight. After the overnight culture period all samples were flash frozen and stored at -80 °C until RNA could be isolated.

RNA was isolated using a RNeasy Mini Kit according to manufacturer instructions (Qiagen, USA). Briefly, pooled tissue samples (intact slices or cell culture suspensions) were homogenized in lysate buffer; cells were vortexed in lysate buffer and passed through a 20-gauge needle to generate a homogenized sample. Lysates were mixed with 70% ethanol and filtered

according to manufacturer recommendations to obtain genetic material. To remove genomic DNA from the sample, 1 µg RNA was added to 1 U/µL DNase (Invitrogen, USA) in DNase reaction buffer. The digestion was run for 15 min at room temperature and stopped with 25 mM EDTA and heated to 65 °C for 10 min. An Accuris qMax cDNA synthesis kit was used to generate the cDNA. Reaction buffer, qMax reverse transcriptase, RNA and water were incubated at 42 °C for 30 minutes. The reaction was stopped by heating to 85 °C for 10 minutes.

A RT^2 profiler array for mouse inflammatory cytokines and receptors (Qiagen, USA) was used according to manufacturer recommendations to measure the expression of 84 inflammatory genes (Table S1). SYBR Green was used as the reporter and the reaction was run for 40 cycles on a QuantStudio 6 PCR instrument (Thermo Fisher, USA). Genes that were detected on or after cycle 35 were considered not expressed. Of the expressed genes, the average relative expression was determined based on the average expression of 5 housekeeping genes (Table 2.2) Because all samples in each group were pooled for analysis, two cut-offs were defined for significant differential expression, two and three standard deviations from the mean differential expression.

.

Table 2.2: Gene targets from Qiagen inflammatory gene array.

Gene	Relative Expression (Sliced/Crushed)	Differential Designation	Gene	Relative Expression (Sliced/Crushed)	Differential Designation
Aimp1	8.94	Not Different	Il10ra	4.95	Not Different
Bmp2	0.01	2SD Different	Il10rb	26.37	1SD Different
Ccl1	0.32	Not Expressed	Il11	33.37	2SD Different
Ccl11	10.33	Not Different	Il13	17.25	Not Different
Ccl12	22.80	1SD Different	Il15	0.21	Not Different
Ccl17	23.80	1SD Different	Il16	0.02	Not Expressed
Ccl19	3.07	Not Different	Il17a	0.02	Not Expressed
Ccl2	385.30	2SD Different	Il17b	0.00022	2SD Different
Ccl20	5.21	Not Different	Il17f	0.02	Not Expressed
Ccl22	13.63	Not Different	Il1a	0.26	Not Different
Ccl24	1.19	Not Different	Il1b	17.40	Not Different
Ccl3	1.88	Not Different	Il1r1	0.61	Not Different
Ccl4	108.01	2SD Different	Il1rn	150.13	2SD Different
Ccl5	1.70	Not Different	Il21	0.02	Not Expressed
Ccl6	0.60	Not Expressed	Il27	0.02	Not Expressed
Ccl7	4.42	Not Different	Il2rb	0.02	Not Expressed
Ccl8	490.67	2SD Different	Il2rg	0.29	Not Expressed
Ccl9	12.06	Not Different	Il3	0.02	Not Expressed
Ccr1	1.80	Not Different	Il33	3.04	Not Different
Ccr10	0.02	Not Expressed	Il4	3.29	Not Different
Ccr2	0.02	Not Expressed	Il5	4.66	Not Different
Ccr3	0.77	Not Expressed	Il5ra	0.02	Not Expressed
Ccr4	0.02	Not Expressed	Il6ra	8.73	Not Different
Ccr5	5.96	Not Different	Il6st	33.41	2SD Different
Ccr6	0.02	Not Expressed	Il7	1.38	Not Different
Ccr8	0.02	Not Expressed	Lta	0.04	Not Expressed
Cd40lg	8.90	Not Different	Ltb	18.25	1SD Different
Csf1	0.27	Not Different	Mif	8.66	Not Different
Csf2	8.28	Not Different	Nampt	0.56	Not Expressed
Csf3	22.69	1SD Different	Osm	1.55	Not Different
Cx3cl1	0.02	Not Expressed	Pf4	1.76	Not Different
Cxcl1	0.27	Not Expressed	Spp1	33.49	2SD Different
Cxcl10	803.88	2SD Different	Tnf	0.02	Not Expressed
Cxcl11	0.023	Not Different	Tnfrsf11b	0.02	Not Expressed
Cxcl12	0.61	Not Different	Tnfsf10	0.13	Not Different
Cxcl13	56.92	2SD Different	Tnfsf11	0.02	Not Expressed
Cxcl15	0.80	Not Different	Tnfsf13	0.02	Not Expressed
Cxcl5	3.03	Not Different	Tnfsf13b	0.01	2SD Different
Cxcl9	27.69	1SD Different	Tnfsf4	1.37	Not Different
Cxcr2	0.02	Not Expressed	Vegfa	0.06	Not Different
Cxcr3	0.02	Not Expressed	Actb		Housekeeper
Cxcr5	11.05	Not Different	B2m		Housekeeper
Fasl	1.58	Not Different	Gapdh		Housekeeper
Ifng	1.10	Not Different	Gusb		Housekeeper
			Hsp90ab1		Housekeeper

2.2.6 DQ-OVA culture of lymph node slices

Slices were collected as above and randomly assigned to live culture or fixation. Live slices were cultured with ovalbumin (OVA) protein solution, consisting of 1 µg/mL DQ-OVA (Thermo Fisher, USA) plus 9 µg/mL purified OVA (InvivoGen, USA) in 500 µL supplemented RPMI, or vehicle control in in 500 µL supplemented RPMI. Killed control slices were fixed in formalin (4% formaldehyde, Protocol, USA) for 1 hour at 37 °C with 5% CO_2, then incubated with OVA protein solution. Slices were incubated for 24 hours at 37 °C, 5% CO_2, and images were collected at 1,2,4,8 and 24 hours.

2.2.7 Antigen-specific interactions in lymph node slices

Spleens were collected from Rag2/OT-II female mice (Taconic Biosciences) aged 6-10 weeks following isoflurane anesthesia and cervical dislocation. Splenocytes were isolated using a 70-µm pore size nylon filter (Fisher Scientific, USA), and the filter was washed with sterile 1x phosphate buffer saline (PBS) supplemented with 2% v/v fetal bovine serum (FBS, VWR, USA). Cell density was determined through trypan blue exclusion. Using a CD4+ T cell enrichment kit (StemCell Technologies, USA), CD4+ T cells were isolated from bulk splenocytes by negative selection. OTII CD4+ T cells ($0.5x10^6$ cells: 200 µL at $2.5x10^6$ cells/mL) were intravenously injected into 8 female C57Bl/6 mice. The following day, the C57Bl/6 mice were vaccinated with 50 µg of OVA protein in either 200 µL of Alum 50:50 v/v PBS or PBS alone. Vaccinated mice were humanely euthanized on days 1,4 and 7 after vaccination, and lymph nodes were harvested and sliced. Slices were cultured overnight in complete media supplemented with 10 µg/mL OVA protein (Invivogen) or PBS. After overnight culture, the supernatant was collected for cytokine analysis using ELISA and the slices immunostained and imaged.

2.2.8 Immunofluorescent staining and imaging of lymph node slices

Slices were stained according to previously published procedures.[50] Briefly, slices were placed on a Parafilm® covered surface and a washer was placed on top. Samples were treated

with blocking solution (anti-CD16/32) for 20 minutes in a cell culture incubator. Antibody cocktail was added to the blocking solution and samples were incubated for an additional 1 hour. Slices were then washed in sterile 1x PBS for at least 30 minutes in a cell culture incubator. Antibody information can be found in Table 2.3

Unless otherwise noted, imaging was performed on a Zeiss AxioZoom upright macroscope with a PlanNeoFluor Z 1x/0.25 FWD 56mm objective, Axiocam 506 mono camera and HXP 200 C metal halide lamp (Zeiss Microscopy, Germany). Images were collected with Zeiss Filter Sets 38 HE (Ex: 470/40, Em: 525/50), 43 HE (Ex: 550/25, Em: 605/70); 64 HE (Ex: 587/25, Em: 647/70); and 50 (Ex: 640/30, Em: 690/50). Confocal microscopy was performed on a Nikon A1Rsi confocal upright microscope, using a 487 and 638 nm lasers with 525/50 and 685/70 nm GaAsP detectors respectively. Images were collected with a 40x/0.45NA Plan Apo NIR WD objective. Two-photon microscopy and second harmonic imaging were performed in the W.M. Keck Center for Cellular Imaging (University of Virginia) on an Axiovert200 MOT inverted microscope with an LSM510 scan head (Zeiss, Germany). Image was collected with 60x/1.20 WD objective. Image analysis was completed using ImageJ software 1.48v.[67]

Table 2.3: Product information for imaging antibodies.

Target	Clone	Fluorophore	Product Number	Vendor
B220	RA3-6B2	FITC	103205	Biolegend
B220	RA3-6B2	eFluor 570	41-0452-80	eBioscience
CD69	H1.2F3	Alexa Fluor 647	104517	Biolegend
CD4	GK1.5	FITC	100405	Biolegend
CD45	30-F11	Alexa Fluor 488	103121	Biolegend
Lyve-1	ALY7	eFluor 660	50-0443-82	eBioscience
Lyve-1	ALY7	eFluor 570	41-0443-82	eBioscience

2.3 RESULTS

2.3.1 Lymph node slices preserve spatial organization

We developed a protocol for slicing lymph node tissue that was informed by well-established procedures for slicing brain, another delicate tissue, and by prior work with lymphoid tissues.[48,56,68] In brief, LNs were gently isolated from the animal, embedded in agarose for physical support, and sliced on a vibratome. LN slices were immediately immersed in culture media to rest until further processing or experimentation. A detailed experimental protocol is provided in the Methods. In this first section, we highlight some of the key aspects of working with lymph node slices prior to describing the optimization and validation of the method.

One of the primary reasons to work with intact tissue rather than cell culture is the preservation of spatial organization. Indeed, the structure of the lymph node was retained in these live, thick slices in the absence of fixation. Live tissue slices from naïve mice contained distinct B cell regions and lymphatic vasculature/vessels with a distribution that was consistent with in vivo and immuno-histochemical studies (Figure 2.1a).[56,30,69–71] These geographical landmarks were readily visualized using widefield microscopy after live immunofluorescence staining.[50] Ex vivo slices could also be used to visualize the distribution of draining antigen after in vivo vaccination, e.g. with rhodamine-conjugated ovalbumin (OVA) protein (Figure 2.1b-d). Both localization in individual cells (Figure 2.1b) and draining of soluble antigen via the lymphatic and sinus structure (Figure 2.1c-d) were visible without fixing the tissue. While the images described above were collected at low magnification, live tissue slices are also compatible with high resolution microscopy techniques. By using confocal microscopy, we were able to visualize individual cells within the branching lymphatic network (Figure 2.1e). Second harmonic imaging of the collagen network within the LN slice (Figure 2.1f) highlighted the dense collagen network that persists throughout the lymph node, consistent with other examples of live two-photon imaging of the

lymph node.[72–74] These images highlight the potential for lymph node slices to reveal tissue organization.

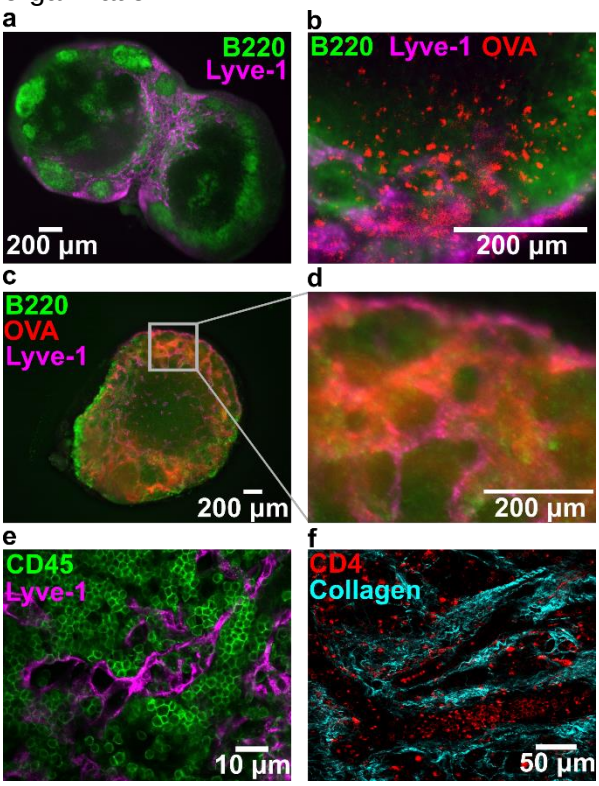

Figure 2.1: Key structural features remain intact in thick lymph node slices. (a) Slice labeled with anti-B220 (FITC, green) and anti-Lyve-1 (eFluor660, purple) revealed key structural features of the lymph node. Slice shown from a female C57Bl-6J mouse. (b-d) Slices from an OVA (rhodamine labelled, red)-immunized C57Bl/6-J mice, labeled as in (a). (b) Rhodamine-OVA was visible inside of cells within the T cell rich (B220-dim) region of the lymph node 3 days post-immunization. (c) Rhodamine-OVA entering the lymph node through the lymphatics 1-day post-immunization. (d) Inset of (c) showing colocalization of draining lymphatics and OVA protein. (e) High-definition image collected by confocal microscopy. Slice labelled with anti-CD45 (AlexaFluor488, green) and anti-lyve-1 (eFluor660, purple). (f) Image of lymph node slice collected by two-photon microscopy, showing CD4 positive T cells (FITC-CD4 Fab', generated in house according to published procedure[74]) within the collagen matrix (second harmonic imaging). Panels c-d collected by B. Groff. Panel f collected by A. Kinman.

2.3.2 Lymph node slices reflect heterogeneity in organ composition

To enable quantitative cellular phenotyping and analysis of viability, we first determined that flow cytometry can be run on a single murine lymph node slice, similar to reports on single thymus slices.[52] Manual counting indicated that each slice yielded, on average, (0.56 ± 0.16) x10^6 cells (n = 10 slices, mean ± std dev). The variability in cell number reflects the fact that the surface area varies between slices. We found that a single murine lymph node slice provided sufficient cell counts to collect flow cytometric data (Figure 2.2a), and all subsequent analyses were performed on single slices unless otherwise noted. Live cells were identified using PI exclusion, and the remaining cells were separated into dead (PI^{high}, $DilC1^{low}$) and apoptotic (PI^{high}, $DilC1^{high}$)

populations according to signal from the mitochondrial membrane potential dye DilC1 Figure 2.2b). Live cells were phenotyped by surface markers for cell type (Figure 2.2c-e).[75]

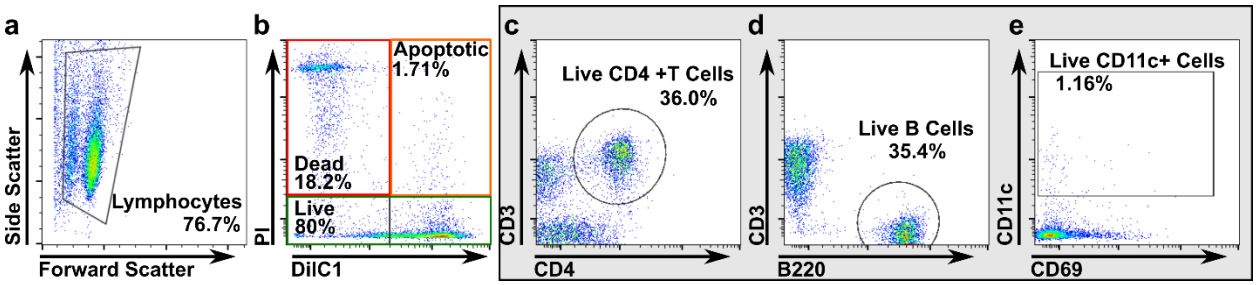

Figure 2.2: Flow cytometry data can be collected from a single slice. (a-e) Representative flow plots from a single naïve slice showing scatter (a), viability (b), T cell, B cell, and CD11c+ cell phenotyping (c,d,e, respectively).

On average, the cell suspension obtained from single C57Bl/6 lymph node slices matched that obtained from whole lymph nodes: 50% CD3+ T cells (51% CD4+, 49% CD4-), 44% B cells, and 1% CD11c+ cells (Figure 2.3a). As expected, there was large heterogeneity in cellular composition between individual slices, as the slices reflect the complex 3-dimensional structure of this organ and non-uniform distribution of cell types within it. In fact, immunofluorescence staining of thin (100-μm) serial slices of fixed lymph node tissue revealed significant heterogeneity from slice to slice in terms of both gross structural changes and cellular composition (Figure 2.3b,c). Thus, tissue slices of spatially organized organs may provide a means to quantify and assess variation in population function across the tissue, whereas methods that begin with tissue homogenization lose this information. Over dozens of experiments, we observed that variations in large scale tissue architecture between slices from the same organ exceeded the variations between the inguinal, axial and brachial lymph nodes. As the large-scale cellular architecture was similar for these three types of skin-draining lymph nodes, they were mixed for subsequent studies.

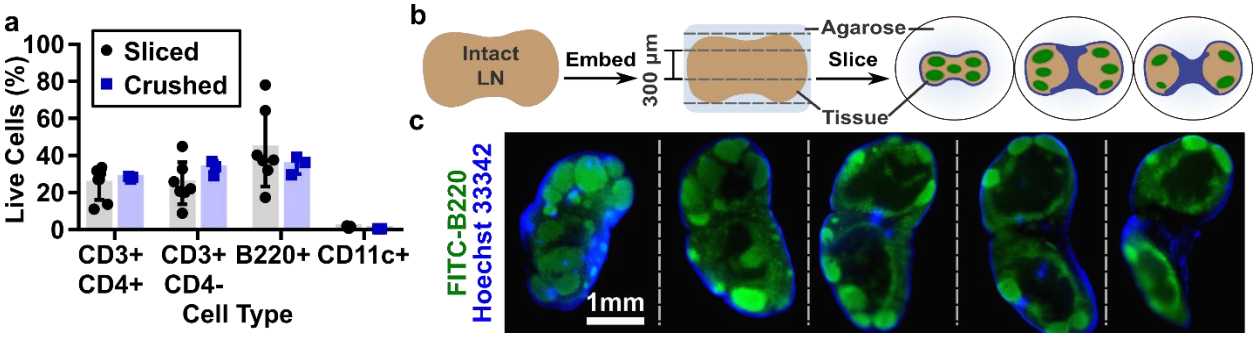

Figure 2.3:Lymph node slices are highly heterogeneous. (a) Average phenotypic distribution within individual lymph node slices compared to whole crushed lymph nodes. The average slice was equally distributed between B cells (44±21%) and CD3+ T cells (50±17%), with very few CD11c+ cells collected (1±0.4%); exact composition varied between slices. These data were not significantly different from whole crushed lymph nodes. Bars show mean ± standard deviation from N=7 sliced and N=3 crushed nodes. (b) Schematic representation of the biological source of heterogeneity from slicing. B cell follicles shown in green; sinuses in blue. (c) Serial 100-µm thick slices of a fixed lymph node labelled with FITC anti-B220 (green) and Hoechst 33342 (blue) detailing the heterogeneous cell distribution in the lymph node and even within a single 300-µm span. Images collected by B. Groff.

2.3.3 Single 300-µm LN slices had similar viability overnight as lymphocyte suspensions

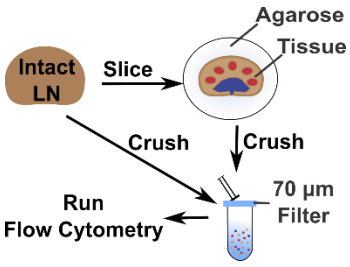

Figure 2.4: **Schematic showing experimental work flow**, Intact LNs were either passed through a 70-µm filter or embedded in agarose, sliced, cultured, and then passed through a filter.

Next, we sought to optimize the conditions for lymph node slicing. First, we varied slice thickness to maximize the number of slices that can be collected from a single node while maintaining high viability. For reference, we compared cells collected from tissue slices to cells collected directly from intact lymph nodes by the conventional method of crushing through a filter (Figure 2.4). First, we determined the appropriate thickness for murine lymph node slices (Figure 2.5); the minimal slice thickness for a given tissue depends on its mechanical strength, while an upper bound is set by its rate of oxygen consumption.[76] Lymph node slices collected at 100 µm were usually torn, so this thickness was not considered further. 200-µm-thick slices were intact but sometimes mechanically distended (stretched); consistent with this, these slices were diminished in initial viability compared to 400-µm slices. There was no significant difference in initial or 24-hr viability between 300-µm and 400-µm slices, so 300 µm was selected to provide more slices per node. The percentage of live cells in slices was similar to

that of cell culture suspensions over this time period (Figure 2.5), indicating that the act of slicing did not significantly decrease the viability of the samples compared to crushing.

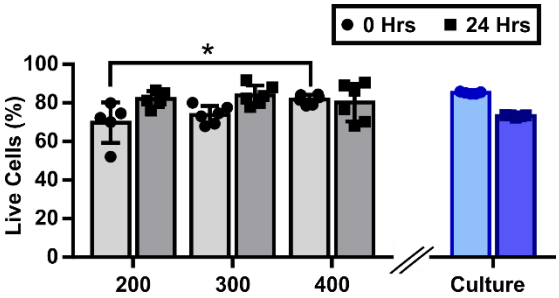

Figure 2.5: Tissue thickness had a slight effect on initial viability, as 200-µm thick slices were less viable than 400-µm thick slices. No significant differences were seen between thicknesses after 24 hours of culture. The viability of tissue slices was comparable to that of cell culture.

2.3.4 Selection of slicing conditions to minimize activation markers

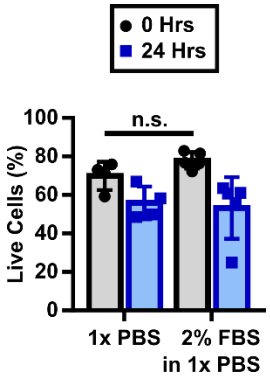

Figure 2.6: Serum in slicing media did not increase viability. Slices were collected in both ice cold 1x PBS and PBS supplemented with 2% FBS. There was no significant differences between these conditions at either time point. Two-way ANOVA with multiple comparisons; ns denotes p>0.05.

We aimed to select slicing conditions that minimized unintentional activation or alteration of the state of the lymph node, particularly the induction of rapid, non-specific inflammation due to mechanical damage from slicing. To do so, we varied the slicing conditions and analyzed viability and apoptotic markers, as well as the intensity of CD69 on CD4+ T cells and CD80 on B cells and CD11c-expressing cells, which include dendritic cells (DCs).[77–79] We first considered the protein content and oxygenation of the media used during slicing. Inclusion of proteins in the chilled slicing media (i.e., addition of 2% v/v fetal bovine serum (FBS) to PBS) did not improve viability (Figure 2.6), so PBS was used for simplicity. Oxygenation of slicing media is essential for brain slices, and this convention has been propagated through many other tissue slicing protocols.[56,68,48,80,81] However, lymph nodes, and many other tissues, are thought to be mildly hypoxic in vivo.[82] We hypothesized that hyperoxia may not be needed during slicing of LN tissue. To test this hypothesis, we sliced tissue in PBS that was either equilibrated with the atmosphere or bubbled with oxygen. Slices collected in oxygen-saturated media showed a small but significant decrease in the live population compared to those sliced under atmospheric conditions and trended towards a greater apoptotic population

(Figure 2.7a; tissues analyzed 1 hr post slicing). CD80 expression was also increased on CD11c positive cells from these slices (Figure 2.7b). From these data we concluded that an O_2-saturated environment during slicing did not improve lymph node slice viability, and so for simplicity all slices were collected in 1x PBS without oxygen bubbling. We note that these results were collected on skin-draining lymph nodes, and we cannot exclude the possibility that lymph nodes from other areas of the body may require different handling.

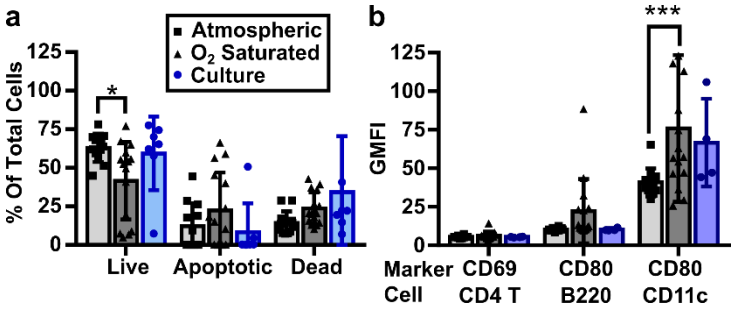

Figure 2.7: Slicing LNs in O_2-saturated media caused damage to the cells. (a) Slices collected in an oxygen-saturated environment had a statistically lower percentage of live cells and an increased spread in the apoptotic population. (b) Slices collected under atmospheric conditions had statistically significant lower expression of CD80 on CD11c+ cells compared to slices collected in an oxygen-saturated environment but not significantly lower than lymphocyte culture. Each dot represents a single slice from skin-draining lymph nodes or cell culture well. Two-way ANOVA with multiple comparisons *p>0.05 ***p=0.0003.

Slices of many organs are “rested” for one or more hours after collection to allow any effects of cutting to dissipate,[41,83,84] and we tested slices in this window for viability and upregulation of inflammatory markers. We found no significant difference in viability over a period of 1 – 3 hr after slicing (Figure 2.8a), nor any increase in the fluorescence intensities of the activation markers CD69 on CD4+ T cells and CD80 on B cells and CD11c+ cells (Figure 2.8b).

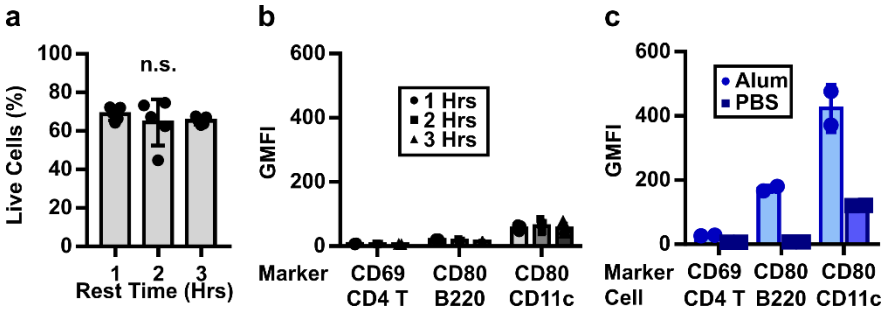

Figure 2.8: Slice viability and activation markers remained stable over a short rest time. (a) Viability was unchanged over short recovery times. (b) The intensity of inflammation markers remained low over short recovery times and was much lower than cf) alum-treated in vitro lymphocyte cultures used as a positive control. 2-way ANOVA with multiple comparisons n.s. p>0.05.

The CD69 and CD80 intensities from slices were comparable to lymphocytes collected directly from crushed nodes and cultured in 1x PBS, and were much lower than those from in vitro-

activated lymphocytes that served as a positive control (Figure 2.8c). Based on these data, we determined that a 1-hour rest is sufficient post-slicing; shorter times may also be acceptable but were not tested. We speculate that the lack of measurable inflammation in response to the mechanical damage of slicing may be due to the rapid dilution of “danger signals” from the cut faces of the slice into the large volume of slicing media. In summary, lymph node slices collected in normoxic saline and rested for one hour displayed high viability and minimal markers of nonspecific activation.

2.3.5 Inflammatory gene expression was low and similar between sliced and crushed lymph nodes.

To further investigate the possibility of inflammation due to slicing, the expression of 84 key inflammatory genes (Table 2.2) was analyzed by RT-PCR array for lymph node tissue slices versus conventional lymphocyte cultures. The slices and cell suspensions were cultured overnight prior to analysis, to allow time for any delayed response or slow-acting inflammatory signals from the process of slicing, then mechanically dissociated directly into lysing buffer. Differential expression was determined by calculating the mean relative expression (sliced/crushed cultures) and setting a conservative threshold at one or two standard deviations from the mean. Consistent with the fact that these were samples from naïve animals, the majority of genes in the inflammatory gene array either were not expressed in either sample (27 genes) or were not differentially expressed between slice culture and cell culture (39 genes; Figure 2.9a), even with the least stringent threshold (1 std dev). Of the differentially expressed genes, 9 out of 18 were related to chemokines and their receptors (Figure 2.9b). We speculate that the increase in gene expression along the chemokine axis may be related to the preservation of the stromal cells in the tissue slices; stromal cells adhere to the matrix and would have been removed by the filter when collecting lymphocyte suspensions.[44,85] Based on the overall low levels of inflammatory gene expression in both tissue slices and cell suspensions, together with the low levels of activation markers observed by flow cytometry (Figure 2.8), we conclude that the process of

slicing does not cause appreciable inflammation of the tissue. These data are consistent with results from tumor slices that found few changes in gene expression caused by the act of slicing.[86]

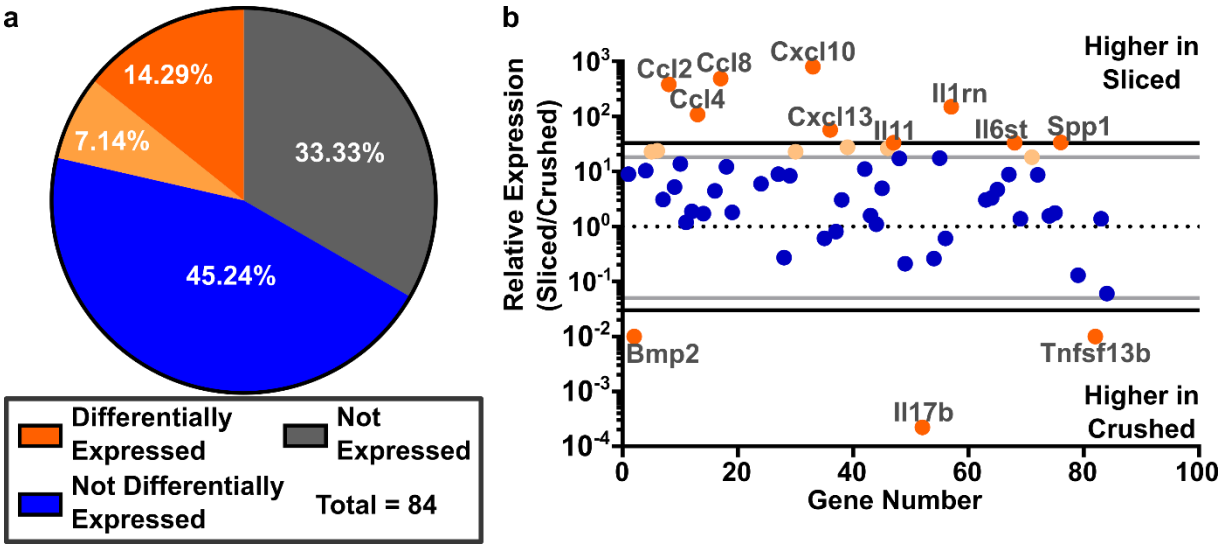

Figure 2.9: Comparable expression of inflammatory genes in slices and cell suspensions from naïve murine lymph nodes. (a) Of the 84 genes investigated, 33.3% were not expressed in either condition, 45.2% were expressed but not differentially expressed, and 14.3-21.4% were differentially expressed. Differential expression was determined by setting a threshold at 1 or 2 standard deviations from the mean relative expression of expressed genes (light and dark orange, respectively). (b) Expressed genes were categorized by the two cut-offs: 2 stdev (black lines) or 1 stdev (grey lines). Seven genes were different between the thresholds. A full gene list is provided in Table 2.2. Pooled samples from N=3 mice, comprising 9 crushed nodes and 30 slices in total.

2.3.6 Lymph node slices processed whole-protein antigen and responded to cellular stimulation

An exciting application of lymph node slice culture is to measure the response of the intact tissue to ex vivo stimulation, with all cell types and structures present and correctly localized. We were particularly interested in the function of antigen-presenting cells, because appropriate antigen recognition is required to initiate adaptive immune responses. We tested the ability of antigen-presenting cells to process whole-protein antigen by incubating live slices with DQ-OVA, a modified form of ovalbumin that becomes fluorescent upon proteolytic cleavage. Repeated fluorescent imaging revealed time-dependent uptake and processing of the whole-protein antigen by cells in lymph node slices. Mean DQ-OVA intensity was significantly greater in live slices than in fixed slices after just two hours (Figure 2.10a). DQ-OVA signal followed a spatial distribution

that was consistent with the sinuses and lymphatics (Figure 2.10b,c), similar to the pattern observed for in vivo antigen drainage (Figure 2.1d). Closer observation by 5-color confocal microscopy showed that the processed protein was visible inside F4/80+ macrophages, CD169+ subcapsular sinus macrophages, and Lyve-1+ lymphatic endothelial cells, but was mostly excluded from B220+ B cells (Figure 2.10d).[87,88] Quantitative image analysis in these densely packed regions was challenging. Qualitatively, the largest fraction of processed protein at this time point appeared to be from CD169+ subcapsular sinus macrophages (Figure 2.10d, arrowheads).

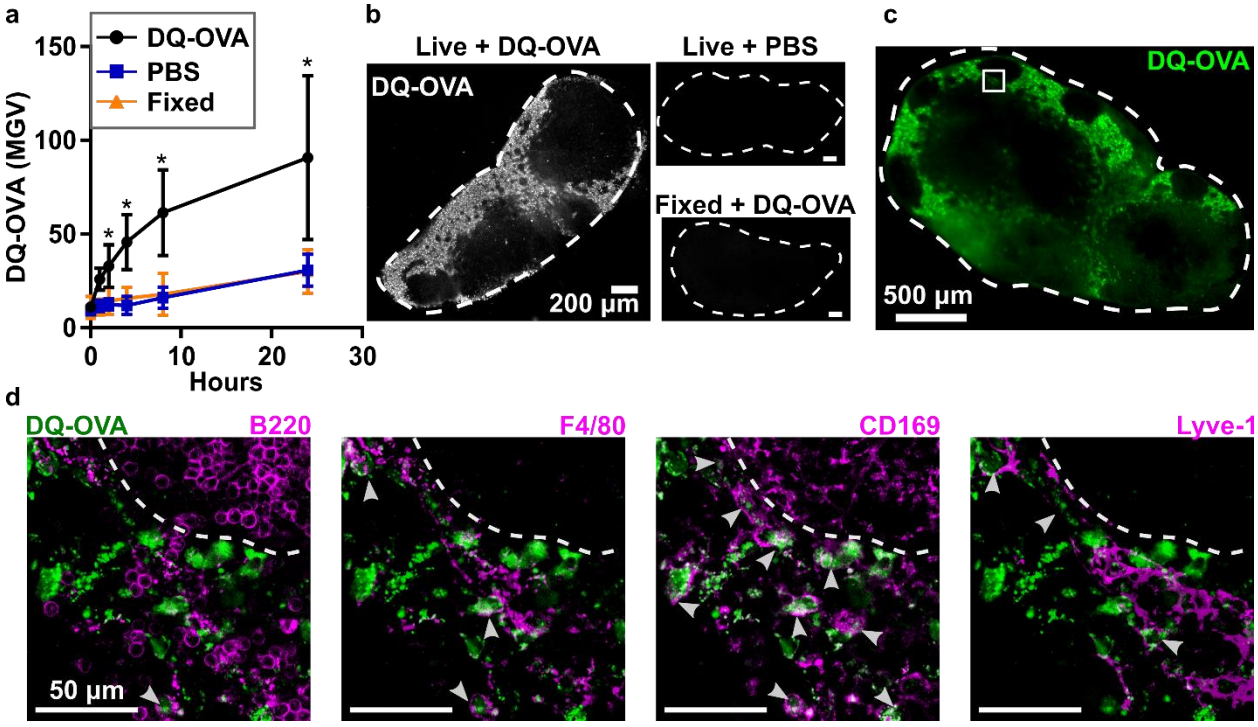

Figure 2.10: Slices processed protein antigen. (a) Mean grey value (MGV) of DQ-OVA in lymph node slices, showing processing of this protein antigen only in live slices. Live slices incubated with 1x PBS and fixed slices incubated with DQ-OVA served as negative controls. 2-way ANOVA with multiple comparisons. N = 9 slices, *p<0.05. (b) Representative images of slices from (a) after 4 hours of culture. Slices outlined with dashed white line. (c) Low-magnification, widefield image of DQ-OVA processed within a live slice after four hours. (d) Confocal images of a representative area of the slice, shown boxed in panel (c). Each panel includes DQ-OVA (green) overlaid with the indicated co-stain (purple). Dashed line indicates edge of B cell follicle. Arrowheads indicate cells that appear to have processed DQ-OVA.

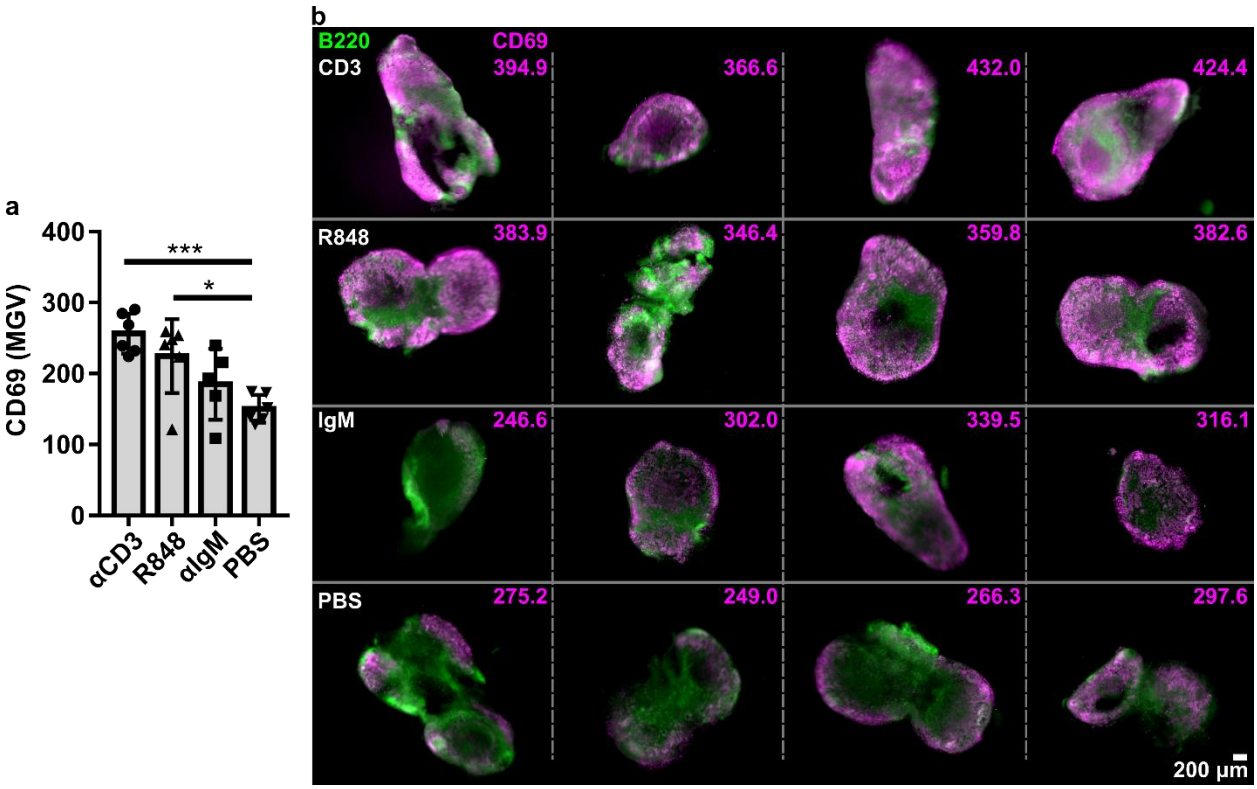

Figure 2.11: Slices responded to stimulation by upregulating surface expression of inflammation markers. (a) Mean pixel intensity of CD69, averaged within each slice, was increased after 24-hour stimulation with indicated reagents. One-way ANOVA with multiple comparisons. Each dot represents one slice. ***p=0.0005, *p=0.0110. (b) B220 (green) and CD69 (purple) immunofluorescence in representative lymph node after ex vivo stimulation with anti-CD3 (row 1), R848 (row 2), anti-IgM (row 3), and PBS (row 4). Mean grey value for the CD69 channel is reported in the upper right corner of each image. The PBS control samples had visible CD69 staining around the edges of the tissue, due to either natural high expression in naïve lymph nodes or off target/Fc-mediated binding fo the antibody in these regions. Slices stimulated with anti-CD3 or R848 both had elevated, somewhat punctate expression within cortical regions of the lymph node, which are rich in both B cells and T cells, and CD3-stimulated slices also had diffuse CD69 signal in the T cell-rich center.[3,4] Anti-IgM stimulation resulted in a uniform staining pattern but with much lower average intensity over the entire slice.

We next tested the extent to which lymph node slices were able to respond to the activation of T cells (anti-CD3, TCR engagement), B cells (anti-IgM, BCR engagement) and APCs (R848, a TLR7 agonist) in overnight cultures.[89–91] While anti-CD3 directly activates T cells by cross-linking the TCR, R848 acts on T cells indirectly by activating APCs to produce IL-12, which has a paracrine effect on nearby T cells.[92,93] Rather than analyze cellular-level responses, which is best done by traditional cell culture and flow cytometry, we focused on readouts that reflect tissue-level responses and multi-cell interactions, such as upregulation of the lymphocyte activation marker CD69. Statistically significant increases in mean CD69 surface staining were

induced by anti-CD3 and R848 but not anti-IgM (Figure 2.11a). These stimuli generated qualitative differences in CD69 staining patterns within the tissue; anti-CD3 elicited diffuse CD69 signal in the T cell-rich paracortex, while other stimuli did not (Figure 2.11b). Notably, anti-CD3 elicited these responses without inclusion of anti-CD28, suggesting that the co-stimulatory signal was adequately provided by the CD80/86 on APCs present within the tissue slice.

We further tested the response of lymph node slices to ex vivo stimulation with anti-CD3 and R848 in terms of cytokine secretion, and directly compared the response of slices to lymphocyte suspensions at matched cell densities. As expected, both tissue slices and cell cultures responded to anti-CD3 with secretion of IFN-γ and IL-2, and unstimulated samples did not secrete measurable IFN-γ or IL-2 (Figure 2.12a,b). Interestingly, we observed up to an 18-fold increase in IFN-γ but not IL-2 secretion in tissue slices compared to cell culture. Stimulation with R848 also resulted in significantly higher levels of IFN-γ production compared to lymphocyte culture (Figure 2.12c). In fact, the lymphocyte response to these concentrations of R848 was very weak, possibly due to the relative scarcity of matrix-bound APCs in lymphocyte cell cultures.[94,95] Splenocyte culture has a higher population of APCs compared to lymphocytes, and splenocytes did have a detectable response to R848, though still lower than lymph node slices (Figure 2.12d).[96,97] We speculate that the integrity of lymphocyte contacts with stromal cells and antigen-presenting cells (e.g. providing CD28 ligation), as well as the integrity of matrix-bound secreted factors, may play a role in differences between slices and cells. These data are consistent with prior reports that the cytokine profile from ex vivo-stimulated human tonsil and spleen slices differed from that of matched tonsil cell and splenocyte cultures.[61,98] We conclude that lymph node slices can respond to ex vivo stimulation with both surface marker upregulation and cytokine secretion. Furthermore, differences between ex vivo and in vitro responses suggest that preserving the cell-cell and cell-ECM interactions that are seen in vivo may have a substantial impact on experimental results.

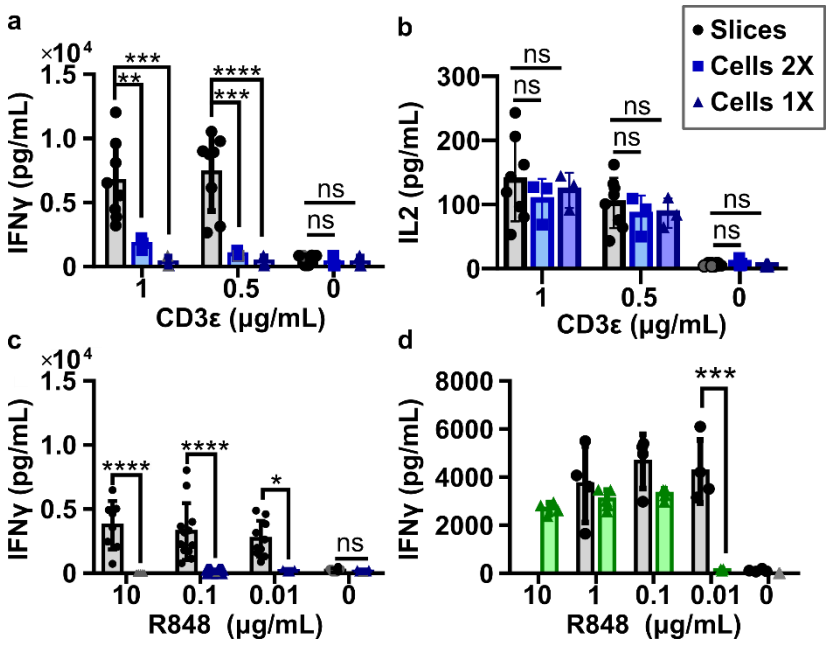

Figure 2.12: Slices produced measurable cytokine levels after stimulation. Cytokine secretion from slices and mixed cell culture after 20-hour direct (CD3ε) or indirect (R848) T cell stimulation. Cell concentration was matched to LN slice, 1X: 1.7 x10^6 cells/mL, 2X: 3.4 x10^6 cells/mL. (a) IFNγ secretion after 20-hr stimulation with CD3Ɛ vs lymphocytes. (b) IL-2 secretion after 20-hr stimulation with CD3ε vs lymphocytes. (c) IFNγ secretion after 20-hr stimulation with R848 vs lymphocytes. (d) IFNγ secretion after 20-hr stimulation with R848 vs splenocytes. Grey dots represent points set to the LOD; each dot represents one slice/cell culture. N = 6-12 slices and 3-4 cell cultures. Mean ± Standard Deviation. 2-way ANOVA with multiple comparisons. *p=0.0102, **p=0.0029, ***p=.00001, ****p<0.0001, n.s. denotes p>0.05. Data collected by A. Kinman.

2.3.7 Live lymph node slices responded to antigen-specific challenge

Finally, we tested the ability of lymph node slices to recall an antigen-specific response ex vivo. In vivo vaccination elicits a complex series of responses, including antigen trafficking and processing, cellular activation, and cytokine secretion, at specific times that reflect the ongoing development of the adaptive immune response. Here we tested a subset of these readouts to assess the ability of ex vivo lymph node slices to report on this in vivo activity. Taking advantage of the OVA/OTII model antigen system, mice received OVA-transgenic CD4+ T cells (OTII) intravenously, then were primed subcutaneously (s.c.) with either a model vaccine (alum and OVA protein) or a vehicle control (PBS) (Figure 2.13a). In this system we expected to measure adjuvant-mediated and initial T cell responses between days 1 and 4, with a full T cell response

by day 7.[99] Alum vaccines are known to produce a Th2-skewed response, and we expected to see this polarization in our slice culture system in the form of IL-4 secretion.[100,101]

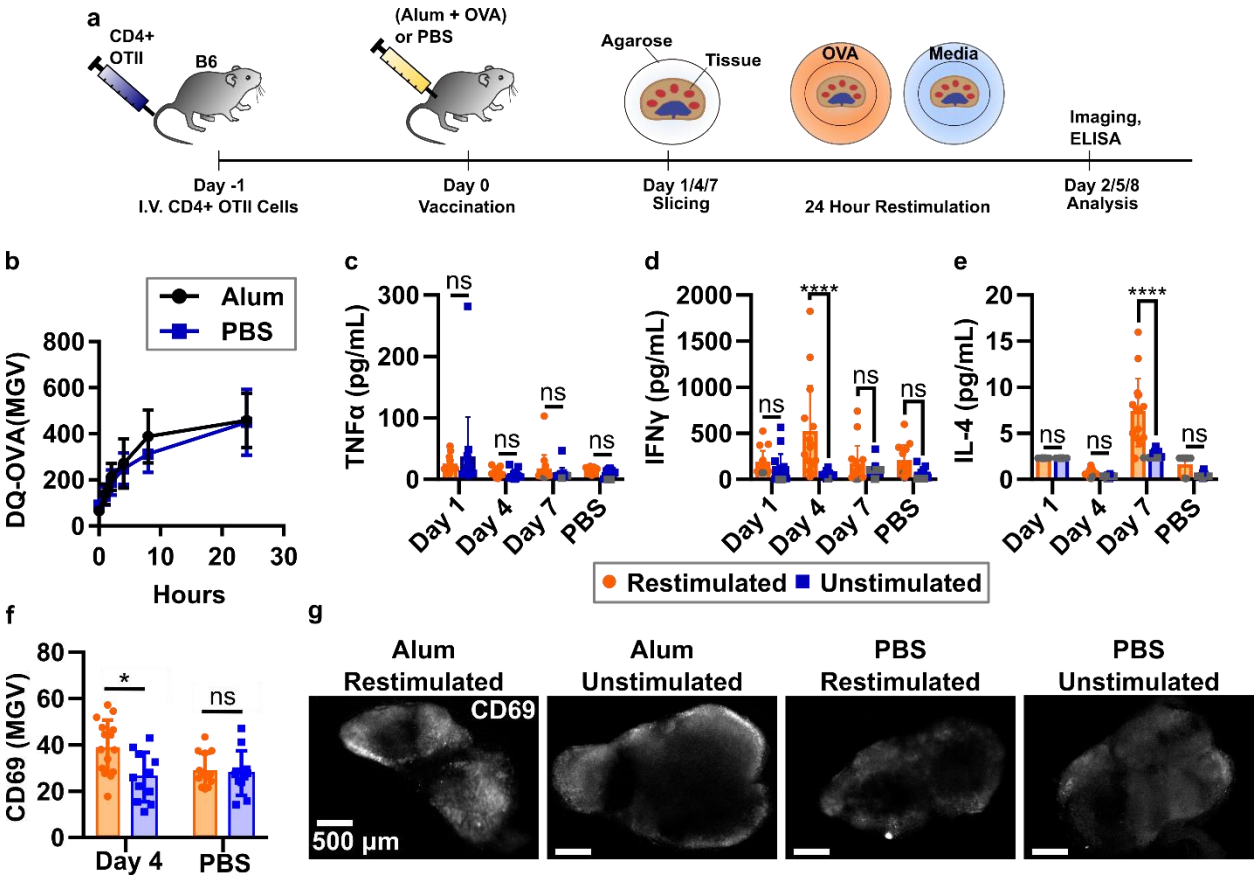

Figure 2.13: Lymph node slices showed antigen-specific stimulation after vaccination. (a) Schematic of experimental procedure. Black/6 mice were given CD4+ OTII cells IV and rested one day before vaccination with either alum and OVA protein or PBS. Tissues were collected on 1, 4, and 7 days after vaccination and sliced. Slices were then cultured with or without OVA protein challenge for 24 hours. Cytokine analysis was completed by ELISA from surrounding media and slices were immunostained for activation markers. (b) Slices from mice vaccinated with alum+OVA four days prior processed OVA antigen at the same rate as those from unvaccinated mice. N=12 slices. (c-d) Quantification of cytokine secretion into the culture media after 24-hr culture with or without OVA. Antigen-specific IFN-γ response was detected on day 4; antigen-specific IL-2 response was detected on day 7. Dark grey points represent data that was set at the limit of detection for the plate. (f) Antigen-specific CD69 upregulation was seen on day 4. (g) Representative images from (f). Slices were stained with FITC-B220 and AF647-CD69. Scalebars all 500 µm. Each dot represents a single slice with bars indicating mean ± standard deviation. Two-way ANOVA with multiple comparisons. *p<0.05, **p<0.01. Panels c-g data collected by A. Ball and M. Catterton

Because activated APCs may decrease their phagocytic properties,[102] we first tested whether cells in lymph node slices from vaccinated mice were able to process DQ-OVA on this time scale. Unexpectedly, DQ-OVA processing in these slices was unchanged compared to slices from control animals (Figure 2.13b). We speculate that the unaltered processing of DQ-OVA in the lymph node may be due to the presence of lymph-node resident DCs that were not activated by the s.c. alum injection. This result indicated that ex vivo incubation with antigen would still be effective in lymph node slices from vaccinated animals.

To quantify early and late responses to vaccination, lymph nodes were collected on days 1, 4, and 7 after vaccination, sliced, and cultured for 24-hr in the presence or absence of OVA protein in the media. TNFα secretion was not detectable at any time point (Figure 2.13c), consistent with other reports for alum adjuvants.[103,100] By day 4, a strong antigen-specific IFNγ response was detected in slices from vaccinated animals (Figure 2.13d). Slices from control animals did not secrete IFNγ upon ex vivo culture with OVA, confirming that the response arose from vaccination. Consistent with the timing of the IFNγ response, on day 4 we also observed a significant increase in CD69 surface marker immunofluorescence in vaccinated/restimulated slices compared to vaccinated/unstimulated and vehicle controls (Figure 2.13f). CD69 upregulation was located throughout the slice (Figure 2.13g, Figure 2.14). No CD69 upregulation was detected on days 1 or 7 (not shown). As expected for an alum-adjuvanted vaccine,[99,101] we observed a statistically significant increase in antigen-specific IL-4 production in lymph node slices from vaccinated animals (Figure 2.13e). Interestingly, the peak days for IFN-γ and IL-4 differed (days 4 and 7, respectively), providing information about the kinetics of cytokine secretion during the in vivo immune response. In summary, these data provide compelling evidence that murine lymph node slices can mount antigen-specific responses ex vivo, including to intact protein antigens. Slice cultures simultaneously yielded data on the timing of cytokine secretion and the distribution of immunofluorescence staining, and could match trends across the results. Overall,

these data show the versatility of live lymph node tissue slices to provide multiple readouts and potentially serve as an ex vivo model of immunity.

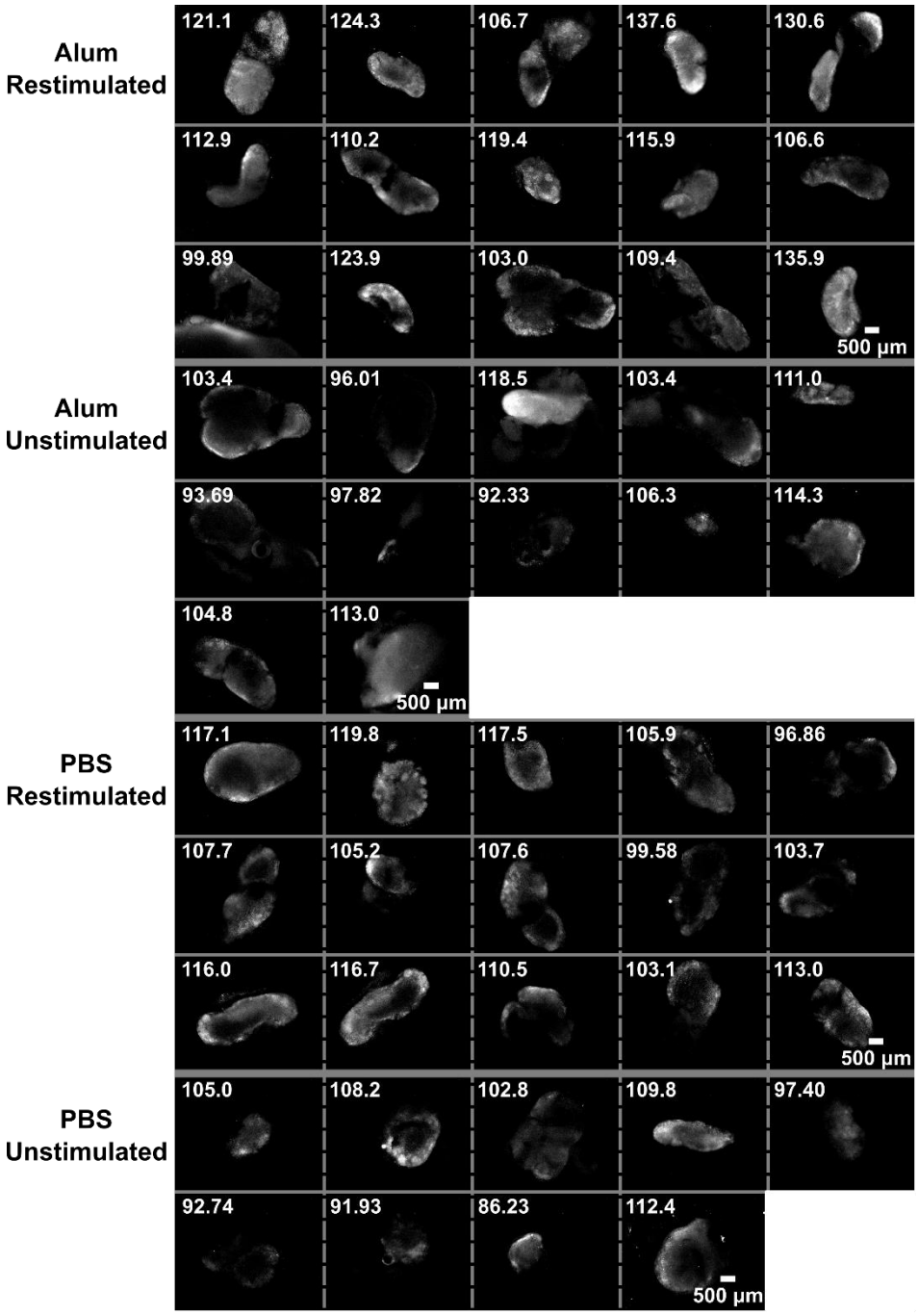

Figure 2.14: **Lymph node slices from vaccinated mice responded to protein-antigen challenge by upregulating surface expression of inflammatory markers.** Mice received i.v. OTII CD4+ T cells, then were immunized with either OVA+Alum (noted as Alum in the figure) or PBS. Slices from draining lymph nodes were collected on Day 4 and cultured ex vivo for 24 hours with either whole-protein OVA (Restimulated) or PBS (Unstimulated). Slices were then stained with AF647-CD69. Mean grey values for the CD69 channel is reported in each image. Data collected by A. Ball and M. Catterton.

2.4 DISCUSSION

The data in this chapter lay out a set of best practices for slicing murine lymph nodes and maintaining them in 24-hr culture, and demonstrate that slices have the potential to be used to study T cell activation and antigen-specific responses ex vivo. Slices retained viability for 24 hours in culture and did not show signs of inflammation. Slices retained the spatial organization seen in vivo while making the tissue readily accessible for imaging and immunostaining, offering the potential to easily image cellular interactions and changes in surface marker expression during culture. Lymph node slices offered a cytokine response that differed in some cases from lymphocyte culture, consistent with prior reports for other lymphoid tissues.[58,61] This difference may reflect the intact extracellular environment and cell-cell interactions that would be found in vivo. Most interestingly, this work provided evidence that lymph node slices could be used to report antigen-specific responses to vaccination, while offering the ability for multi-modal readout that combines imaging and traditional analysis such as ELISA and flow cytometry. Overall, this work lays the foundation for lymph node slices to serve as a controlled, ex vivo experimental platform in which to study the spatial organization and dynamics of the lymph node.

Traditionally, antigen presentation studies have been conducted by in vitro cell culture or by in vivo imaging, frequently using DCs pulsed with protein or peptide antigen.[70,73] By using intact tissue ex vivo instead of co-culturing T cells with DCs in vitro, the contributions other cell types are retained, e.g. fibroblastic reticular cells (FRCs), with which T cells interact with at a higher frequency than with DCs.[104] We note that pulsed DC cultures could, in principle, be overlaid onto ex vivo lymph node slices for facile imaging of T cell-DC interactions similar to the in vivo studies, although overlays likely would not produce the fine segregation of DC phenotypes seen in vivo.[70,73,95] Here, the lymph node was primed in vivo, then challenged ex vivo with a protein antigen in a manner similar to traditional ELIspot assays. The finding that cells in LN slices were able to process protein antigen for antigen-specific T cell activation opens the possibility for ex

vivo analysis of intercellular interactions as well as antigenicity analysis. In contrast, peptides may load onto any available MHC, potentially introducing cellular interactions that would not traditionally occur. Furthermore, antigen-presenting cells were presumably present in same numbers and locations as they were in vivo.

Like any model system, ex vivo platforms have inherent features and limitations that impact experimental design. Ex vivo lymph node slices are characterized by heterogeneity, isolation from the organ, and exposure to the culture media that differs from the in vivo system. (1) Heterogeneity. The complex internal architecture of the lymph node results in each slice being distinct in both cellular distribution and available treatment surface area, despite all nodes being sliced along the transverse plane. This heterogeneity can lead to highly variable data sets, which can be addressed by either increasing sample size or by pre-selecting slices based on objective criteria, such as B220 intensity or slice area. On the other hand, it may be possible to take advantage of this feature to tease out differences in responses in varying parts of the organ. For many of our studies we preferred to keep the heterogeneous distribution as a representation of biological complexity. (2) Isolation. Once the tissue has been removed from the body, no additional cells can be recruited from other areas, such as memory B cells from the bone marrow or circulating T cells from the blood stream.[105,106] However, cells can be overlaid onto the slice ex vivo at defined concentrations and times, offering a powerful method to test the impact of specific cell types at known time points.[56,63] Removal from the body also eliminates blood, lymphatic, and interstitial fluid flow, so shear stress is altered compared to what the organ is exposed to in vivo. This limitation is also present in standard lymphocyte cultures, and may have an impact on stromal cells in particular.[107] Flow can be introduced into the system either through the tissue by gravity, or across the tissue with pumps,[54] with control over flow rates to mimic different disease states in vivo and offer greater control of the experimental system. Microfluidics in particular can offer a controlled approach for both the perfusion of tissue and potentially long-term culture.[108–110] (3)

Route of access. Drugs, cells, and other stimuli added to the culture media over a lymph node slice can enter the entire cut surface of the tissue, rather than being restricted to enter through the lymphatic or blood vasculature. This means that ex vivo slice treatment should not be used to report in vivo biodistribution, although uptake may still be somewhat selective based on regional cell activity (e.g. DQ-OVA uptake in Figure 2.10b, and regional T cell homing reported previously[63]). On the other hand, this feature makes it possible to deliver stimuli to controlled locations rather than being limited by natural biodistribution mechanisms.[49,51,111]

2.5 Conclusions and Future Work

As discussed above this data is fundamental to working with live lymph node slices as a way to study novel immunology. We are optimistic that live lymph node slices will provide a novel platform that will add to the immunologist's tool box as a supplement to traditional experimental models. Slices provide a new angle of investigation based on spatially organized and dynamic cell-cell and cell-matrix interactions, coupled with the responses to well defined ex vivo stimulation. The enduring success of brain, lung, and tumor slices to study cellular and tissue-level events, pharmacological responses, and even response to damage and infection, indicates the wide array of potential utility for lymph node slices. Indeed, human tonsil slices are already in use in this manner,[46,112] and it seems likely that use with transgenic animals and animal models of disease will prove equally fruitful. Lymph node slices may also prove useful for monitoring the effect of the immune system on other organs, e.g. by co-culturing lymph node tissue with cells and tissues from elsewhere in the body, in a far simpler manner than is possible in vivo.[54] In summary, the methods for collecting and working with acute murine lymph node slices presented here provide a basis for the use of this model system to study dynamics and cellular interactions; applications may span the range of vaccine development, infectious disease, cancer immunity, and autoimmunity.

Looking ahead, it will be useful to increase the longevity of the cultures to several days or weeks, to monitor an immune response from onset to completion ex vivo. Long term culture poses several challenges, including nutrient supplementation and oxygenation of the tissue, as well as retention of motile lymphocytes within the slices. As they currently stand, lymph node slices are able to provide valuable insight into short-term immune functions. Increasing the longevity will hinge on the ability to recapitulate in vivo conditions. I hypothesize that the main contributor will be the addition of fluid flow as this should stimulate the stromal cells to produce chemokines to increase cell retention.[107] After cell retention has been addressed media supplementation should only be necessary to support immunological activity.

2.6 REFERENCES

1 Qi H, Kastenmüller W, Germain RN. Spatiotemporal basis of innate and adaptive immunity in secondary lymphoid tissue. *Annu Rev Cell Dev Biol* 2014; **30**: 141–167.

2 Gaylo A, Schrock DC, Fernandes NRJ, Fowell DJ. T cell interstitial migration: Motility cues from the inflamed tissue for micro- and macro-positioning. *Front Immunol* 2016; **7**. doi:10.3389/fimmu.2016.00428.

3 Gonzalez SF, Pitcher LA, Mempel T, Schuerpf F, Carroll MC. B cell acquisition of antigen in vivo. *Curr Opin Immunol* 2009; **21**: 251–257.

4 Willard-Mack CL. Normal structure, function, and histology of lymph nodes. *Toxicol Pathol* 2006; **34**: 409–424.

5 Thurley K, Gerecht D, Friedmann E, Höfer T. Three-dimensional gradients of cytokine signaling between T cells. *PLoS Comput Biol* 2015; **11**. doi:10.1371/journal.pcbi.1004206.

6 Lian J, Luster AD. Chemokine-guided cell positioning in the lymph node orchestrates the generation of adaptive immune responses. *Curr Opin Cell Biol* 2015; **36**: 1–6.

7 Vaday GG, Lider O. Extracellular matrix moieties, cytokines, and enzymes: dynamic effects on immune cell behavior and inflammation. *J Leukoc Biol* 2000; **67**: 149–159.

8 Schmitz ML, Weber A, Roxlau T, Gaestel M, Kracht M. Signal integration, crosstalk mechanisms and networks in the function of inflammatory cytokines. *Biochim Biophys Acta BBA - Mol Cell Res* 2011; **1813**: 2165–2175.

9 Germain RN, Bajénoff M, Castellino F, Chieppa M, Egen JG, Huang AYC *et al.* Making friends in out-of-the-way places: how cells of the immune system get together and how they conduct their business as revealed by intravital imaging. *Immunol Rev* 2008; **221**: 163–181.

10 Kastenmüller W, Torabi-Parizi P, Subramanian N, Lämmermann T, Germain RN. A spatially-organized multicellular innate immune response in lymph nodes limits systemic pathogen spread. *Cell* 2012; **150**: 1235–1248.

11 Pompano RR, Chiang AH, Kastrup CJ, Ismagilov RF. Conceptual and experimental tools to understand spatial effects and transport Phenomena in Nonlinear Biochemical Networks Illustrated with Patchy Switching. 2017; **86**: 333–356.

12 Saeys Y, Van Gassen S, Lambrecht BN. Computational flow cytometry: helping to make sense of high-dimensional immunology data. *Nat Rev Immunol* 2016; **16**: 449–462.

13 Spitzer MH, Nolan GP. Mass cytometry: single cells, many features. *Cell* 2016; **165**: 780–791.

14 Faley S, Seale K, Hughey J, Schaffer DK, VanCompernolle S, McKinney B *et al.* Microfluidic platform for real-time signaling analysis of multiple single T cells in parallel. *Lab Chip* 2008; **8**: 1700–1712.

15 Ogunniyi AO, Thomas BA, Politano TJ, Varadarajan N, Landais E, Poignard P *et al.* Profiling human antibody responses by integrated single-cell analysis. *Vaccine* 2014; **32**: 2866–2873.

16 Han Q, Bradshaw EM, Nilsson B, Hafler DA, Love JC. Multidimensional analysis of the frequencies and rates of cytokine secretion from single cells by quantitative microengraving. *Lab Chip* 2010; **10**: 1391.

17 Xue Q, Lu Y, Eisele MR, Sulistijo ES, Khan N, Fan R *et al.* Analysis of single-cell cytokine secretion reveals a role for paracrine signaling in coordinating macrophage responses to TLR4 stimulation. *Sci Signal* 2015; **8**: ra59.

18 Chattopadhyay PK, Gierahn TM, Roederer M, Love JC. Single-cell technologies for monitoring immune systems. *Nat Immunol* 2014; **15**: 128–135.

19 Shalek AK, Satija R, Shuga J, Trombetta JJ, Gennert D, Lu D *et al.* Single-cell RNA-seq reveals dynamic paracrine control of cellular variation. *Nature* 2014; **510**: 363–369.

20 Consortium TTM, Quake SR, Wyss-Coray T, Darmanis S. Transcriptomic characterization of 20 organs and tissues from mouse at single cell resolution creates a Tabula Muris. *bioRxiv* 2017; : 237446.

21 Everts B. Metabolomics in immunology research. *Methods Mol Biol Clifton NJ* 2018; **1730**: 29–42.

22 Wu M, Neilson A, Swift AL, Moran R, Tamagnine J, Parslow D *et al.* Multiparameter metabolic analysis reveals a close link between attenuated mitochondrial bioenergetic function and enhanced glycolysis dependency in human tumor cells. *Am J Physiol Cell Physiol* 2007; **292**: C125-136.

23 Shakhar G, Lindquist RL, Skokos D, Dudziak D, Huang JH, Nussenzweig MC *et al.* Stable T cell-dendritic cell interactions precede the development of both tolerance and immunity in vivo. *Nat Immunol* 2005; **6**: 707–714.

24 Matheu MP, Parker I, Cahalan MD. Dissection and 2-photon imaging of peripheral lymph nodes in mice. *J Vis Exp JoVE* 2007. doi:10.3791/265.

25 Liu Z, Gerner MY, Panhuys NV, Levine AG, Rudensky AY, Germain RN. Immune homeostasis enforced by co-localized effector and regulatory T cells. *Nature* 2015; **528**: 225–230.

26 Germain RN, Robey EA, Cahalan MD. A decade of imaging cellular motility and interaction dynamics in the immune system. *Science* 2012; **336**: 1676–1681.

27 Dzhagalov IL, Melichar HJ, Ross JO, Herzmark P, Robey EA. Two-photon imaging of the immune system. *Curr Protoc Cytom Editor Board J Paul Robinson Manag Ed Al* 2012; **Chapter 12**: Unit12.26.

28 Rodda LB, Lu E, Bennett ML, Sokol CL, Wang X, Luther SA *et al.* Single-cell RNA sequencing of lymph node stromal cells reveals niche-associated heterogeneity. *Immunity* 2018; **48**: 1014-1028.e6.

29 Goltsev Y, Samusik N, Kennedy-Darling J, Bhate S, Hale M, Vazquez G *et al.* Deep profiling of mouse splenic architecture with CODEX multiplexed imaging. *Cell* 2018; **174**: 968-981.e15.

30 Stoler-Barak L, Biram A, Davidzohn N, Addadi Y, Golani O, Shulman Z. B cell dissemination patterns during the germinal center reaction revealed by whole-organ imaging. *J Exp Med* 2019; **216**: 2515–2530.

31 Gosselin EA, Eppler HB, Bromberg JS, Jewell CM. Designing natural and synthetic immune tissues. *Nat Mater* 2018; **17**: 484–498.

32 Manifold MC. The effect of certain antiseptics on the respiration of brain tissues in vitro. *Br J Exp Pathol* 1941; **22**: 111–126.

33 Rafaelsen OJ. Action of insulin on glucose uptake of rat brain slices and isolated rat cerebellum. *J Neurochem* 1961; **7**: 45–51.

34 Yamamoto C, McIlwain H. Electrical activities in thin sections from the mammalian brain maintained in chemically-defined media in vitro. *J Neurochem* 1966; **13**: 1333–1343.

35 Collingridge GL. The brain slice preparation: a tribute to the pioneer Henry McIlwain. *J Neurosci Methods* 1995; **59**: 5–9.

36 Buskila Y, Breen PP, Tapson J, Schaik A van, Barton M, Morley JW. Extending the viability of acute brain slices. *Sci Rep* 2014; **4**: 5309.

37 De Simoni A, MY Yu L. Preparation of organotypic hippocampal slice cultures: interface method. *Nat Protoc* 2006; **1**: 1439–1445.

38 Marciniak A, Cohrs CM, Tsata V, Chouinard JA, Selck C, Stertmann J *et al.* Using pancreas tissue slices for in situ studies of islet of Langerhans and acinar cell biology. *Nat Protoc* 2014; **9**: 2809–2822.

39 Olinga P, Schuppan D. Precision-cut liver slices: a tool to model the liver ex vivo. *J Hepatol* 2013; **58**: 1252–1253.

40 Henjakovic M, Sewald K, Switalla S, Kaiser D, Müller M, Veres TZ *et al.* Ex vivo testing of immune responses in precision-cut lung slices. *Toxicol Appl Pharmacol* 2008; **231**: 68–76.

41 Wang K, Lee P, Mirams GR, Sarathchandra P, Borg TK, Gavaghan DJ *et al.* Cardiac tissue slices: preparation, handling, and successful optical mapping. *Am J Physiol - Heart Circ Physiol* 2015; **308**: H1112–H1125.

42 Allen CDC, Cyster JG. Follicular dendritic cell networks of primary follicles and germinal centers: phenotype and function. *Semin Immunol* 2008; **20**: 14–25.

43 Fletcher AL, Acton SE, Knoblich K. Lymph node fibroblastic reticular cells in health and disease. *Nat Rev Immunol* 2015; **15**: 350–361.

44 Chang JE, Turley SJ. Stromal infrastructure of the lymph node and coordination of immunity. *Trends Immunol* 2015; **36**: 30–39.

45 Gerner MY, Kastenmuller W, Ifrim I, Kabat J, Germain RN. Histo-Cytometry: A method for highly multiplex quantitative tissue imaging analysis applied to dendritic cell subset microanatomy in lymph nodes. *Immunity* 2012; **37**: 364–376.

46 Grivel J-C, Margolis L. Use of human tissue explants to study human infectious agents. *Nat Protoc* 2009; **4**: 256–269.

47 Mohammed JS, Caicedo HH, Fall CP, Eddington DT. Microfluidic add-on for standard electrophysiology chambers. *Lab Chip* 2008; **8**: 1048–1055.

48 Salmon H, Rivas-Caicedo A, Asperti-Boursin F, Lebugle C, Bourdoncle P, Donnadieu E. Ex vivo imaging of T cells in murine lymph node slices with widefield and confocal microscopes. *J Vis Exp* 2011. doi:10.3791/3054.

49 Ross AE, Belanger MC, Woodroof JF, Pompano RR. Spatially resolved microfluidic stimulation of lymphoid tissue ex vivo. *Analyst* 2017; **142**: 649–659.

50 Groff BD, Kinman AWL, Woodroof JF, Pompano RR. Immunofluorescence staining of live lymph node tissue slices. *J Immunol Methods* 2018. doi:10.1016/j.jim.2018.10.010.

51 Ross AE, Pompano RR. Diffusion of cytokines in live lymph node tissue using microfluidic integrated optical imaging. *Anal Chim Acta* 2018; **1000**: 205–213.

52 Ross JennyO, Melichar HeatherJ, Halkias J, Robey EllenA. Studying T cell development in thymic slices. In: Bosselut R, S. Vacchio M, Vacchio MS (eds). *T-Cell Development*. Springer New York, 2016, pp 131–140.

53 Hensley AL, Colley AR, Ross AE. Real-time detection of melatonin using fast-scan cyclic voltammetry. *Anal Chem* 2018; **90**: 8642–8650.

54 Shim S, Belanger MC, Harris AR, Munson JM, Pompano RR. Two-way communication between ex vivo tissues on a microfluidic chip: application to tumor-lymph node interaction. *Lab Chip* 2019; **19**: 1013–1026.

55 Low LA, Tagle DA. Microphysiological systems (tissue chips) and their utility for rare disease research. In: Posada de la Paz M, Taruscio D, Groft SC (eds). *Rare Diseases Epidemiology: Update and Overview*. Springer International Publishing: Cham, 2017, pp 405–415.

56 Ross JO, Melichar HJ, Halkias J, Robey EA. Studying T cell development in thymic slices. *Methods Mol Biol Clifton NJ* 2016; **1323**: 131–140.

57 Lancaster JN, Ehrlich LIR. Analysis of thymocyte migration, cellular interactions, and activation by multiphoton fluorescence microscopy of live thymic slices. *Methods Mol Biol Clifton NJ* 2017; **1591**: 9–25.

58 Hoffmann P, Skibinski G, James K. Organ culture of human lymphoid tissue. I. Characteristics of the system. *J Immunol Methods* 1995; **179**: 37–49.

59 Skibinski G, Hoffmann P, Radbruch A, James K. Organ culture of human lymphoid tissue. II. Marked differences in cytokine production and proliferation between slice and suspension cultures of human spleen. *J Immunol Methods* 1997; **205**: 115–125.

60 Knoblich K, Cruz Migoni S, Siew SM, Jinks E, Kaul B, Jeffery HC *et al.* The human lymph node microenvironment unilaterally regulates T-cell activation and differentiation. *PLOS Biol* 2018; **16**: e2005046.

61 Giger B, Bonanomi A, Odermatt B, Ladell K, Speck RF, Kojic D *et al.* Human tonsillar tissue block cultures differ from autologous tonsillar cell suspension cultures in lymphocyte subset activation and cytokine gene expression. *J Immunol Methods* 2004; **289**: 179–190.

62 Asperti-Boursin F, Real E, Bismuth G, Trautmann A, Donnadieu E. CCR7 ligands control basal T cell motility within lymph node slices in a phosphoinositide 3–kinase– independent manner. *J Exp Med* 2007; **204**: 1167–1179.

63 Salmon H, Rivas-Caicedo A, Asperti-Boursin F, Lebugle C, Bourdoncle P, Donnadieu E. Ex vivo imaging of T cells in murine lymph node slices with widefield and confocal microscopes. *J Vis Exp JoVE* 2011; : e3054.

64 Katakai T, Habiro K, Kinashi T. Dendritic cells regulate high-speed interstitial T cell migration in the lymph node via LFA-1/ICAM-1. *J Immunol* 2013; **191**: 1188–1199.

65 Katakai T, Kondo N, Ueda Y, Kinashi T. Autotaxin produced by stromal cells promotes LFA-1–independent and rho-dependent interstitial T cell motility in the lymph node paracortex. *J Immunol* 2014; **193**: 617–626.

66 Katakai T. Live imaging of interstitial T cell migration using lymph node slices. In: Ishii M (ed). *Intravital Imaging of Dynamic Bone and Immune Systems : Methods and Protocols*. Springer New York: New York, NY, 2018, pp 29–42.

67 Schneider CA, Rasband WS, Eliceiri KW. NIH image to ImageJ: 25 years of image analysis. *Nat Methods* 2012; **9**: 671–675.

68 Asperti-Boursin F, Real E, Bismuth G, Trautmann A, Donnadieu E. CCR7 ligands control basal T cell motility within lymph node slices in a phosphoinositide 3–kinase– independent manner. *J Exp Med* 2007; **204**: 1167–1179.

69 Gerner MY, Kastenmuller W, Ifrim I, Kabat J, Germain RN. Histo-cytometry: A method for highly multiplex quantitative tissue imaging analysis applied to dendritic cell subset microanatomy in lymph nodes. *Immunity* 2012; **37**: 364–376.

70 Stoll S, Delon J, Brotz TM, Germain RN. Dynamic imaging of T cell-dendritic cell interactions in lymph nodes. *Science* 2002; **296**: 1873–1876.

71 Garside P. Visualization of Specific B and T lymphocyte interactions in the lymph node. *Science* 1998; **281**: 96–99.

72 Moran I, Nguyen A, Khoo WH, Butt D, Bourne K, Young C *et al.* Memory B cells are reactivated in subcapsular proliferative foci of lymph nodes. *Nat Commun* 2018; **9**. doi:10.1038/s41467-018-05772-7.

73 Malide D. In vivo cell tracking using two-photon microscopy. In: Bai M (ed). *In Vivo Fluorescence Imaging: Methods and Protocols*. Springer New York: New York, NY, 2016, pp 109–122.

74 Bajénoff M, Egen J, Koo LY, Laugier JP, Brau F, Glaichenhaus N *et al.* Stromal cell networks regulate lymphocyte entry, migration, and territoriality in lymph nodes. *Immunity* 2006; **25**: 989–1001.

75 Hume DA. Macrophages as APC and the dendritic cell myth. *J Immunol* 2008; **181**: 5829–5835.

76 Astolfi M, Péant B, Lateef MA, Rousset N, Kendall-Dupont J, Carmona E *et al.* Micro-dissected tumor tissues on chip: an ex vivo method for drug testing and personalized therapy. *Lab Chip* 2016; **16**: 312–325.

77 Craston R, Koh M, Mc Dermott A, Ray N, Prentice HG, Lowdell MW. Temporal dynamics of CD69 expression on lymphoid cells. *J Immunol Methods* 1997; **209**: 37–45.

78 Dilioglou S, Cruse JM, Lewis RE. Function of CD80 and CD86 on monocyte- and stem cell-derived dendritic cells. *Exp Mol Pathol* 2003; **75**: 217–227.

79 Sahoo NC, Rao KVS, Natarajan K. CD80 expression is induced on activated B cells following stimulation by CD86. *Scand J Immunol* 2002; **55**: 577–584.

80 Graaf IAM de, Meijeren CE van, Pektaş F, Koster HJ. Comparison of in vitro preparations for semi-quantitative prediction of in vivo drug metabolism. *Drug Metab Dispos* 2002; **30**: 1129–1136.

81 Graaf IAM de, Olinga P, Jager MH de, Merema MT, Kanter R de, Kerkhof EG van de *et al.* Preparation and incubation of precision-cut liver and intestinal slices for application in drug metabolism and toxicity studies. *Nat Protoc* 2010; **5**: 1540–1551.

82 Zenewicz LA. Oxygen levels and immunological studies. *Front Immunol* 2017; **8**. doi:10.3389/fimmu.2017.00324.

83 Buskila Y, Breen PP, Tapson J, van Schaik A, Barton M, Morley JW. Extending the viability of acute brain slices. *Sci Rep* 2014; **4**: 5309.

84 Papouin T, Haydon PG. Obtaining acute brain slices. *Bio-Protoc* 2018; **8**. doi:10.21769/BioProtoc.2699.

85 Gentek R, Bajénoff M. Lymph node stroma dynamics and approaches for their cisualization. *Trends Immunol* 2017; **38**: 236–247.

86 Davies EJ, Dong M, Gutekunst M, Närhi K, van Zoggel HJAA, Blom S *et al.* Capturing complex tumour biology *in vitro*: histological and molecular characterisation of precision cut slices. *Sci Rep* 2015; **5**: 17187.

87 Junt T, Moseman EA, Iannacone M, Massberg S, Lang PA, Boes M *et al.* Subcapsular sinus macrophages in lymph nodes clear lymph-borne viruses and present them to antiviral B cells. *Nature* 2007; **450**: 110–114.

88 Gray EE, Cyster JG. Lymph node macrophages. *J Innate Immun* 2012; **4**: 424–436.

89 Wagner TL, Ahonen CL, Couture AM, Gibson SJ, Miller RL, Smith RM *et al.* Modulation of TH1 and TH2 cytokine production with the immune response modifiers, R-848 and imiquimod. *Cell Immunol* 1999; **191**: 10–19.

90 Tomai MA, Imbertson LM, Stanczak TL, Tygrett LT, Waldschmidt TJ. The immune response modifiers imiquimod and R-848 are potent activators of B lymphocytes. *Cell Immunol* 2000; **203**: 55–65.

91 Jurk M, Heil F, Vollmer J, Schetter C, Krieg AM, Wagner H *et al.* Human TLR7 or TLR8 independently confer responsiveness to the antiviral compound R-848. *Nat Immunol* 2002; **3**: 499.

92 Rubtsova K, Rubtsov AV, Halemano K, Li SX, Kappler JW, Santiago ML *et al.* T Cell production of IFNγ in response to TLR7/IL-12 stimulates optimal B cell responses to viruses. *PLoS ONE* 2016; **11**. doi:10.1371/journal.pone.0166322.

93 Caron G, Duluc D, Frémaux I, Jeannin P, David C, Gascan H *et al.* Direct stimulation of human T cells via TLR5 and TLR7/8: Flagellin and R-848 up-regulate proliferation and IFN-γ production by memory CD4+ T cells. *J Immunol* 2005; **175**: 1551–1557.

94 Parmentier HK, van der Linden JA, Krijnen J, van Wichen DF, Rademakers LH, Bloem AC *et al.* Human follicular dendritic cells: isolation and characteristics in situ and in suspension. *Scand J Immunol* 1991; **33**: 441–452.

95 Gerner MY, Kastenmuller W, Ifrim I, Kabat J, Germain RN. Histo-cytometry: a method for highly multiplex quantitative tissue imaging analysis applied to dendritic cell subset microanatomy in lymph nodes. *Immunity* 2012; **37**: 364–376.

96 Shen E, Lu L, Wu C. TLR7/8 ligand, R-848, inhibits IgE synthesis by acting directly on B lymphocytes. *Scand J Immunol* 2008; **67**: 560–568.

97 Wang X, Li L, Wang J, Dong L, Shu Y, Liang Y *et al.* Inhibition of cytokine response to TLR stimulation and alleviation of collagen-induced arthritis in mice by Schistosoma japonicum peptide SJMHE1. *J Cell Mol Med* 2017; **21**: 475–486.

98 Hoffmann P, Skibinski G, James K. Organ culture of human lymphoid tissue. I. Characteristics of the system. *J Immunol Methods* 1995; **179**: 37–49.

99 Kim C, Fang F, Weyand CM, Goronzy JJ. The life cycle of a T cell after vaccination – where does immune ageing strike? *Clin Exp Immunol* 2017; **187**: 71–81.

100 Orr MT, Khandhar AP, Seydoux E, Liang H, Gage E, Mikasa T *et al.* Reprogramming the adjuvant properties of aluminum oxyhydroxide with nanoparticle technology. *Npj Vaccines* 2019; **4**: 1–10.

101 Kool M, Fierens K, Lambrecht BN. Alum adjuvant: some of the tricks of the oldest adjuvant. *J Med Microbiol* 2012; **61**: 927–934.

102 Trombetta ES, Mellman I. Cell biology of antigen processing in vitro and in vivo. *Annu Rev Immunol* 2005; **23**: 975–1028.

103 Mosca F, Tritto E, Muzzi A, Monaci E, Bagnoli F, Iavarone C *et al.* Molecular and cellular signatures of human vaccine adjuvants. *Proc Natl Acad Sci* 2008; **105**: 10501–10506.

104 Tasnim H, Fricke GM, Byrum JR, Sotiris JO, Cannon JL, Moses ME. Quantitative measurement of naïve T cell association with dendritic cells, FRCs, and blood vessels in lymph nodes. *Front Immunol* 2018; **9**. doi:10.3389/fimmu.2018.01571.

105 Shenoy GN, Chatterjee P, Kaw S, Mukherjee S, Rathore DK, Bal V *et al.* Recruitment of memory B cells to lymph nodes remote from the site of immunization requires an inflammatory stimulus. *J Immunol* 2012; **189**: 521–528.

106 Nolz JC. Molecular mechanisms of CD8+ T cell trafficking and localization. *Cell Mol Life Sci CMLS* 2015; **72**: 2461–2473.

107 Tomei AA, Siegert S, Britschgi MR, Luther SA, Swartz MA. Fluid flow regulates stromal cell organization and CCL21 expression in a tissue-engineered lymph node microenvironment. *J Immunol* 2009; **183**: 4273–4283.

108 van Midwoud PM, Groothuis GMM, Merema MT, Verpoorte E. Microfluidic biochip for the perifusion of precision-cut rat liver slices for metabolism and toxicology studies. *Biotechnol Bioeng* 2010; **105**: 184–194.

109 van Midwoud PM, Merema MT, Verpoorte E, Groothuis GMM. A microfluidic approach for in vitro assessment of interorgan interactions in drug metabolism using intestinal and liver slices. *Lab Chip* 2010; **10**: 2778–2786.

110 Komeya M, Kimura H, Nakamura H, Yokonishi T, Sato T, Kojima K *et al.* Long-term ex vivo maintenance of testis tissues producing fertile sperm in a microfluidic device. *Sci Rep* 2016; **6**: 1–10.

111 Catterton MA, Dunn AF, Pompano RR. User-defined local stimulation of live tissue through a movable microfluidic port. *Lab Chip* 2018; **18**: 2003–2012.

112 Davies FJ, Olme C, Lynskey NN, Turner CE, Sriskandan S. Streptococcal superantigen-induced expansion of human tonsil T cells leads to altered T follicular helper cell phenotype, B cell death and reduced immunoglobulin release. *Clin Exp Immunol* 2019; **197**: 83–94.

3 LABELLING PRIMARY IMMUNE CELLS USING BRIGHT BLUE FLUORESCENT NANOPARTICLES

3.1 INTRODUCTION

Tracking fluorescently labelled cells is a common strategy to assess cell behavior in vitro and in vivo, particularly for highly motile cells such as lymphocytes.[1–3] Many fluorescent dyes provide intracellular labelling by binding in the cytoplasm or to DNA, but labelling reagents continue to be an area of active research, particularly to take advantage of the further ends of the UV-visible spectrum.[4] Cytoplasmic labelling reagents are preferred for live cell imaging over time, as DNA-binding dyes can interrupt transcription and cell replication.[4,5] Common cytoplasmic dyes align well with standard green (Ex 470/40, Em 525/50) and red (Ex 550/25, Em 605/70) filter sets for widefield microscopy, including carboxyfluorescein succinimidyl ester (CSFE), calcein-AM, tetramethylrhodamine isothiocyanate (TRITC), and similar newer commercial fluorophores. However, the UV-excitable blue filter (Ex 365/50, Em 445/50) set is often underutilized for cell tracking.

Many traditional blue fluorophores, such as DAPI and Hoechst, bind directly to DNA, while others suffer from low intensities, such as derivatives of pyrene or coumarin.[6] Dim fluorescence signal under the classic UV-excited blue filter makes it difficult to distinguish labelled cells from tissue autofluorescence. Newer, brighter blue and violet fluorophores are available, but are primarily designed for multiplexed flow cytometry and laser-based microscopy, with a maximum excitation at either 405 or 395 nm and narrow excitation peaks. This makes translating the same dyes from one excitation source to another difficult; concentration, time of labelling, and detector sensitivity must be optimized for each read-out. A bright blue reagent that can be used across multiple platforms such as flow cytometry, confocal microscopy, and widefield fluorescent microscopy would enable a single optimized labelling procedure to be used with flexible choice of read-out.

Boron-based organic dyes serve as effective fluorescence reporters.[7–10] Previously, we reported luminescent difluoroboron β-diketonate (BF_2bdk) complexes as well suited for biomolecular imaging[11–14] and oxygen sensing.[15–18] Here we explore them as reagents for tracking cells in the blue channel. In particular, fluorescent BF_2bdk complexes offer outstanding optical properties such as large extinction coefficients and quantum yields,[19] two-photon absorption,[20] solvatochromism,[21] and photostability.[22] One of the brightest of these dyes, methoxy substituted difluoroboron dibenzoymethane (BF_2dbmOMe), emits intense blue fluorescence with a quantum yield approaching unity (Φ_F = 0.99).[23] This is significantly larger than most commercially available blue fluorophores (e.g., DAPI: Φ_F = 0.58;[24] pyrene: Φ_F = 0.75;[25] 7-hydroxy-4-methylcoumarin: Φ_F = 0.63 [26]). Therefore, we sought to harness this bright blue dye emission for *in vitro* and *ex vivo* imaging agents.

Boron-based fluorophores are often incorporated into a polymer matrix to improve their physical and chemical properties.[27] Many BF_2bdk complexes have large dipole moments (e.g., μ= 6.7 Debye for BF_2dbm), making their emission sensitive to the polarity of media and the local concentration. Therefore, emission spectra are tunable by varying the chemistry and/or length of the polymer chains, fabricated either in film or nanoparticle format.[28,29] Suitably chosen polymers also can increase solubility in aqueous solution and offer protection to the dye (e.g. against hydrolysis), improving their shelf life.[30] Poly($_{D,L}$-lactic acid) (PLA), a biocompatible and biodegradable material, has been utilized extensively for nanoparticle formation.[31] The first-generation boron-based polymer BF_2dbmPLA (Figure 3.1a-(1)), has found application in fluorescence imaging of cells and tissues, including intracellular uptake and oxygen sensing.[11,32] Poly ($_L$-lactic acid) (PLLA), a stereoisomer of PLA, offers a higher degree of crystallinity, which may slow the rate of hydrolysis in aqueous solution.[33,34] Poly (ε-caprolactone) (PCL) is a more hydrophobic polyester[35] that is even slower to degrade than PLLA, making it useful for extended retention of loaded cargo.[36,37] Blends of other polymers with PCL provide tunable properties useful

for drug delivery and tissue engineering applications.[38] Finally, although pure hydrophobic polymers can assemble as nanoparticles in water, hydrophilic segments, such as poly (ethylene glycol) (PEG), are often incorporated to enhance the water solubility for biological imaging and drug delivery.[12]

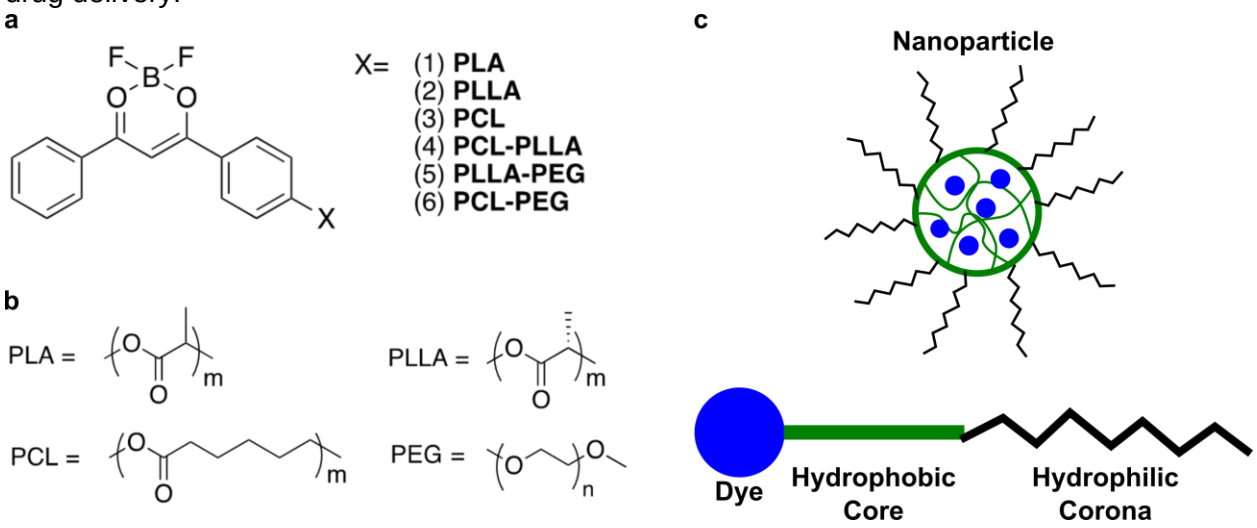

Figure 3.1: Nanoparticle design and compositions. (a) Chemical structures of boron-based dye-polymer conjugates. (b) Chemical structures of each polymer tested. (c) Schematic of polymeric nanoparticles, which adopt a micellar structure with the boron-based dye in the core and the polymer in the outer shell.

Well-controlled labelling of immune cells is of particular interest, as these highly motile cells are frequently tracked in vitro and in vivo, or labelled for flow cytometric analysis. Fabricating dye-polymer conjugates into nanoparticles offers the opportunity to tune its uptake by immune cells.[39] Lymphocytes (T cells and B cells), dendritic cells, and macrophages each have been targeted for delivery of drugs or probes by using nanoparticles.[39–42] Particles similar in size to viruses (20 – 200 nm) are readily internalized via endocytosis, particularly by phagocytic cells such as B cells or professional antigen presentation cells such as dendritic cells after adsorption of serum proteins.[43] Altering the hydrophobicity of the nanoparticle can significantly affect internalization,[40,44] and we hypothesized that PLA, PCL, and block co-polymers of PLA-PCL would exhibit differential uptake by endocytic cells.[45] Furthermore, PEGylation hinders particle uptake in

other systems, and we hypothesized that it would similarly prevent uptake of these boron-based nanoparticles.[46–49]

In this chapter, we tested the utility of labelling and tracking primary immune cells (murine splenocytes) with polymeric nanoparticles containing a blue boron-based fluorophore. After confirming the stability of the dyes and nanoparticles in solution, we assessed internalization and suitability for cellular staining as a function of polymer chemistry. We tested whether cells labelled with these reagents were detectable by fluorescent microscopy under standard blue fluorescence filter sets and compared to a commercial reagent, and utilized these particles to enable four-color fluorescent labelling and cell tracking in live tissue. This is the first demonstration of a materials-based blue fluorescent labelling reagent for cell tracking in the context of tissue autofluorescence.

3.2 Materials and Methods

3.2.1 Polymer synthesis and characterization

The boron-based dye was prepared as either a primary alcohol (BF_2dbmOCH_2CH_2OH)[31] or a phenol (BF_2dbmOH),[50] to act as an initiator or a coupler respectively.[51] These were used to synthesize polymer conjugates using methods similar to those previously described.[31,51] ^{1}H NMR spectra were recorded on a Varian VMRS/600 (600 MHz) instrument in $CDCl_3$ unless otherwise indicated. ^{1}H NMR resonance was referenced to the residual protiochloroform signal at 7.260 ppm. Coupling constants are given in hertz. Polymer molecular weights (MW) and polydispersity indices (Đ) were determined by gel permeation chromatography (GPC) (THF, 25 °C, 1.0 mL / min) using multi-angle laser light scattering (MALLS) (λ = 658 nm, 25 °C) and refractive index (RI) (λ = 658 nm, 25 °C) detection. Polymer Laboratories 5 µm mixed-C columns (guard column plus two columns) along with Wyatt Technology (Optilab T-rEX interferometric refractometer, miniDAWN TREOS multi-angle static light scattering (MALS) detector, ASTRA 6.0 software) and Agilent Technologies instrumentation (series 1260 HPLC with diode array (DAD) detector, ChemStation) were used in GPC analysis. The incremental refractive index (*dn*/*dc*) was

calculated by a single-injection method assuming 100% mass recovery from the columns. UV-vis spectra were recorded on a Hewlett-Packard 8452A diode-array spectrophotometer.

3.2.2 Luminescence measurements

Steady-state fluorescence spectra for the boron dye initiator, polymer and nanoparticle suspensions were recorded on a Horiba Fluorolog-3 Model FL3-22 spectrofluorometer (double-grating excitation and double-grating emission monochromator) after excitation. Optically dilute aqueous solutions of the nanoparticles, with absorbance <0.1 au, were prepared in 1 cm path length quartz cuvettes. Fluorescence spectra were obtained under ambient conditions (i.e., air, ~21% oxygen in volume).

3.2.3 Nanoparticle fabrication and characterization

Nanoparticles were fabricated as previously reported.[52] The polymer (~3.0 mg) was dissolved in DMF (3 mL), then the dye solution was added dropwise to rapidly stirred DI water (27 mL). The homogeneous mixture was stirred for 30 min, then the nanoparticle suspension was transferred into dialysis tubing (Specra/Pro, 12-14 kDa MWCO, Fisher Scientific) followed by dialysis against water for 24 hours. Nanoparticle size and polydispersity were analyzed by dynamic light scattering (DLS, Wyatt, DynaPro). Zeta potentials were determined by Zetasizer Nano Z (Malvern instruments, UK) and data were analyzed using DTS Nano software. UV-Vis absorbance was recorded by diluting ~1 mg/mL stock nanoparticle suspensions to 50 μg/mL in DI water. The extinction coefficient was estimated based on the Beer-Lambert law.

3.2.4 Nanoparticle stability

The stock suspensions of nanoparticles (1 mg/mL) were serially diluted (200, 100, 50, 20, 10 μg/mL) with DI water, PBS, water/glucose/serum, and supplemented RPMI. Each sample (100 μL) was injected into a 96-well microtiter plate. Mineral oil was added on the top of each well via syringe to form a thin layer to prevent evaporation. The plate was put into the DLS instrument,

protected from light, set to 37 °C and the sizes and polydispersities of the nanoparticles were recorded every 12 h for one week. Nanoparticle aggregates larger than 2000 nm exceed the DLS detection limit. Separately, samples were incubated at 37 °C for five days to obtain daily photographs, as well as the emission spectra, to capture evidence of aggregation and fluorescence changes. GPC was used to monitor the polymer molecular weights (i.e. polymer stability) before and after incubation for specified times. To prepare samples for GPC analysis, nanoparticle aliquots in water were freeze-dried then dissolved in THF for injection into the GPC instrument. The degradation of boron dyes and hydrolysis of polyester were also analyzed by ^{1}H NMR spectroscopy in $CDCl_3$.

3.2.5 Cell culture

All animal work was approved by the Animal Care and Use Committee of the University of Virginia under protocol #4042, and was conducted in compliance with guidelines from the University of Virginia Animal Care and Use Committee and the Office of Laboratory Animal Welfare at the National Institutes of Health (United States). Mice were housed in a vivarium and given food and water *ab libitium*. Spleens, and lymph nodes where appropriate, were collected from male and female C57Bl/6 mice aged 6-10 weeks (Jackson Laboratories, USA) after isoflurane anesthesia and cervical dislocation. To isolate splenocytes, the spleen was processed through a 70-µm pore size nylon filter (Fisher Scientific, USA) and rinsed with sterile 1x phosphate buffer saline (PBS) supplemented with 2% v/v fetal bovine serum (FBS, VWR, USA). Red blood cells were lysed and the cell suspension was filtered through a fresh 70-µm filter. Cell density was determined through trypan blue exclusion. Where noted, B cells were isolated from bulk splenocytes by using a B cell enrichment kit (StemCell Technologies, USA) based on negative magnetic selection, according to manufacturer instructions. For all overnight cultures, cells were cultured at a concentration of $1x10^6$ cells/mL in “complete RPMI;” RPMI (Lonza, 16-167F) supplemented with 10 % FBS (VWR, Seradigm USDA approved, 89510-186) 1x L-glutamine

(Gibco Life Technologies, 25030-081), 50 U/mL Pen/Strep (Gibco), 50 µM beta-mercaptoethanol (Gibco, 21985-023), 1 mM sodium pyruvate (Hyclone, GE USA), 1x non-essential amino acids (Hyclone, SH30598.01), and 20 mM HEPES (VWR, 97064-362) with 120 ng/mL IL-2 (Peprotech, USA).

3.2.6 Cell labelling

To minimize nanoparticle aggregation, cellular labelling with nanoparticles was performed in an isotonic glucose solution without saline. Splenocytes were resuspended at $10x10^6$ cells/mL in a solution of 5% w/v D-glucose and 2% v/v FBS in ultra-pure water (water-glucose-serum solution, or 1x WGS; components from Thermo Fisher). A staining solution was prepared by mixing 3 parts nanoparticle stock solution (1 mg/mL in water), 2 parts 10x WGS, and 5 parts water. The staining solution was mixed in equal volumes with the cell suspension. This resulted in a 1x WGS solution that contained cells at $5x10^6$ cells/mL with nanoparticles at 0.15 mg/mL. Cells were incubated, protected from light, at room temperature for 30 min, then washed and resuspended at $1x10^6$ cells/mL in supplemented RPMI.

To label with Cell Tracker™ Blue CMF_2HC (4-chloromethyl-6,8-difluoro-7-hydroxycoumarin, Invitrogen), cells were resuspended at $1x10^6$ cells/mL in 1x PBS in the presence of 10 µM Cell Tracker™ Blue (CTB). Cells were incubated, protected from light, at 37 °C for 30 min, then washed and resuspended at $1x10^6$ cells/mL in supplemented RPMI.

3.2.7 Flow cytometry

Cells were resuspended at 0.5 $x10^6$ cells/mL in 10 µg/mL anti-CD16/32 blocking antibody and incubated at 4 °C for 20 minutes. Antibody cocktail was added, and the cells were incubated for a further 30 minutes at 4 °C. Cells were then washed and resuspended at 0.5 $x10^6$ cells/mL and mixed with 5 µg/mL 7-AAD (AAT Bioquest). To stain bulk splenocytes, the antibody cocktail was comprised of antibodies for CD3, CD4, CD11c, and B220 in 1x PBS with 2% v/v FBS. Details on antibody reagents are provided in Table 3.1. All flow cytometry data was collected on a Guava

12HT EasyCyte Cytometer (EMD Millipore, USA) using a 405 nm laser and 450/45 nm emission filter and analyzed using FCS Express 6.

Table 3.1: Flow cytometry antibody product information.

Target	*Fluorophore*	*Target Species*	*Clone*	*Vendor*
CD3	AlexaFluor488	Mouse	17A2	Biolegend
CD4	APC/Cy7	Mouse	GK1.5	Biolegend
CD11c	PE	Mouse	N418	Biolegend
B220	AlexaFluor647	Mouse	RA3-6B2	Biolegend
B220	FITC	Mouse	RA3-B2	Biolegend
CD80	PE	Mouse	16-10A1	Biolegend
CD40	AlexaFluor647	Mouse	HM40-3	Biolegend

3.2.8 B cell activation in vitro

Isolated B cells were labeled with 5 µM CFSE (carboxyfluorescein diacetate succinimidyl ester, BD Biosciences) for 30 minutes at 37 °C, rinsed, and resuspended in supplemented RPMI media. B cells were phenotyped by flow cytometry as above, using anti-B220 (FITC). The cells were cultured at $1x10^6$ cells/mL for 48 hours with 0.2 µg/mL of IL-4 (Pepro Tech) and 10 µg/mL R848 (Invivogen) or with PBS control. Afterwards, the cells were removed from the plate and stained for flow cytometry as described above, using CD40 and CD80.

3.2.9 Ex vivo overlays

Murine lymph nodes were collected and sliced as previously reported.[53–55] Briefly, inguinal, axial and brachial lymph nodes were collected from male and female C57Bl/6 mice, embedded in 6% low melting point agarose (Lonza) and sliced 300-µm thick on a vibratome (Leica VT1000s, USA). Lymph node slices were immunostained with FITC anti-mouse B220 and Lyve-1 as previously reported.[56]

CD3+ T cells were isolated by using a CD3 negative selection kit according to manufacturer instructions (StemCell Technologies, USA) from splenocytes sex-matched to the lymph node slices. T cells ($1x10^6$ cells/mL) in 1x PBS were labelled by incubating with NHS-Rhodamine (1 µg/mL, Thermo Fisher) for 30 minutes at 37 °C. B cells were isolated and labeled

with CFSE as above, mixed with labelled T cells and concentrated to $10x10^6$ cells/mL. The cell mixture was then overlaid onto immunostained lymph node slices for 1 hour at 37 °C. To remove excess cells, slices were incubated for at least 30 minutes in 1x PBS with gentle agitation at regular intervals.

3.2.10 Imaging

Confocal microscopy was performed on a Nikon A1Rsi confocal upright microscope, using a 400 nm laser and 450/50 nm GaAsP detector. Images were captured with a 40x/0.45NA Plan Apo NIR WD objective. Widefield microscopy was performed on a Zeiss AxioZoom upright macroscope, using a Zeiss PlanNeoFluar Z 1x / 0.25 NA FWD 56mm objective, Zeiss Axiocam 506 mono camera, and HXP 200 C illuminator with metal halide lamp (Zeiss Microscopy, Germany). Images were collected with Zeiss filter sets 49 (Ex: 365, Em: 445/50), 38 HE (Ex: 470/40, Em: 525/50), 43 HE (Ex: 550/25, Em: 605/70), and 50 (Ex: 640/30, Em: 690/50). Image analysis was completed using ImageJ software 1.48v.[57]

3.3 RESULTS AND DISCUSSION

3.3.1 Synthesis of polymeric boron-based dyes

In order to generate polymeric nanoparticles with different surface chemistries, we synthesized an array of polymers based on the blue-emitting boron-based dye BF_2dbm (**1**-**5** in Table 3.2, Figure 3.1a).[51] We have previously shown that for BF_2dbmPLA, a molecular weight of ~10 kDa for the PLA corresponded to blue fluorescence,[29] so polymers in this size regime were targeted. The dye was prepared as either a primary alcohol (BF_2dbmOCH_2CH_2OH)[31] or a phenol (BF_2dbmOH),[50] to act as an initiator or a coupler respectively (Figure S1). The initiator BF_2dbmOCH_2CH_2OH was used to grow BF_2dbmPLA (**1**), BF_2dbmPLLA (**2**), and BF_2dbmPCL (**3**) by a solvent-free, tin-catalyzed ring-opening polymerization.[31] The BF_2dbmPCL product was further used as a macroinitiator for the ring-opening polymerization of lactide to prepare a block copolymer, BF_2dbmPCL-PLLA (**4**).[58] Finally, to generate the PEGylated material (**5**), BF_2dbmOH

was coupled to PEG-PLLA via a Mitsunobu reaction.[59] The polymer molecular weights and polydispersities were determined by GPC and ^{1}H NMR spectroscopy (Table 3.2). The polydispersities were relatively low (Đ < 1.3) for all five samples, indicating the polymer chains were relatively uniform in chain length.

Table 3.2: Polymer synthesis data. Data collected by M.Zhuang

Polymer	#	*Loading*[a]	M_n[b] *(GPC)*	M_w[b] *(GPC)*	M_n[c] *(NMR)*	*Đ*[b]
BF_2dbmPLA	**1**	1/100	12 300	13 000	15 200	1.06
BF_2dbmPLLA	**2**	1/100	12 200	14 800	13 200	1.24
BF_2dbmPCL	**3**	1/130	6 900	7 300	10 400	1.06
BF_2dbmPCL-PLLA	**4**	1/100	7 700	9 000	14 100	1.17
BF_2dbmPLLA-PEG	**5**	1/130	10 500	11 000	14 400	1.05

[a]Initiator to lactide loading in the ring opening polymerization. For **1**-**3**, BF_2dbmOCH_2CH_2OH was used as the initiator. For BF_2dbmPCL-PLLA (**4**), BF_2dbmPCL (**3**) was used as the initiator. For **5**, PEG-OH (2 kDa) was used as the initiator and the dye (BF_2dbmOH) was added post polymerization. See Schemes S1 and S2 for reference. [b]Average molecular weight (M_n, Da) and weighted molecular weight (M_w, Da) of dye-polymer conjugates determined by gel permeation chromatography (GPC) in THF. Đ = polydispersity index (M_w/M_n). [c]Molecular weight determined by ^{1}H NMR (PLA-H or PCL-CH_2 vs 4-Ar-H of the dye).

3.3.2 Generation of blue fluorescent nanoparticles

Next, boron nanoparticles were fabricated by nanoprecipitation.[11] The polymer was dissolved in a water miscible solvent (DMF), which was added dropwise to DI water. Dialysis against water removed the organic solvent to yield the nanoparticles. Nanoparticle sizes (hydrodynamic radius; R_H) ranged from 37-61 nm (

Table 3.3), in the range suitable for cellular uptake.[60,61] All of the nanoparticles have narrow size distributions with low polydispersity values (0.1 ~ 0.3) and negative zeta potentials.[11] As expected, all five fluorescence spectra were similar with only subtle differences

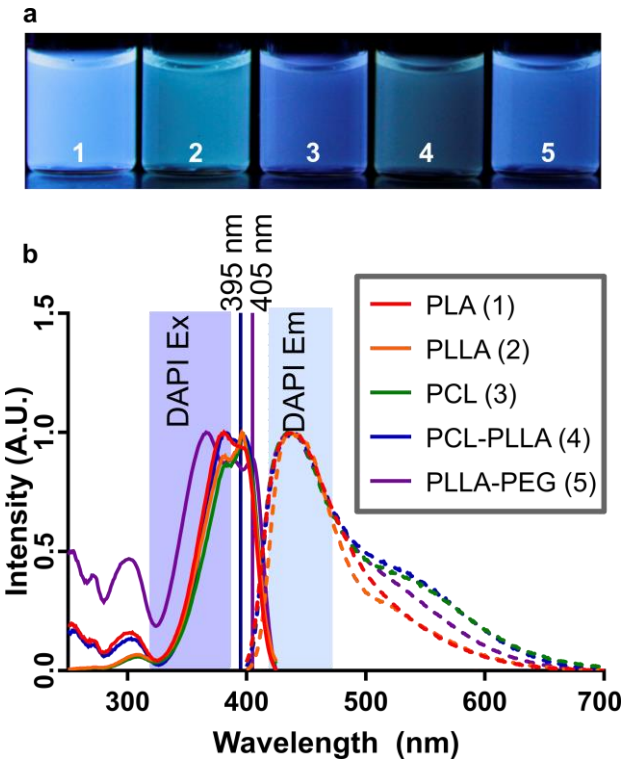

Figure 3.2 Optical properties of boron dye nanoparticles. a) Image of nanoparticles under UV illumination (λ_{ex} = 369 nm). All fluoresced blue. Numbering corresponds to the compounds in Table 3.1. (b) Total excitation (solid lines) and emission spectra (dashed lines) of nanoparticle suspensions (λ_{ex} = 369 nm). Popular excitation sources including a DAPI filter set, 395 nm LED, and 405 nm laser all demonstrate good overlap with the spectra of the nanoparticles. Data collected by M. Zhuang

in spectral features, with excitation in the UV range (366-397 nm) and blue emission (438-447 nm) (Figure 3.2, Table 3.3). For convenience, here and throughout this paper we refer to the nanoparticles formed from the dye-polymer conjugates simply by the name of the polymer. The second, low energy feature observed in the total emission spectra for PCL and PCL-PLLA is commonly observed for PCL-containing samples. This may be due to non-linear, long-range, dye-dye interactions, related to molar mass and matrix effects on the BF_2dbm-fluorophore, as previously described.[62] These spectra make the dyes well suited for use on traditional DAPI filter sets, as well as for excitation via a UV or 405 nm laser by flow cytometry or confocal microscopy.

Table 3.3: Nanoparticle characterization data. Collected by M. Zhuang

Nanoparticles	λ_{max}[a] *(nm)*	ε_{λ}[a] *($M^{-1}cm^{-1}$)*	*Diameter*[b] *(nm)*	*PD*[b]	λ_{Ex}[c] *(nm)*	λ_{F}[c] *(nm)*
PLA	398	32 100	61	0.13	381	439
PLLA	382	25 600	31	0.13	396	437
PCL	400	25 200	56	0.26	397	440
PCL-PLLA	399	21 100	51	0.12	381	438
PLLA-PEG	396	29 800	37	0.23	366	439

[a]Absorption maximum, λ_{max}, and corresponding extinction coefficient at λ_{max}, ε_{λ}, for aqueous nanoparticle suspension (~ 50 μg/mL). [b] Determined by dynamic light scattering, for nanoparticles at 200 μg/mL in water. Polydispersity (PD) is the standard deviation of the distribution. PD = (peak width/peak height)^2. [c]Fluorescence excitation and emission maximum for aqueous nanoparticle suspension.

3.3.3 Physical and optical stability of nanoparticles

We assessed the physical and optical stability of the nanoparticles in aqueous environments suitable for bioimaging, at physiological temperature of 37 °C (Figure 3.3).[51] PLA nanoparticles show good shelf life with respect to molecular weight, size, absorption, and emission for months when stored at 4 °C in water.[11] At elevated temperature, all nanoparticles showed constant size in DI water over one week (Figure 3.3a). In PBS, however, nanoparticles containing PLA or PLLA polymers aggregated immediately, and the block copolymer PCL-PLLA aggregated after two days of incubation (Figure 3.3b). As an alternative to saline, we tested a solution of 5 % glucose in water, intended to match the osmotic pressure of the cells; 2 % serum was added to improve cell handling (water/glucose/serum solution). Compared with PBS, this solution greatly increased the stability of nanoparticles: PLA and PCL were stable for two days, and the other three particles maintained their sizes for over one week (Figure 3.3c). Surprisingly, complete cell culture media, RPMI supplemented with 10 % serum and nutrients (see Methods), better maintained nanoparticle sizes despite its high ionic strength, perhaps because of spontaneous protein coating that protected the nanoparticles against aggregation (Figure 3.3d). The minor fluctuation in radii observed in complete media, known as swelling and deswelling, could be caused by a concentration gradient of ions (e.g., Na^+, Cl^-, amino acids) between the nanoparticle matrix and the surroundings, leading to ion diffusion and osmosis.[63,64] Regardless, nanoparticle radii were maintained consistently.

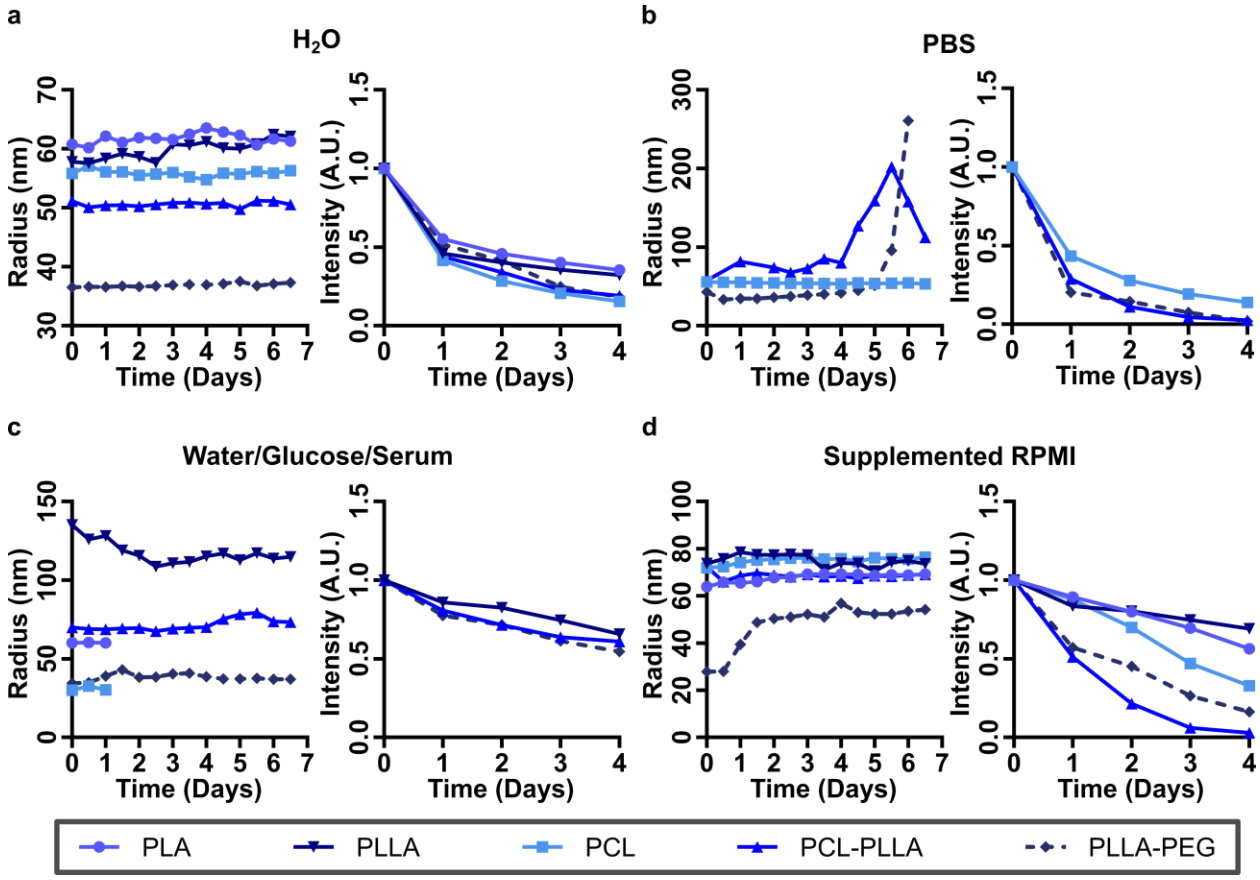

Figure 3.3: Nanoparticle stability at 37 °C in various media. 200 µg/mL of nanoparticles were monitored for size by DLS (left) and emission by fluorimeter (right) in a variety of media. Data not shown for aggregated particles. Data collected by M. Zhuang.

Despite their relative stability in terms of size, the fluorescence intensity of all particle types decreased significantly over time in all solvents at 37 °C, and the rate of decay was sensitive to the choice of solvent (Figure 3.3). Compared to other particles, PLA and PLLA particles retained the most fluorescence intensity over time, and compared to other buffers, they were the most stable in glucose/serum solution and in complete RMPI culture media (Figure 3.3). In terms of "color," the peak emission wavelength was stable for PLA and PLLA particles,[51] and was blue-shifted by no more than 15 nm for PCL and PCL-PLLA nanoparticles.[51]

We hypothesized that the observed decay in fluorescence intensity was due to either hydrolysis of the polyester or degradation of the boron dye. Therefore, we tested polymer and fluorophore stability of the PLA and PCL nanoparticles after storage in water for 5 days at 37 °C.

GPC elution peaks for PLA and PCL nanoparticles were nearly identical before and after incubation,[51] and polydispersity index remained low (1.10), indicating little fluctuation in polymer molecular weight and therefore no evidence of polymer hydrolysis. Based on ^{1}H NMR spectra, the fluorophore in the PLA particle remained unchanged. In the PCL sample, resonances appeared at 6.76 ppm and 16.94 ppm after incubation, which are characteristic of the ArC(O)C***H***=C(OH)Ar proton and associated enol proton ArC(O)CH=C(O***H***) in boron-free dbmPCL, respectively. These results indicate chemical and optical stability for BF_2dbmPLA, but hydrolysis of BF_2 from the dbm binding site of PCL.[11] In the latter case, dye hydrolysis and the resulting reduction in dye concentration is expected to result in a blue-shifted emission,[29,32] consistent with our experimental results for the PCL nanoparticle. In summary, the physical and optical data suggested that nanoparticle stability in solution varies with the polymer chain and surrounding media. While it is not clear to what extent these results will predict the stability once internalized by a cell, we note that for short-term (hours) cellular imaging, boron nanoparticles have been widely and successfully used in many contexts. Longer-term stability in solution may be possible with additional polymer engineering.

3.3.4 Nanoparticle labelling of primary immune cells

With a good understanding of the particle chemistry and stability in solution, we next quantified the uptake of the nanoparticles by live cells. We excluded the racemic PLA particles from these studies, as they offered surface chemistry similar to PLLA but were less physically stable in solution. Primary murine splenocytes were incubated with each remaining type of nanoparticle, washed, and analyzed by flow cytometry (405 nm laser) immediately (day 0) or after 24 hr culture (day 1). For comparison, cells were labelled with Cell Tracker Blue (CTB), a commercially available, coumarin-derived, small molecule reagent that diffuses passively into the cell and binds covalently with thiol groups in the cytoplasm. Mixed splenocytes incubated with CTB were labelled with high efficiency, while a lower percentage of cells incubated with

nanoparticles were labelled, indicating a more selective labelling mechanism (Figure 3.4a). PCL and PCL-PLLA nanoparticles each labelled ~ 50% of the mixed splenocyte culture, while PLLA nanoparticles labelled only 25% on average. Cellular phenotyping showed that the nanoparticles labelled CD11c-positive and B220-positive cells more efficiently than CD3-positive T cells (Figure 3.4b). This result suggests that the nanoparticles may label the cells through an active uptake mechanism, as both B cells and CD11c+ cells can act as antigen presenting cells and are more endocytic than T cells.[65] Indeed, the increased uptake of the hydrophobic PCL-containing particles compared to PLLA particles is consistent with improved internalization of more hydrophobic polymers[45] PEGylated nanoparticles (PLLA-PEG) labelled very few cells, consistent with PEG preventing binding and cellular internalization of nanoparticles.[49] Future work will explore the active uptake mechanism as a possible point of control; enabling the targeting of nanoparticles to different cellular subsets.

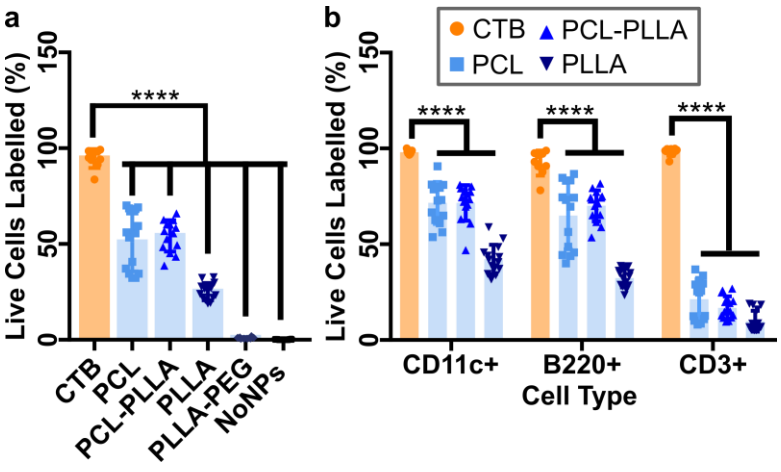

Figure 3.4: Fabricated nanoparticles labelled primary immune cells. (a) Mixed primary splenocytes were labelled with Cell Tracker Blue (CTB), boron-based polymer nanoparticles, or no label. Uptake was measured immediately by flow cytometry. One-way ANOVA with comparisons of each group to CTB control. (b) Uptake of selected NPs by cell type as determined by flow cytometry. More phagocytic cell types were more readily labelled by nanoparticles. Each dot represents one biological replicate. Two-way ANOVA with multiple comparisons. ****p<0.0001.

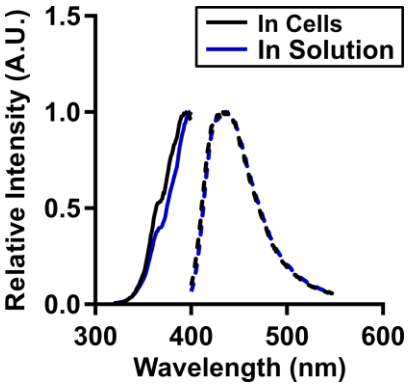

Figure 3.5: BNP spectra were unchanged after labelling cells. Excitation (solid) and emission (dashed) scans of PCL-PLLA nanoparticles immediately after labelling mixed splenocytes (black) and suspended in water (blue). Traces are averaged over three replicates and background subtracted.

Next, we tested the stability of cellular labelling. The fluorescence excitation and emission spectra immediately after cellular uptake (i.e. after 30 min incubation) were comparable to nanoparticles in solution (Figure 3.5). Labelled cells were also monitored after 24 hours. Cell Tracker Blue, like other cytoplasmic dyes, often suffers from a significant decrease in fluorescence intensity after the first 24 hours as unbound dye diffuses out of the cell. Indeed, we observed that the average CTB intensity per cell dropped by two-fold overnight, while there was no decrease in the percentage of CTB-labelled cells (Figure 3.6). Interestingly the nanoparticle labelled cells showed an opposite effect. The percentage of cells that were labelled with nanoparticles decreased to 75%, on average, of its initial value after overnight culture, while the mean intensity per labelled cell did not (Figure 3.6). These data suggest that the nanoparticles may be exported by a fraction of the cells. The relative stability of nanoparticle intensity per cell during this time frame compared to CTB labelled populations may be a point of control when transitioning this technology for long-term tracking.

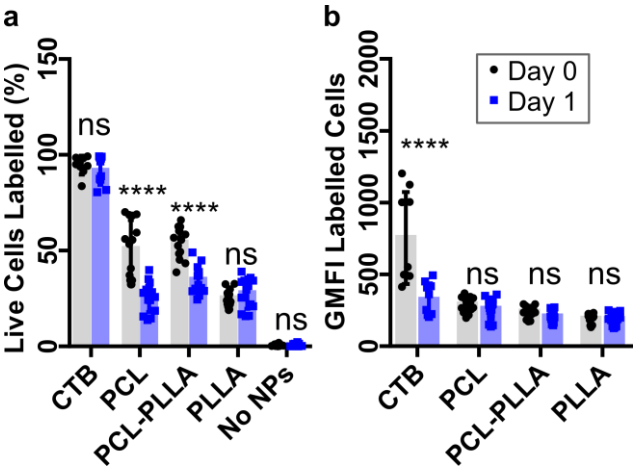

Figure 3.6: NP labelling persisted over 24 hours. Stability of cellular labelling in mixed splenocytes after overnight culture as measured by flow cytometry both in terms of fraction of cells labelled (a) and intensity (b). Each dot represents one biological replicate. Two-way ANOVA with multiple comparisons. ****$p<0.0001$, n.s. denotes $p>0.05$

Finally, we addressed whether labelling with nanoparticles affected cellular viability. Average viability in mixed splenocytes was unchanged by labelling with nanoparticles or CTB, except for a 20% reduction in viability of PLLA-labelled splenocytes after 24 hours of culture (Figure 3.7). Thus, the nanoparticle-labelling process is compatible with maintaining high viability in primary splenocyte cultures. Based on these data, we selected the PCL-PLLA co-block polymer nanoparticles for further testing, based on its stability in solution, high initial labelling efficiency of the cell types of interest, and cytocompatibility.

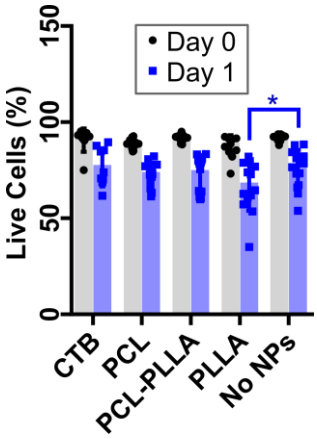

Figure 3.7: NP labelling did not affect 24-hr viability. Viability of labelled and unlabeled cells in mixed splenocytes as determined by flow cytometry after overnight culture. Viability is defined as 7-AAD negative. Each dot represents one biological replicate. Two-way ANOVA with multiple comparisons. *p=0.0148.

3.3.5 Nanoparticle labelling does not affect immune cell function

Having demonstrated that splenocyte viability was not affected by nanoparticle labelling, it was essential to determine whether labelling affected relevant cellular functions. Given their prominent role in adaptive immunity, high frequency in the splenocyte culture, and high rate of staining, we focused on the effect of labelling on B cells in particular. B cells act as “antibody factories,” and upon stimulation proliferate to begin the process of producing the most effective antibody against the pathogen, generating a strong adaptive response. We have shown that labelling with nanoparticles did not affect the viability of B cells in a mixed splenocyte culture (Figure 3.8) and so to test the response to stimulation, we used the small molecule R848, which acts through Toll-like receptor 7 (TLR7) and results in proliferation, antibody production, and up-regulation of

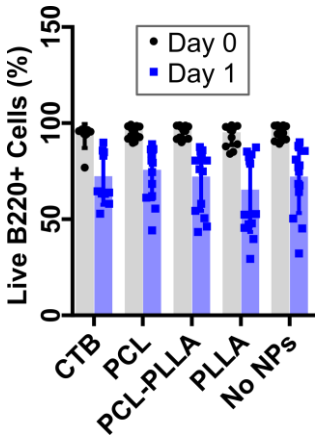

Figure 3.8: NP labelling did not affect B cell viability over 24 hours. Viability of labelled and unlabeled B cells from a mixed splenocyte population as determined by flow cytometry after overnight culture. Viability is defined as 7-AAD negative. Each dot represents one biological replicate.

surface activation markers such as CD40 and CD80.[66] In preliminary tests, R848 elicited a stronger response in unlabeled B cells than other common stimuli at matched doses (Figure 3.9). Upon further optimization we determined that 10 µg/mL was the optimum concentration of R848 to stimulate B cells (Figure 3.10). As with many immune stimulants we observed a bell-curve effect on this scale. At high doses of R848 the B cells had lower viability (not shown) and those that were still present were more similar to the unstimulated control in all metrics (Figure 3.10). This illustrated the importance of titrating every biologically derived reagent.

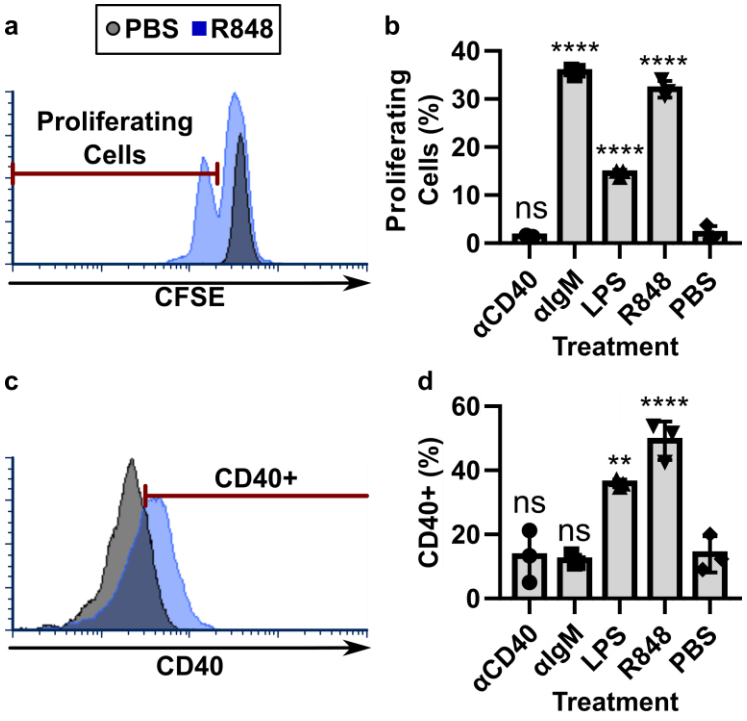

Figure 3.9: R848 elicited the strongest B cell response. (a) Representative CFSE histograms of PBS (black) and R848 (blue) treated B cells. (b) Quantification of proliferating cells. (c) Representative CD40 histograms of PBS and R848 treated B cells. (d) Quantification of CD40+ cells. Each dot represents one biological replicate. One-way ANOVA with comparisons to PBS control. **p=0.0014 ****p<0.0001 n.s. denotes p>0.05.

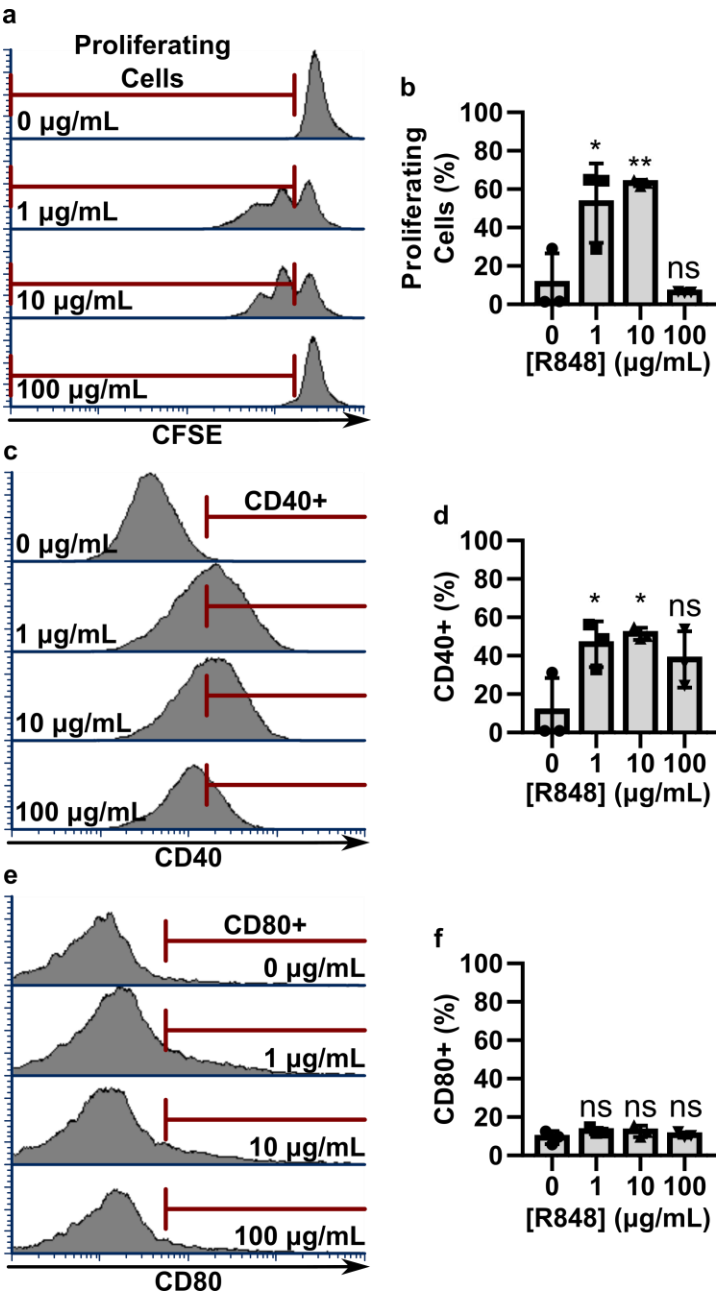

Figure 3.10: Titration of R848 for B cell stimulation. (a) Representative CFSE histograms of indicated R848 concentrations. (b) Quantification of proliferating live B cells. (c) Representative CD40 histograms. (d) Quantification of CD40+ live B cells. (e) Representative CD80 histograms. (f) Quantification of CD80+ live B cells. Each dot represents one biological replicate. One-way ANOVA with comparisons to 0 µg/mL condition. *p<0.03, **p=0.0029, n.s. denotes p>0.05.

Purified B cell populations were labelled with either CTB or the PCL-PLLA nanoparticle and stimulated with R848. Proliferation was tracked by CFSE staining, the brightness of which is reduced with each cycle of cellular proliferation. In the absence of R848 stimulation, nanoparticle labelling did not induce B cell proliferation (Figure 3.11) or activation marker expression (Figure 3.12), indicating that the particles did not activate the cells on their own. After 48-hr R848

treatment, neither the Cell Tracker Blue nor the nanoparticles suppressed the proliferation and upregulation of activation markers on purified B cells (Figure 3.11, Figure 3.12).

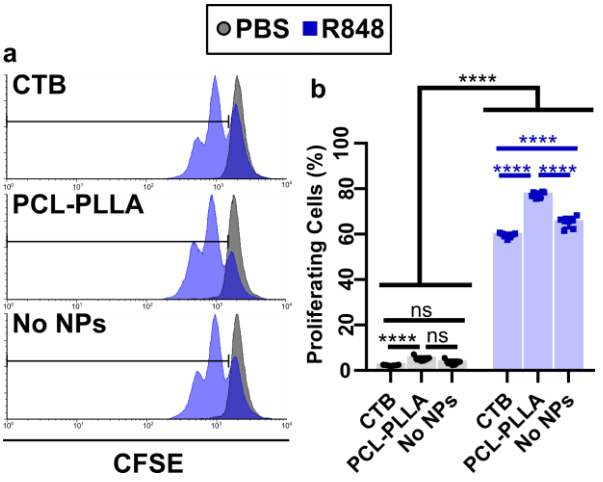

Figure 3.11: NP labelling did not affect B cell proliferation after stimulation. (a) Representative histograms of CFSE intensity as measured by flow cytometry. Proliferation was measured as the percentage of cells with reduced CFSE intensity compared to unstimulated cells. (b) Quantification of proliferated cells. Stimulation with R848 resulted in increased proliferation in all labelling schemes. Two-way ANOVA with multiple comparisons. **** p<0.0001, *** p=0.0003, ns denotes p>0.05.

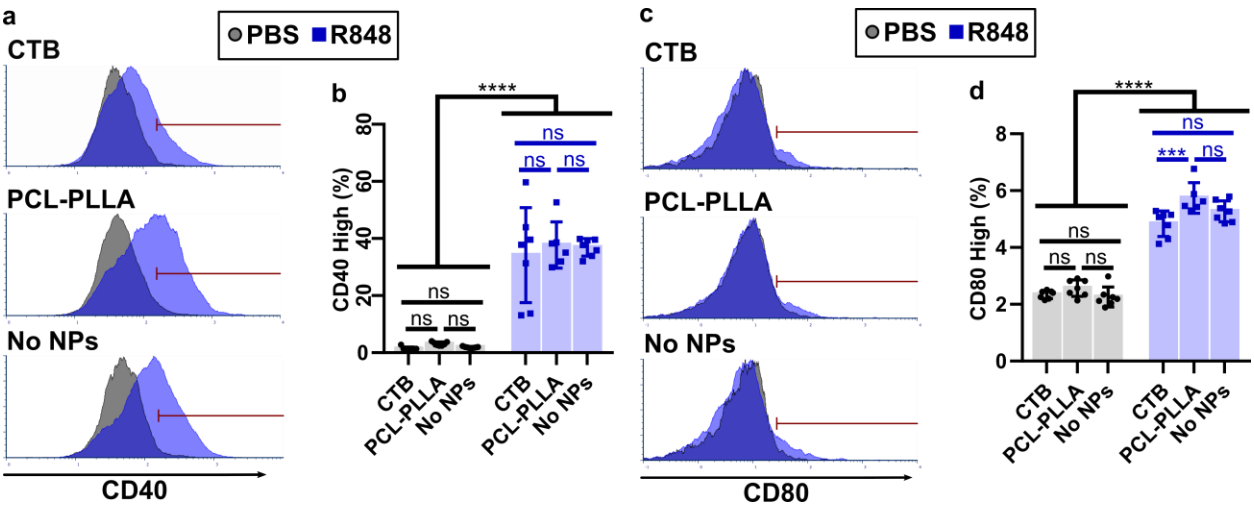

Figure 3.12: Labelling of primary splenocyte B cells did not affect up regulation of activation markers in response to stimulation. (a) Representative histograms of CD40 as measured by flow cytometry (b) Quantification of CD40 high (marker) labeled cells. (c) Representative histograms of CD80 as measured by flow cytometry. (d) Quantification of CD80 high (marker) labelled cells. Stimulation with R848 resulted in higher activation marker percentages in both labelling schemes; though CD80 is a much subtler shift. Two-way ANOVA with multiple comparisons. **** p<0.0001, *** p=0.0003, ns denotes p>0.05.

B cells labelled with PCL-PLLA nanoparticles did proliferate at a higher frequency than the unlabeled cells, but did not exhibit an increase in activation marker expression, indicating that any synergy of the nanoparticle loading with R848 stimulation was modest. In separate experiments, the ability of CD3+ T cells to respond to a non-antigen-specific stimulation was also

uncompromised by nanoparticle labelling (Figure 3.13). Overall, these data show that the labelling of primary splenocytes with PCL-PLLA nanoparticles does not compromise immune function.

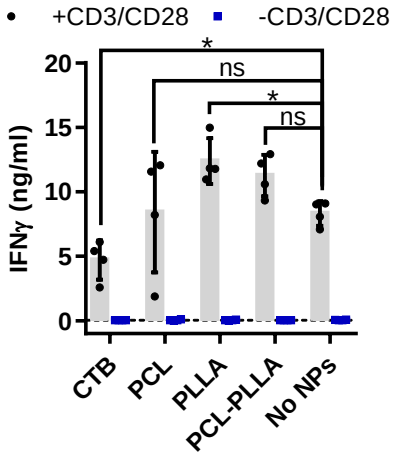

Figure 3.13: T cell activation in bulk splenocytes labelled with nanoparticles. Splenocytes were incubated with anti-CD3/CD28 to induce non-antigen-specific T cell activation. After 24 hours, IFN-γ secretion in the supernatant was analyzed by ELISA. There were significant differences between the stimulated and PBS conditions in all labelling schemes. CTB-labelled cells were significantly lower than the no nanoparticle control whereas the PCL-PLLA-labelled cells were not significant. Dashed line near zero depicts the ELISA limit of detection. Two-way ANOVA with multiple comparisons. * $p < 0.05$.

3.3.6 Nanoparticle labelling is intracellular and bright

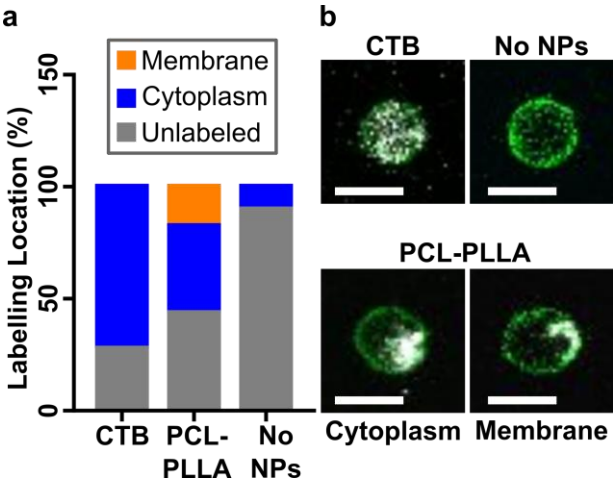

Figure 3.14: Nanoparticle labelling was mainly intracellular. (a) Quantification of staining location as determined by confocal microscopy (400 nm excitation). (b) Representative images of labelling location. Cells were co-labelled with AF488 anti-CD45 antibody (green) to determine membrane location. Brightness and contrast differs between images to account for different excitation efficiencies. Scale bar is 10 µm.

For cell tracking applications, labelling with the nanoparticles must be intracellular, as any extracellular particles or aggregates could easily be washed away during handling. Therefore, we determined the distribution of PCL-PLLA nanoparticles in or on labelled splenocytes via confocal microscopy (400 nm laser excitation). Cell membranes were marked with anti-CD45, a surface-bound pan-lymphocyte marker, to visually determine whether each cell was unlabeled, labelled in the cytoplasm, labelled extracellularly (outer surface of membrane), or labelled on the membrane itself (Figure 3.14). This method of data collection leaves some ambiguity as to whether the “membrane”-associated nanoparticles are in

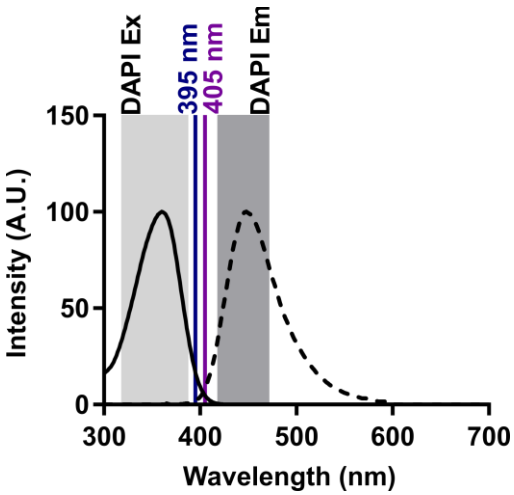

Figure 3.15: CTB did not line up well with 405 nm excitation sources. Excitation (solid) and emission (dashed) data for 7-hydroxy-4-methylcoumarin, overlaid with typical excitation sources and DAPI emission filter. This data is representative of the spectra for Cell Tracker Blue. The dye has very low overlap with 395 nm and 405 nm excitation sources. Spectral data from Thermo Fisher spectra viewer page for 7-hydroxy-4-methylcoumarin.

contact with the inner or outer leaflet of the cell membrane or penetrate entirely. As expected for a cytoplasmic dye, all CTB signal was detected within the bounds of the cell membrane. Nanoparticle labelling was either cytoplasmic or associated with the membrane, and none of the latter cells had signal from the nanoparticles protruding out into the surrounding media. Thus, the majority of the signal from the PCL-PLLA nanoparticles is cytoplasmic and is useful for potentially tracking cells. We noted in this experiment that the CTB-labelled cells appeared dimmer than the nanoparticle labelled cells. This difference in brightness is consistent with the poor overlap between CTB and the 400 nm excitation source (Figure 3.15), though it does contrast with results seen earlier by flow cytometry, likely due to the difference in sensitivity between detectors on the two instruments.

The original goal was to develop a very bright blue labelling system for fluorescence microscopy, as many blue dyes suffer from low quantum yields.[6] Thus, we measured the fluorescence intensity of labelled cells when imaged by widefield microscopy under standard UV excitation (360/60 nm filter). The intensity of cells labelled with PCL-PLLA nanoparticles was 1.43-fold brighter than cells labelled with CTB. In fact, CTB-labelled cells were not significantly brighter than unlabeled cells under these imaging conditions (Figure 3.16a). In this experiment, we did note large aggregates of nanoparticles (arrow head in Figure 3.16b) outside of the cells, which were difficult to remove. We speculate that this aggregation arose from the experimental procedure, in which cells were resuspended in 1x PBS for dual-labelling with Cell Trace Far Red

after labelling with the blue reagent; 1x PBS causes free nanoparticles to aggregate quickly. Further experimentation is needed to determine the best approach to minimize extracellular aggregate formation during cellular manipulation, for example by keeping cells in protein-rich media.

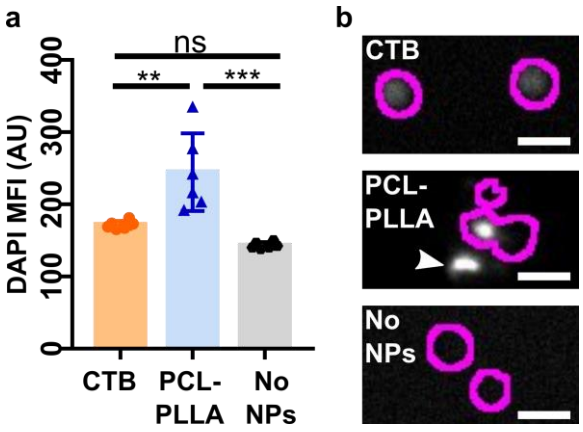

Figure 3.16: NP labelling was brighter than CTB when imaged within cells with 405 nm excitation. (a) Quantification of intensity using widefield microscopy (360 nm excitation) of labelled and unlabeled cells. PCL-PLLA labelled cells were on average 1.43 times brighter than CTB labelled cells. Each dot represents one sample averaged over 200+ cells. Ordinary one-way ANOVA with multiple comparisons. ** p=0.0029, *** p=0.0001, n.s. denotes p>0.05 (d) Representative images of cells labelled with CTB and PCL-PLLA nanoparticles with identical brightness and contrast settings. Cells were co-labelled with Cell Trace Far Red to locate cells efficiently (purple outlines). Large aggregates of PCL-PLLA particles were detected in this labelling scheme (arrowhead). Scale bar is 10 μm.

3.3.7 Nanoparticle labelled cells are brightly visible against tissue autofluorescence

When working with typical blue fluorophores, their low fluorescence intensity is especially challenging to detect against tissue, a complex matrix that exhibits high background.[6] We hypothesized that the bright-blue fluorescent nanoparticles would not suffer from this limitation. We tested the ability to detect nanoparticle-labelled cells embedded in living tissue with widefield microscopy, by labelling purified B cells and overlaying them onto live slices of murine lymph node as a model system.[56] As in the in vitro imaging above, the PCL-PLLA nanoparticle labelled cells were significantly brighter than both unlabeled and CTB labelled cells (Figure 3.17a) and easily detectable against the autofluorescence of the tissue.

The nanoparticles allowed us to capture bright signal within the blue channel of the widefield fluorescence microscope (360/60 nm excitation), freeing the remaining three channels for additional fluorophores to monitor multiple cell populations and tissue structures. As a proof-of-principle, we labelled purified B cells with the PCL-PLLA nanoparticles, labelled purified T cells with a rhodamine-based cytoplasmic dye (NHS-rhodamine), and overlaid these cells on a slice of lymph node tissue that was live immunostained for B220 (B cell zones) and Lyve-1 (lymphatic vessels) (Figure 3.17b-d).

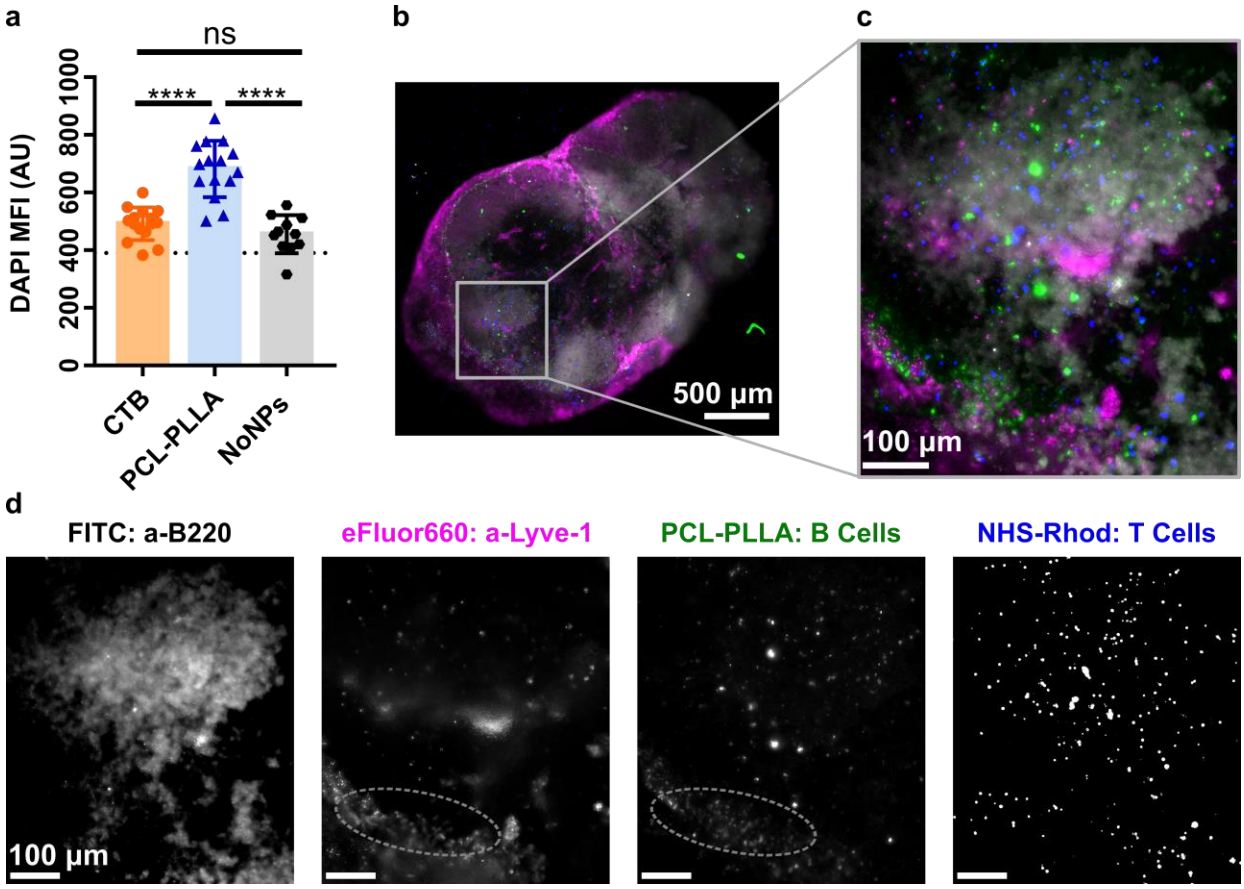

Figure 3.17: Imaging PCL-PLLA labelled cells in tissue. (a) Quantification of labelled cells against tissue background. Nanoparticle labelled cells were significantly brighter after background subtraction compared to both CTB and unlabeled cells. Dotted line represents the average intensity of tissue autofluorescence in the DAPI filter. Two-way ANOVA with multiple comparisons. **** $p<0.0001$, ns $p>0.05$. (b) Image of representative stained tissue slice (3x mag). The live tissue was immunostained with FITC anti-B220 (white), and eFluor660 anti-Lyve-1 (false-colored pink) to show B cell follicles and lymphatics. (c) View of a single B cell follicle within the tissue slice (10x mag). Here we can visualize overlaid B cells labelled with PCL-PLLA nanoparticles (false-colored green) and T cells labelled with NHS-Rhodamine (false-colored blue). (d) Individual channel data from (c). Some nanoparticle aggregates align well with the Lyve-1 signal (dashed ovals).

With this multi-color staining approach, we could visualize individual B cell follicles and the mixture of B cells (green) and T cells (blue) on the tissue. The fluorescent puncta from nanoparticle-labelled cells were smaller than the diameter of the cytoplasmic-labelled cells, since the particles do not fill the entire cytoplasm. Interestingly we also observed a collection of small signals in the nanoparticle channel that aligned with the lymphatic staining (Figure 3.17d, dashed oval).

We speculate that this signal comes from free nanoparticles or aggregates coming into contact with the endocytic cells that line the lymphatic vessels in the lymph node.[67] This limitation should be taken into consideration when translating this technology in the future; it could also be taken advantage of to label endocytic cells in live tissue slices. Overall, we are able to easily visualize all four fluorophores simultaneously by widefield microscopy, using a set of four standard fluorescence filter sets.

3.4 Conclusions and Future Work

This chapter described the fabrication and the characterization of a family of five bright-blue fluorescent boron-based polymeric nanoparticles. The nanoparticles exhibited high excitation and emission efficiency at wavelengths that match well with a variety of traditional sources for microscopy and flow cytometry, including a 405 nm laser, 395 nm LED and 360/60 nm excitation filter. Nanoparticle stability at 37 °C was best maintained in supplemented RPMI media and an isotonic glucose solution without saline. Primary splenocytes, particularly the phagocytic cell types, were well labelled by these particles and remained brightly fluorescent overnight with no detectable impact on viability or ability to respond to stimulation. PCL-PLLA co-block polymer-based nanoparticles had the highest labelling efficiency and cellular retention over time. Nanoparticle labelling was cytoplasmic and is significantly brighter than cells labelled with Cell Tracker Blue, a commercially available cytoplasmic blue dye, when imaged by both confocal and widefield microscopy. Cells labelled with PCL-PLLA were easily distinguished against tissue autofluorescence, which enabled straightforward four-color imaging. In the future, we will use this

approach to image B and T cell interactions within ex vivo lymph node samples and map where these interactions occur.

Broadly, these bright blue fluorescent nanoparticles expand the toolbox for cellular labelling and tracking in multi-color imaging experiments and may find many applications in a variety of tissues. Potential future improvements include varying the surface chemistry of the nanoparticles to enhance uptake by non-phagocytic cells, and adding functional groups such as succinimidyl esters or maleimides to increase dye retention within the cells.

3.5 REFERENCES

1 Ahrens ET, Flores R, Xu H, Morel PA. In vivo imaging platform for tracking immunotherapeutic cells. *Nat Biotechnol* 2005; **23**: 983–987.

2 Schaefer BC, Schaefer ML, Kappler JW, Marrack P, Kedl RM. Observation of antigen-dependent CD8+ T-cell/ dendritic cell interactions in vivo. *Cell Immunol* 2001; **214**: 110–122.

3 Prendergast RA, Iliff CE, Coskuncan NM, Caspi RR, Sartani G, Tarrant TK *et al.* T cell traffic and the inflammatory response in experimental autoimmune uveoretinitis. *Invest Ophthalmol Vis Sci* 1998; **39**: 754–762.

4 Parish CR. Fluorescent dyes for lymphocyte migration and proliferation studies. *Immunol Cell Biol* 1999; **77**: 499–508.

5 Atale N, Gupta S, Yadav UCS, Rani V. Cell-death assessment by fluorescent and nonfluorescent cytosolic and nuclear staining techniques. *J Microsc* 2014; **255**: 7–19.

6 Gonçalves MST. Optimized UV/visible fluorescent markers. In: Demchenko AP (ed). *Advanced Fluorescence Reporters in Chemistry and Biology I: Fundamentals and Molecular Design*. Springer Berlin Heidelberg: Berlin, Heidelberg, 2010, pp 27–64.

7 Karpenko IA, Niko Y, Yakubovskyi VP, Gerasov AO, Bonnet D, Kovtun YP *et al.* Push-pull dioxaborine as fluorescent molecular rotor: Far-red fluorogenic probe for ligand-receptor interactions. *J Mater Chem C* 2016; **4**: 3002–3009.

8 Xiao H, Li P, Zhang W, Tang B. An ultrasensitive near-infrared ratiometric fluorescent probe for imaging mitochondrial polarity in live cells and in vivo. *Chem Sci* 2016; **7**: 1588–1593.

9 Lehner P, Staudinger C, Borisov SM, Klimant I. Ultra-sensitive optical oxygen sensors for characterization of nearly anoxic systems. *Nat Commun* 2014; **5**: 4460.

10 Lavis LD, Raines RT. Bright building blocks for chemical biology. *ACS Chem Biol* 2014; **9**: 855–866.

11 Pfister A, Zhang G, Zareno J, Horwitz AF, Fraser CL. Boron polylactide nanoparticles exhibiting fluorescence and phosphorescence in aqueous medium. *ACS Nano* 2008; **2**: 1252–1258.

12 Kersey FR, Zhang G, Palmer GM, Dewhirst MW, Fraser CL. Stereocomplexed poly(lactic acid)−poly(ethylene glycol) nanoparticles with dual-emissive boron dyes for tumor accumulation. *ACS Nano* 2010; **4**: 4989–4996.

13 DeRosa CA, Fraser CL. *Main group strategies towards functional organic materials*. First edition. John Wiley & Sons: Hoboken, NJ, 2018.

14 Kerr C, DeRosa CA, Daly ML, Zhang H, Palmer GM, Fraser CL. Luminescent difluoroboron β-diketonate PLA–PEG nanoparticle. *Biomacromolecules* 2017; **18**: 551–561.

15 Zhang G, Palmer GM, Dewhirst MW, Fraser CL. A dual-emissive-materials design concept enables tumour hypoxia imaging. *Nat Mater* 2009; **8**: 747–751.

16 DeRosa CA, Seaman SA, Mathew AS, Gorick CM, Fan Z, Demas JN *et al.* Oxygen sensing difluoroboron β-diketonate polylactide materials with tunable dynamic ranges for wound imaging. *ACS Sens* 2016; **1**: 1366–1373.

17 Samonina-Kosicka J, DeRosa CA, Morris WA, Fan Z, Fraser CL. Dual-emissive difluoroboron naphthyl-phenyl β-diketonate polylactide materials: Effects of heavy atom placement and polymer molecular weight. *Macromolecules* 2014; **47**: 3736–3746.

18 Samonina-Kosicka J, Weitzel DH, Hofmann CL, Hendargo H, Hanna G, Dewhirst MW *et al.* Luminescent difluoroboron β-diketonate PEG-PLA oxygen nanosensors for tumor imaging. *Macromol Rapid Commun* 2015; **36**: 694–699.

19 Zhao D, Li G, Wu D, Qin X, Neuhaus P, Cheng Y *et al.* Regiospecific N-heteroarylation of amidines for full-color-tunable boron difluoride dyes with mechanochromic luminescence. *Angew Chem Int Ed* 2013; **52**: 13676–13680.

20 Cogné-Laage E, Allemand JF, Ruel O, Baudin JB, Croquette V, Blanchard-Desce M *et al.* Diaroyl(methanato)boron difluoride compounds as medium-sensitive two-photon fluorescent probes. *Chem - Eur J* 2004; **10**: 1445–1455.

21 Butler T, Morris WA, Samonina-Kosicka J, Fraser CL. Mechanochromic luminescence and aggregation induced emission of dinaphthoylmethane β-diketones and their boronated counterparts. *ACS Appl Mater Interfaces* 2016; **8**: 1242–1251.

22 Mukherjee S, Thilagar P. Stimuli and shape responsive 'boron-containing' luminescent organic materials. *J Mater Chem C* 2016; **4**: 2647–2662.

23 Xu S, Evans RE, Liu T, Zhang G, Demas JN, Trindle CO *et al.* Aromatic difluoroboron β-diketonate complexes: effects of π-conjugation and media on optical properties. *Inorg Chem* 2013; **52**: 3597–3610.

24 Larsen TA, Goodsell DS, Cascio D, Grzeskowiak K, Dickerson RE. The structure of DAPI bound to DNA. *J Biomol Struct Dyn* 1989; **7**: 477–491.

25 Karpovich DS, Blanchard GJ. Relating the polarity-dependent fluorescence response of pyrene to vibronic coupling. Achieving a fundamental understanding of the py polarity scale. *J Phys Chem* 1995; **99**: 3951–3958.

26 Lavis LD, Raines RT. Bright ideas for chemical biology. *ACS Chem Biol* 2008; **3**: 142–155.

27 Reisch A, Klymchenko AS. Fluorescent polymer nanoparticles based on dyes: Seeking brighter tools for bioimaging. *Small* 2016; **12**: 1968–1992.

28 Zhang G, St. Clair TL, Fraser CL. Synthesis and fluorescent properties of difluoroboron dibenzoylmethane polycaprolactone. *Macromolecules* 2009; **42**: 3092–3097.

29 Zhang G, Kooi SE, Demas JN, Fraser CL. Emission color tuning with polymer molecular weight for difluoroboron dibenzoylmethane-polylactide. *Adv Mater* 2008; **20**: 2099–2104.

30 Corbin PS, Webb MP, McAlvin JE, Fraser CL. Biocompatible polyester macroligands: New subunits for the assembly of star-shaped polymers with luminescent and cleavable metal cores. *Biomacromolecules* 2001; **2**: 223–232.

31 Zhang G, Chen J, Payne SJ, Kooi SE, Demas JN, Fraser CL. Multi-emissive difluoroboron dibenzoylmethane polylactide exhibiting intense fluorescence and oxygen-sensitive room-temperature phosphorescence. *J Am Chem Soc* 2007; **129**: 8942–8943.

32 Contreras J, Xie J, Chen YJ, Pei H, Zhang G, Fraser CL *et al.* Intracellular uptake and trafficking of difluoroboron dibenzoylmethane−polylactide nanoparticles in HeLa cells. *ACS Nano* 2010; **4**: 2735–2747.

33 Reeve MS, McCarthy SP, Downey MJ, Gross RA. Polylactide stereochemistry: effect on enzymic degradability. *Macromolecules* 1994; **27**: 825–831.

34 Ishii D, Ying TH, Mahara A, Murakami S, Yamaoka T, Lee W *et al.* In vivo tissue response and degradation behavior of PLLA and stereocomplexed PLA nanofibers. *Biomacromolecules* 2009; **10**: 237–242.

35 Woodard LN, Grunlan MA. Hydrolytic degradation and erosion of polyester biomaterials. *ACS Macro Lett* 2018; **7**: 976–982.

36 Pitt CG, Chasalow FI, Hibionada YM, Klimas DM, Schindler A. Aliphatic polyesters. I. The degradation of poly (ε-caprolactone) in vivo. *J Appl Polym Sci* 1981; **26**: 3779–3787.

37 Sinha VR, Bansal K, Kaushik R, Kumria R, Trehan A. Poly-ϵ-caprolactone microspheres and nanospheres: an overview. *Int J Pharm* 2004; **278**: 1–23.

38 Dash TK, Konkimalla VB. Poly-e-caprolactone based formulations for drug delivery and tissue engineering: A review. J. Controlled Release. 2012; **158**: 15–33.

39 Du J, Zhang YS, Hobson D, Hydbring P. Nanoparticles for immune system targeting. *Drug Discov Today* 2017; **22**: 1295–1301.

40 Zolnik BS, González-Fernández Á, Sadrieh N, Dobrovolskaia MA. Nanoparticles and the immune system. *Endocrinology* 2010; **151**: 458–465.

41 Jiang W, Kim BYS, Rutka JT, Chan WCW. Nanoparticle-mediated cellular response is size-dependent. *Nat Nanotechnol* 2008; **3**: 145–150.

42 Reddy ST, Rehor A, Schmoekel HG, Hubbell JA, Swartz MA. In vivo targeting of dendritic cells in lymph nodes with poly(propylene sulfide) nanoparticles. *J Controlled Release* 2006; **112**: 26–34.

43 Scholzen A, Minigo G, David C, Apostolopoulos V, Mottram PL. Pathogen recognition and development of particulate vaccines: Does size matter? *Methods* 2006; **40**: 1–9.

44 Foged C, Brodin B, Frokjaer S, Sundblad A. Particle size and surface charge affect particle uptake by human dendritic cells in an in vitro model. *Int J Pharm* 2005; **298**: 315–322.

45 Sitia L, Ferrari R, Violatto MB, Talamini L, Dragoni L, Colombo C *et al.* Fate of PLA and PCL-based polymeric nanocarriers in cellular and animal models of triple-negative breast cancer. *Biomacromolecules* 2016; **17**: 744–755.

46 Suk JS, Xu Q, Kim N, Hanes J, Ensign LM. PEGylation as a strategy for improving nanoparticle-based drug and gene delivery. *Adv Drug Deliv Rev* 2016; **99**: 28–51.

47 Bruckman MA, Randolph LN, VanMeter A, Hern S, Shoffstall AJ, Taurog RE *et al.* Biodistribution, pharmacokinetics, and blood compatibility of native and PEGylated tobacco mosaic virus nano-rods and -spheres in mice. *Virology* 2014; **449**: 163–173.

48 Yu SS, Lau CM, Thomas SN, Gray Jerome W, Maron DJ, Dickerson JH *et al.* Size- and charge-dependent non-specific uptake of PEGylated nanoparticles by macrophages. *Int J Nanomedicine* 2012; **7**: 799–813.

49 Jokerst JV, Lobovkina T, Zare RN, Gambhir SS. Nanoparticle PEGylation for imaging and therapy. *Nanomed* 2011; **6**: 715–728.

50 Cammack JK, Marder SR, Kippelen B. U.S. Patent 6 916 894, 2005

51 Belanger MC, Zhuang M, Ball AG, Richey KH, DeRosa CA, Fraser CL *et al.* Labelling primary immune cells using bright blue fluorescent nanoparticles. *Biomater Sci* 2020; : 1897–1909.

52 Fessi H, Puisieux F, Devissaguet JPh, Ammoury N, Benita S. Nanocapsule formation by interfacial polymer deposition following solvent displacement. *Int J Pharm* 1989; **55**: R1–R4.

53 Ross AE, Belanger MC, Woodroof JF, Pompano RR. Spatially resolved microfluidic stimulation of lymphoid tissue ex vivo. *The Analyst* 2017; **142**: 649–659.

54 Ross AE, Pompano RR. Diffusion of cytokines in live lymph node tissue using microfluidic integrated optical imaging. *Anal Chim Acta* 2018; **1000**: 205–213.

55 Catterton MA, Dunn AF, Pompano RR. User-defined local stimulation of live tissue through a movable microfluidic port. *Lab Chip* 2018; **18**: 2003–2012.

56 Groff BD, Kinman AWL, Woodroof JF, Pompano RR. Immunofluorescence staining of live lymph node tissue slices. *J Immunol Methods* 2019; **464**: 119–125.

57 Schneider CA, Rasband WS, Eliceiri KW. NIH Image to ImageJ: 25 years of image analysis. *Nat Methods* 2012; **9**: 671–675.

58 Zhang G, Fiore GL, St. Clair TL, Fraser CL. Difluoroboron dibenzoylmethane PCL-PLA block copolymers: Matrix effects on room temperature phosphorescence. *Macromolecules* 2009; **42**: 3162–3169.

59 Thévenaz DC, Monnier CA, Balog S, Fiore GL. Luminescent nanoparticles with lanthanide-containing poly(ethylene glycol)–poly(ε-caprolactone) block copolymers. *Biomacromolecules* 2014; **15**: 3994–4001.

60 Petros RA, DeSimone JM. Strategies in the design of nanoparticles for therapeutic applications. *Nat Rev Drug Discov* 2010; **9**: 615–627.

61 Panyam J, Sahoo SK, Prabha S, Bargar T, Labhasetwar V. Fluorescence and electron microscopy probes for cellular and tissue uptake of poly(d,l-lactide-co-glycolide) nanoparticles. *Int J Pharm* 2003; **262**: 1–11.

62 Zhang G, Fiore GL, St. Clair TL, Fraser CL. Difluoroboron dibenzoylmethane PCL-PLA block copolymers: matrix effects on room temperature phosphorescence. *Macromolecules* 2009; **42**: 3162–3169.

63 Proikakis CS, Mamouzelos NJ, Tarantili PA, Andreopoulos AG. Swelling and hydrolytic degradation of poly(d,l-lactic acid) in aqueous solutions. *Polym Degrad Stab* 2006; **91**: 614–619.

64 Horkay F, Tasaki I, Basser PJ. Osmotic swelling of polyacrylate hydrogels in physiological salt solutions. *Biomacromolecules* 2000; **1**: 84–90.

65 Flaherty DK (ed.). Chapter 5 - Antigen-presenting cells. In: *Immunology for Pharmacy*. Mosby: Saint Louis, 2012, pp 37–44.

66 Tomai MA, Imbertson LM, Stanczak TL, Tygrett LT, Waldschmidt TJ. The immune response modifiers imiquimod and R-848 are potent activators of B lymphocytes. *Cell Immunol* 2000; **203**: 55–65.

67 Bellomo A, Gentek R, Bajénoff M, Baratin M. Lymph node macrophages: Scavengers, immune sentinels and trophic effectors. *Cell Immunol* 2018; **330**: 168–174.

4 CHARACTERIZING THE USE OF MAGNETIC BEADS FOR EMBEDDED IMMUNOASSAYS IN LYMPH NODE TISSUE

4.1 INTRODUCTION

Many organs have exquisite organization of sub-structures including the brain,[1] intestine,[2,3] and lymph node.[4] Understanding how the cells within tissue are arranged, and how they communicate is essential to learning more about the biological function. The tissue microenvironment can directly impact cell behavior including stem cell differentiation in the gut,[2,3] and activation of T cells within the lymph node.[5,6] Keeping the tissue organization intact is absolutely necessary to understanding the way in which the location of signals is impacting the biological function. While thin, fixed tissue sections are used regularly for histological studies, they cannot inform on dynamic biological functions.[7,8] Conversely, complex biological reporter systems allow for visualization of specific biological functions but, they are costly to generate.[9–11] Analytical techniques to visualize the molecular organization of tissues without prior manipulation are only recently emerging.

The introduction of *ex vivo* tissue culture has allowed for the manipulation and interrogation of sub-structures within the tissue.[1,12,13] Live tissue slices maintain the spatial organization of the organ, as with *in vivo*, but offer more experimental control. Analyzing specific cells of interest is possible through the use of transient dyes. Cell membrane labelling reveals the state of the cell as it moves through biological processes.[14] The cells of interest are then easily monitored with well-defined fluorescent microscopy techniques. However, secreted signals quickly diffuse away from their source to interact with other cells and require stationary platforms for analysis. Analytical probes, such as electrodes[15,16] or mcirodialysis pumps,[17–19] can be introduced to areas of deep tissue with a high degree of accuracy. These kinds of probes are very informative in the area they are placed, but cannot inform on the state of the tissue as a whole. Arrays of electrodes have been employed to monitor electroactive compounds across a wide area.[20,21] These arrays

can only report on electroactive molecules such as neurotransmitters, protein detection is more difficult. There is a need for a stationary analytical platform that can easily detect secreted protein analytes, within tissue.

Beads have been used as a platform for immunoassays for many years.[22,23] Immunoassays are analytical assays that use antibodies to capture analytes of interest. The most popular platform for bead-based immunoassays is the Luminex system.[24,25] Using beads provides a greater reactive surface area, compared to a traditional well plate, and therefore, a more sensitive assay.[26] Beads are incubated with samples containing the proteins of interest then biotinylated detection antibodies are added to complete the “sandwich” and streptavidin-conjugated phycoerythrin (PE) is used to detect the signal.[27] Two fluorophores in defined ratios act as bar codes to differentiate beads for distinct analytes from one another.[27] In this way, bead platforms are very easily multiplexed. Beads can also be very small; therefore, a large number of beads can be introduced without causing damage to the tissue. This is a risk for the larger probes.[28] We hypothesized that beads could be introduced to *ex vivo* tissue samples with a high degree of precision. The beads, once embedded into the tissue, would then act as a highly sensitive, stationary platform to investigate secreted protein signals.

We chose to investigate the use of beads in lymph node tissue slices as a model system, though they could be employed in any soft tissue setting. The lymph node is a secondary organ of the immune system where the majority of the adaptive immune response is generated and matured.[4] The lymph node is highly organized into distinct areas with specific cell types populating them.[4] As the immune response develops over time cells move throughout the lymph node in response to chemokine gradients within the tissue. The secreted signals from the lymphocytes can change as they move through the tissue and the immune response.[4] Bulk analysis of secreted proteins from the lymphocytes has revealed how secreted signals can change over time[29,30] but

spatial context has not yet been determined in live tissue. By anchoring immunoassays on beads embedded in the tissue we would be able to map gradients of secreted protein signals in response to stimuli. The *ex vivo* slice platform allows for precise dosing of stimulants to the tissue[12,13,29], and in combination with the bead-based immunoassay platform we could generate a complete picture of dose-and-response within the lymph node tissue.

Introducing beads to the immune system poses challenges as lymphocytes are highly phagocytic.[31–33] Particles ranging from 20-200 nm are readily internalized by phagocytic cell types such as macrophages and dendritic cells (DCs).[34] Microparticles that have been introduced as therapeutic agents need to avoid detection from the immune system.[35–37] Therefore, there are a number of established techniques to avoid uptake, including the use of polyethylene glycol (PEG).[38,39] We hypothesized that adding PEG to the beads would prevent uptake of the beads by phagocytic cells.

In this chapter, we functionalized magnetic beads with antibodies. Once the coating was confirmed the distributions of antibody only and antibody and PEG coated beads were characterized within the lymph node tissue.

4.2 Materials and Methods

4.2.1 Functionalizing magnetic beads

To conjugate antibodies and PEG to beads, 100 µg of carboxylic acid functionalized magnetic beads (BangsLab, USA) of indicated sizes was mixed with equal molar proportions of antibody and polyethylene glycol (PEG). Total moles of conjugates were varied based on available binding surface area for size-based characterization.

For all other distribution experiments, beads with a diameter of 1.00 µm were mixed with 0.2 nmols of anti-HRP (BioXCell, USA clone: HRPN, cat: BE0088, 1 mg/mL) and 20 kDa PEG (Thermo Fisher, USA, at 120 mg/mL). The mixture was shaken at room temperature, protected

from light, for 15 minutes. Fresh 10 mg/mL solutions of EDC (Thermo Fisher) were prepared in 1x phosphate buffered saline (PBS) for each reaction. The EDC was added in 1000x molar excess (2 µmol total). The reaction was shaken at 4 °C, protected from light, overnight. To cap any unreacted functional groups 3.5 nmol of 1,8-diaminooctane (Sigma Aldrich, USA) was added to the reaction. This mixture was then shaken at room temperature, protected from light, for an additional 30 minutes. Bead mixtures were washed three times with 1x PBS. The beads were exposed to a strong magnet (StemCell) for 5 minutes each time. The resulting solution was then resuspended in 100 µL, for a final bead concentration of 1 mg/mL.

4.2.2 Making functionalized beads fluorescent

To visualize the beads fluorophores must be added to the functionalized beads. Chromeo494 with NHS functionalization (ActiveMotif, USA) was added to the beads to make them fluorescent. The dye was added in 250 molar excess (50 nmol of dye) to the beads. The reaction was shaken, protected from light, at room temperature for 2 hours. The reactions were washed as above with 1x PBS until the elute was clear and resuspended at 1 mg/mL in 1x PBS for storage. Beads used to characterize delivery to agarose were conjugated with NHS-Rhodamine in the same way instead of Chromeo494.

4.2.3 Secondary antibody assay

In order to confirm that the beads were successfully functionalized secondary antibodies were used. Beads were diluted to 0.1 mg/mL and blocked with 1x PBS supplemented with 10% BSA and 0.05% Tween-20 (components from Thermo Fisher). Beads were blocked for approximately 1 hour at room temperature with agitation and protected from light. The beads were then washed with 1x PBS with 0.05% Tween-20 as before.

Alexa Fluor 647 anti-rat IgG1 (conjugated in-house, described below) was added to the blocked beads in a 1:500 µL dilution. The mixture was reacted at room temperature, with agitation and protected from light for 2 hours. Samples were washed as above and resuspended in 100 µL

of 1x PBS. Samples were then transferred to a black-walled 96 well plate (Corning costar, Thermo Fisher) and both Alexa Fluor 647 and Chromeo494 intensities were measured by plate reader (CLARIOstar; BMG LabTech). Alexa Fluor 647 intensity was normalized to the bead fluorescent intensity to account for differences in bead number between wells.

Alexa Fluor 647 conjugated anti-rat IgG1 (Biolegend, clone: MRG1-58, cat: 407402) was prepared in-house according to manufacturer's procedure with minimal modifications. Briefly, 100 µg of antibody was mixed with 20 molar excess NHS-ester Alexa Fluor 647 (Life Technologies) for 1 hour at room temperature, with agitation and protected from light. The reaction was then filtered through a 50 kDa molecular weight centrifuge filter. The modified antibody was then diluted to 0.2 mg/mL.

4.2.4 Delivery to agarose

Beads of various sizes were delivered to agarose slices to determine appropriate size for further studies. Fluorescent beads were embedded within the agarose slices to facilitate imaging in the correct plane. Liquid 4% low-melting point agarose (Lonza) was mixed with polystyrene beads with FITC embedded within the bead matrix (Polyscience, 2 µm diameter, 0.002% beads). The agarose-bead mixture was then sliced 300 µm thick on a vibratome (Leica VT1000s). Slices were equilibrated in "complete media" for 1 hour at 37 °C and 5% CO_2. Complete media was comprised of: RPMI (Lonza, 16-167F) supplemented with 10 % FBS (VWR, Seradigm USDA approved, 89510-186) 1x L-glutamine (Gibco Life Technologies, 25030-081), 50 U/mL Pen/Strep (Gibco), 50 µM beta-mercaptoethanol (Gibco, 21985-023), 1 mM sodium pyruvate (Hyclone, GE USA), 1x non-essential amino acids (Hyclone, SH30598.01), and 20 mM HEPES (VWR, 97064-362).

The lids of 24-well plates (Falcon, VWR) were covered in Parafilm® to provide a hydrophobic surface and prevent aqueous solutions from wicking away from the slice. Agarose slices with the green beads embedded were placed on the Parafilm® surface with a paint brush. To contain the

solutions of magnetic beads an A2 stainless steel flat washer (10 mm outer diameter, 5.3 mm inner; Grainger, USA) was placed on top of the slice. Functionalized magnetic beads of indicated sizes were then added to the interior of the washer at a concentration of 100 µg/mL. A custom 3D printed holder containing 24 Neodynium magnets (grade N52, 3/8" diameter, 1/8" thickness, J&K Magnetics) arranged with the same x,y coordinates as the 24-well plate was placed underneath the slice set-up. These beads were exposed to the magnet for 20 minutes to allow the majority of the beads to embed within the slice.

Agarose slices were rinsed for 15 minutes in 1x PBS, replacing the 1x PBS every 5 minutes. Images of beads delivered to the slices were collected by an upright stereomicroscope (Zeiss, Germany). Microscope details are described under the "imaging" section.

4.2.5 Delivery to lymph node tissue

Slices of murine lymph node tissue were collected as previously described.[29] Briefly, inguinal, axial and brachial lymph nodes were collected from male and female C57Bl/6 mice, embedded in 6% low melting point agarose (Lonza) and sliced 300-µm thick on a vibratome (Leica VT1000s, USA). Tissue slices were allowed to rest for one hour at 37 °C with 5% CO_2 in complete media.

Tissue slices were then transferred to the same magnetic bead delivery set-up previously described and exposed to the magnet for 5 minutes at room temperature. Slices with beads were then immunostained with Alexa Fluor 488 anti-mouse CD45 (Biolegend, clone: 30-F11, cat: 13122) and eFluor 660 anti-mouse lyve-1 (eBioscience, clone: ALY7 cat: 50-0443-82) as previously described.[14] Stained slices were then washed and fixed in formalin (4% formaldehyde, Protocol, USA) at 4 °C overnight and stored in 1x PBS until imaging by confocal microscopy.

4.2.6 Imaging

Widefield microscopy images were collected with a Zeiss AxioZoom upright macroscope with a PlanNeoFluor Z 1x/0.25 FWD 56mm objective, Axiocam 506 mono camera and HXP 200 C metal halide lamp (Zeiss Microscopy, Germany). Images were collected with Zeiss Filter Sets 38 HE (Ex: 470/40, Em: 525/50), 43 HE (Ex: 550/25, Em: 605/70); 64 HE (Ex: 587/25, Em: 647/70); and 50 (Ex: 640/30, Em: 690/50).

Confocal microscopy was performed on a Nikon A1Rsi confocal upright microscope, using a 487 and 638 nm lasers with 525/50, 600/50 and 685/70 nm GaAsP detectors. Images were collected with a 40x/0.45NA Plan Apo NIR WD objective.

4.2.7 Image and statistical analysis

Image analysis was completed using ImageJ software 1.48v.[40] Bead area was determined using the ”analyze particles” function. Delaunay lengths were calculated using the “Delaunay Voronoi” plug-in.[41] The random distribution of particles was generated using a custom macro written by R. Pompano. The concentration of the random distribution of particles was chosen based on the average number of objects per frame.

All statistical analysis was completed using GraphPad Prism 7 version 7.00.

4.3 RESULTS AND DISCUSSION

4.3.1 Functionalizing magnetic beads

In order for these beads to function as an analytical assay platform they must first be functionalized with a capture antibody. Beads of different sizes, materials, and reactivities are readily commercially available. We chose magnetic polystyrene beads with carboxylic acid reactivity to use as the base for our analytical assay. Delivery of beads by magnets can ensure uniform delivery across the tissue in a relatively short time period. Polystyrene was chosen as the material due to its biocompatibility and the variety of sizes available.[42,43] Carboxylic acid chemistry

is very well defined, which allows for functional features to be added through known chemical processes. Here, we functionalized beads with a model capture antibody, to minimize changes in tissue signaling; PEG was also added to many of the beads to determine its role in bead distribution. We were able to coat carboxylic acid functionalized magnetic beads with a mixture of antibodies and PEG (Figure 4.1).

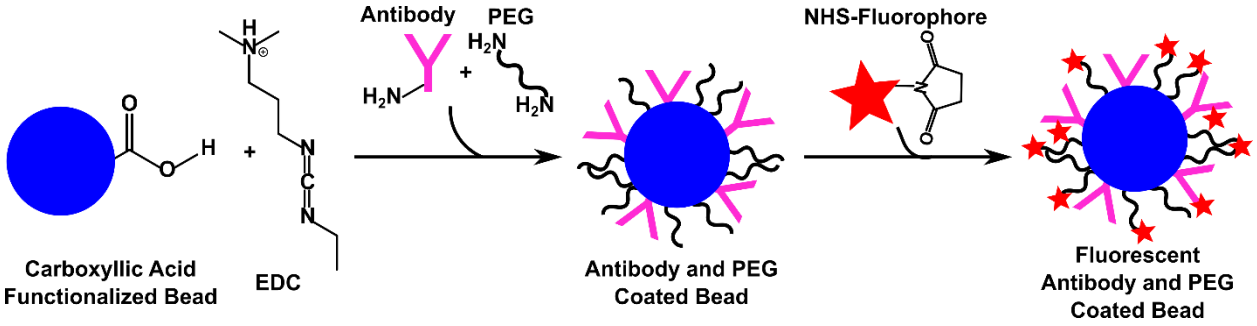

Figure 4.1: Schematic representation of bead functionalization.

First, the carboxylic acid must be functionalized to an activated ester by the addition of 1-ethyl-3-(-3-dimethylaminopropyl) carbodiimide (EDC), this can then react with primary amines. This reaction forms a covalent amide bond between the bead and the amine-containing compound. In this case the amine is primarily found on free lysine residues within the antibody structure. As these residues are prevalent in all proteins, the antibody can be customized to the specific analyte of interest making the platform flexible. The PEG was also bifunctionalized with amines on the end to take advantage of the same chemistry. Coating particles in PEG is a common technique to avoid detection by the immune system.[38,39] The PEG changes the surface chemistry of particles, making them more hydrophilic and therefore less likely to be picked up by phagocytic cells like dendritic cells and macrophages.[44] We chose the 20 kDa PEG as it was a similar length to an antibody. This should prevent the PEG from blocking the binding sites while still allowing for the chemical advantages associated with PEGylation of particles.

To confirm the coating of the beads we used secondary antibodies to detect the presence of the antibody of interest. The secondary antibody intensity was measured by plate reader and

normalized to the fluorescence intensity of the beads. We measured a significant difference between samples with and without the secondary detection antibody only in samples with the primary antibody added (Figure 4.2). Beads with no primary antibodies added had no significant difference after the addition of the detection antibody. This confirmed that the antibodies of interest and fluorophores were successfully bonded to the surface of the beads and should be completed with each functionalization reaction. Once these beads were confirmed to be coated successfully the next step was to ensure that the beads could be visualized in tissue.

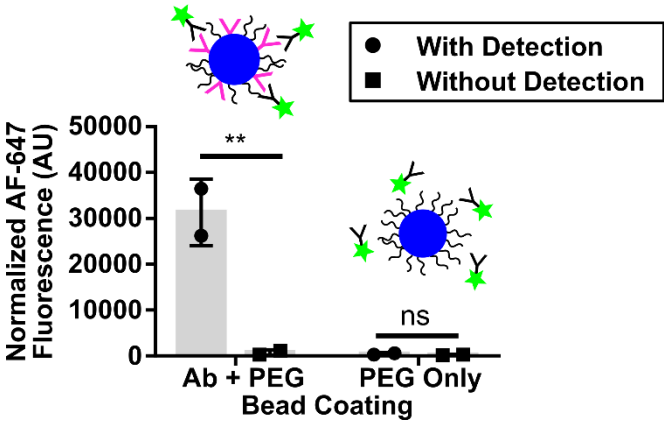

Figure 4.2: Magnetic beads were successfully coated with antibodies. Significant signal was only measured in samples with both coated antibody and secondary antibody. Secondary antibody signal was normalized to the intensity of bead fluorescence. Two-way ANOVA with multiple comparisons. **p<0.001 ns denotes p>0.05

4.3.2 Visualizing magnetic beads

The free amines available on the PEG and additional amines on the antibodies allows the addition of a fluorophore by N-hydroxysuccinimide (NHS) conjugation chemistry. The choice of fluorophore is very important to avoid high background and tissue damage.[45] The short wavelengths, near the ultraviolet range of the spectrum, required to excite common blue fluorophores can cause damage to the tissue, resulting in changes in biology.[46] Green fluorophores are very common, but suffer from high autofluorescence within the tissue.[47–49] Fluorophores in the near-IR range result in less autofluorescence, therefore they are common for low intensity signals.[10,50] We chose a fluorophore that has a large stokes shift to minimize tissue autofluorescence, while keeping the traditional fluorescent channels (blue, green, red, and near-IR) for additional labels.

One technique to achieve long stokes-shifts in is the use of tandem dyes. Tandem dyes use fluorescent energy resonance transfer (FRET) to shift the overall emission to longer wavelengths.[51] However, some protein-based dyes exhibit natural long stokes shifts such as PerCP.[52] Both tandem and protein dyes are not appropriate to include in tissue as they are bulky and would exhibit limited diffusion within the tissue matrix. The dye we chose was Chromeo494, a small molecule fluorophore that excites at 488 nm and emits in the 600 nm range (Figure 4.3).

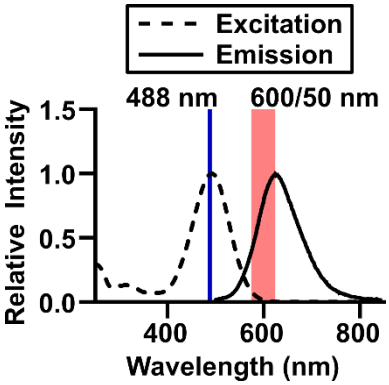

Figure 4.3: Excitation and emission of Chromeo494. The dye is excited with a 488 nm laser and is measured in the 600/50 nm detector.

4.3.3 Large-Diameter Beads were Excluded from Complex Matrices

We determined that characterizing the distribution of the beads was a crucial step to determining the viability of an in-tissue-bead-based immunoassay platform. Once the beads were deemed an acceptable assay platform, the ability of the conjugated beads to successfully detect the analyte of interest could be confirmed. The antibody can be customized to change the bead's specificity, so functionality would need to be confirmed for each analyte but the distribution of the beads would remain the same. Additionally, the beads could be used as a platform for other reactive species, beyond antibodies.[53,54]

The beads we chose were magnetic to facilitate delivery to tissue. Without help particles would just rest on the tissue surface, due to the dense structure of cells and extracellular matrix. The magnet ensured a uniform delivery across the sample. Centrifugation was also considered but due to the relatively light density of the beads the speeds required to embed them in the tissue would result in damage to the tissue itself. In order to determine the best size for delivery to tissue

we varied the diameter of the functionalized beads and delivered them to a model matrix, a 4% agarose slice.

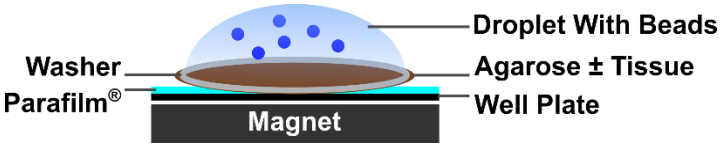

Figure 4.4: Schematic representation of magnetic bead delivery.

The magnets were placed in a custom holder that aligned with a 24-well plate. The remaining set-up was the same as the published procedure for live immunostaining (Figure 4.4).[14] Agarose slices, containing tissue or not, were placed on top of a parafilm-covered well plate. Washers were placed on top of the slice and the bead mixture was added to the top. These slices were then placed on top of the magnet holder and exposed for 20 minutes.

Once delivered to the agarose slice the beads were imaged by fluorescence microscopy and the number of beads were counted. The counts of the 1.00-, 4.67-, and 6.68-μm diameter beads were not significantly different than the no-bead control (Figure 4.5a). This shows that the larger diameter beads are excluded from the matrix because of the close structure. If the larger beads were forced to penetrate the matrix there would likely be damage to the tissue, and so were not considered further.

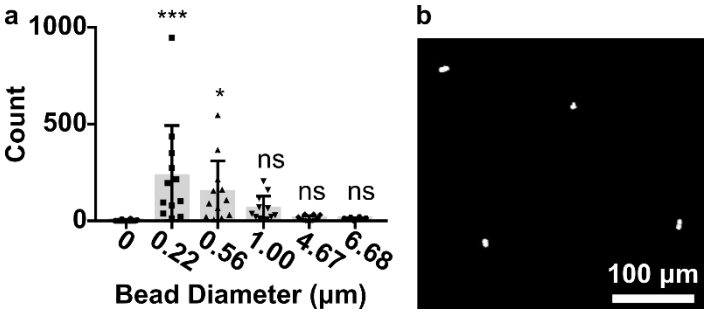

Figure 4.5: Large diameter beads are excluded from agarose. (a) Different diameter beads were delivered to 4% agarose slices. Objects were then counted within multiple fields of view. The 0.22- and 0.56-μm diameter had significantly higher counts than the no-bead blank. The 4.67- and 6.68-μm beads were excluded from the matrix and were not significantly different from the no-bead control. One-way ANOVA with multiple comparisons to the no-bead control (0) ***$p<0.001$ *$p<0.05$ ns denotes $p>0.05$. (b) Visualization of 1.00-μm diameter beads. Individual smaller beads are more difficult to discern.

The smaller beads, 0.56- and 0.22-μm diameter, had significantly higher counts than the no-bead control, but they do suffer from visual artifacts. The small diameter of these beads meant that visualization by microscopy was difficult. The 1.00-μm diameter beads were already difficult to visualize with the widefield microscope (Figure 4.5b). The size of objects that can be discerned from each other is determined, in part, by the numerical aperture of the objective.[55] As the numerical aperture increases the size of objects that can be visualized decreases.[56] Even with our highest numerical aperture objective individual beads with this small diameter would not able to be imaged accurately. The high counts of the smaller beads would seem to indicate that these beads would be more effective when delivered to tissue. However, these beads would only be able to be visualized in aggregates. Aggregated beads could artificially increase the detected signal in a single area and are more easily up-taken by phagocytic cells. Additionally, we would not want to bind all the secreted protein in the area, as this could affect the biological function.

The 1.00 μm diameter beads were chosen for further characterization. The counts were not significantly different than the no-bead control, but were still higher than the larger diameters. These beads were also more accurately and easily visualized than the smaller diameter beads.

4.3.4 PEGylation Increases Bead Distribution Within the Tissue Matrix

In order to achieve an accurate picture of analyte secretion across the tissue it is important to disperse the beads as evenly across the tissue slice as possible. We determined that the addition of PEG to the beads is crucial to evenly distribute the beads throughout the tissue, mainly through avoiding aggregate formation. As mentioned earlier, bead aggregates within the tissue can alter the signal overall. Bead aggregates would also not be evenly distributed across the tissue, and result in an artificial increase in signal in certain areas of the tissue.

To ensure that the beads within the tissue were not aggregating 1.00-μm diameter beads were coated either with the non-reactive antibody alone, or mixed in equal molar ratio with 20 kDa PEG. The area of each object within the tissue was then determined. Beads coated with antibody

alone had a much wider distribution of measured area than the antibody and PEG coated beads (Figure 4.6a). This wider distribution indicated different sized aggregates collecting within the tissue. The antibody and PEG coated beads had a much narrower, and smaller, distribution of areas. This indicated that the beads were more separated and could be more dispersed throughout the tissue. The geometric mean of the area of the antibody and PEG coated beads was 2.98 μm^2, this is much higher than the expected area (0.79 μm^2) but much smaller than 5.69 μm^2, the geometric mean of the antibody only coated beads. This discrepancy between the measured and expected area could be due to the camera resolution. If a bead is within two different pixel bins, once averaged the entire measured area would be increased. The apparent size of the beads was decreased and fewer aggregates were easily identifiable, so we determined that the distribution of PEGylated beads compared to antibody only coated beads was worth exploring further.

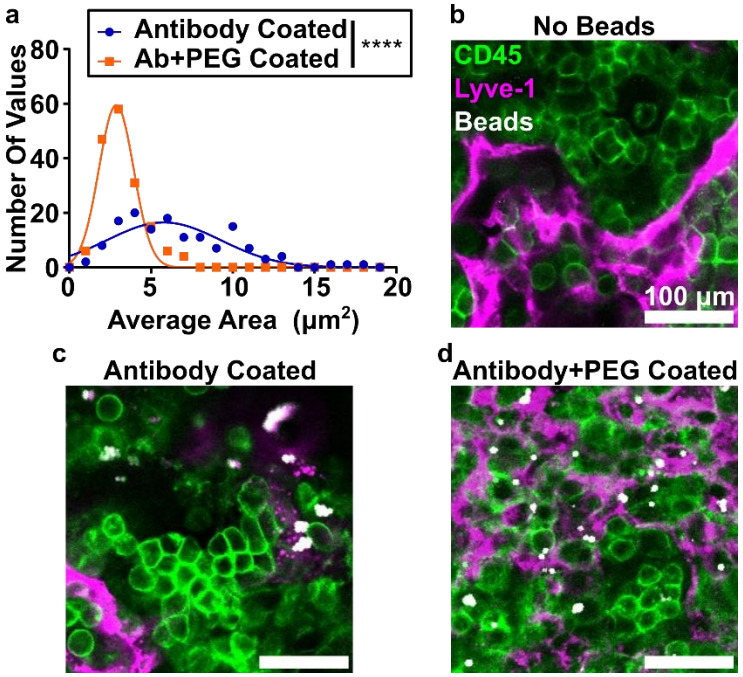

Figure 4.6: PEGylation inhibits aggregate formation in tissue. (a) Measured area of 1.00-μm beads that were delivered to stained tissue slices. A single bead would have an area of 0.79 μm^2. The addition of the PEG shifted the majority of the averages to below 5 μm^2. Student's T test N=6-7 slices, ****p<0.0001. (b-d) Tissue sections stained with AF488 CD45 (green) and eFluor660 Lyve-1 (pink) for the (b) no-bead control (c) antibody only coated beads and (d) antibody and PEG coated beads. The antibody and PEG coated beads appeared much smaller and more separated than the antibody coated beads. Many of the beads were closely aligned with the lymphatic vessels.

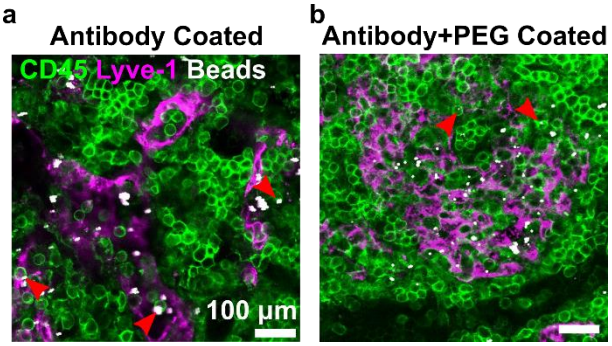

Figure 4.7: Beads delivered to tissue were not phagocytosed. (a) Antibody coated beads aggregated into large artifacts. (b) Antibody and PEG coated beads were smaller and spread throughout the tissue. Red arrowheads indicate cells that have phagocytosed beads.

The long stokes-shift dye conjugated to the beads allowed for very clear, distinct, objects to be visualized against the tissue background (Figure 4.6 b-d). Large aggregates of beads were easily visualized within the tissue and left large portions of the tissue empty (Figure 4.6b, Figure 4.7a). The antibody and PEG coated beads were more evenly distributed throughout the tissue interior (Figure 4.6 c, Figure 4.7b). All the delivered beads were closely aligned with the lymphatic vessels (Figure 4.6c,d). These lymphatic vessels are lined with highly phagocytic cell types such as macrophages and dendritic cells.[33,57] Closer examination of these beads within the tissue revealed that very few beads were being phagocytosed by the lymphocytes (Figure 4.7, red arrowheads).

The beads could have avoided uptake by two different mechanisms. The antibody-only coated beads were aggregated to large enough objects that the cells could not phagocytose them completely. The antibody and PEG coated beads were smaller in diameter, and therefore more able to be phagocytosed, but the PEG prevented uptake by changing the surface chemistry of the particles.[44]

The beads associating with the lymphatic vessels may be due to an increase in the free space within the reticular network along these vessels. Areas with densely packed cells did not have as many beads in that area (Figure 4.7*).* Anchoring an assay platform around the lymphatic vessels could be beneficial as secretions from migrating cells would be held in place. This could allow us to interrogate the state of secreted proteins from incoming cells, or highly motile cell types. However, denser areas such as the T-cell rich paracortex and the B cell follicles would not be easily investigated with this assay platform in its current form.

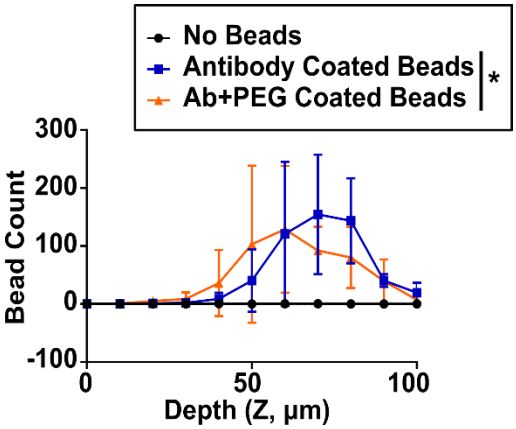

Figure 4.8: Magnetic beads were embedded within the tissue matrix. Serial images of lymph node slices were collected and beads were counted at each slice. Both antibody only and antibody-PEG coated beads penetrated beyond the first layer of the tissue. One-way ANOVA with multiple comparisons. N=5-7 slices *p=0.0127

The distribution of the beads throughout the depth of the tissue section is as important as the x,y distribution. If the beads are merely sitting on top of the tissue there is the risk of them being washed away during handling, and therefore not effectively acting as an anchor within the tissue. Antibodies alone penetrate at least 50 µm into the tissue.[14] Ideally, the beads would be at a similar depth so that their location and corresponding signal intensity can be accurately matched to structural mapping antibodies. Images were collected at defined steps within the tissue slice and the beads at each level were counted (Figure 4.8). The shape of the distributions was similar between the antibody only and antibody and PEG coated beads. This data means that both beads were able to penetrate into the tissue. Beads within the first 10s of microns were easily washed away during handling, resulting in very low counts near the surface of the tissue slices. There was a large amount of variability between the counts at the same levels of different tissue slices. This was most likely due to differences in the tissue structure in different organ sections.[29]

The curve for the antibody and PEG coated beads had a more gradual increase to its peak, the antibody only beads had a sharp increase from 60 to 70 µm from the surface of the tissue. The flatness of the antibody and PEG coated bead curve adds to the data that the PEGylated beads are more evenly distributed throughout the tissue.

The antibody only coated beads had a maximum count that was 20 µm deeper than the antibody and PEG coated beads. As characterized previously, antibody only coated beads easily form aggregates. We hypothesized that these aggregates could form within the delivery solute

increasing the apparent mass of the beads. If the heavier aggregates sank closer to the surface of the tissue before the magnetic field was applied this may have allowed them to penetrate deeper than the smaller antibody and PEG coated beads in the same time. Overall, these data show that the beads would not be easily washed away with handling as they are embedded within the tissue, not just resting on its surface.

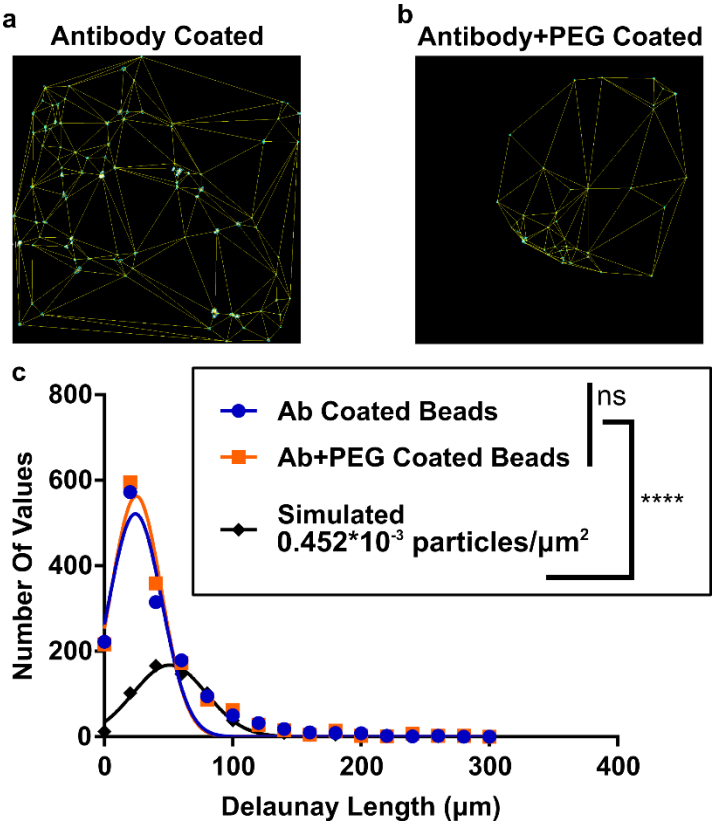

Figure 4.9: Beads were distributed non-randomly within the tissue matrix. (a-b) Representative images of Delaunay measurements for antibody only (a) and antibody and PEG (b) coated beads. (c) Histogram of Delaunay lengths between adjacent particles. Random distribution matched in concentration to average beads per image. One-way ANOVA with multiple comparisons. N=5-7 slices ****p<0.0001, n.s. denotes p>0.05.

The last metric we used to describe the distribution of beads within the tissue was the Delaunay length.[58] This allowed us to describe the distribution within the tissue slice. Delaunay triangulation calculate the smallest possible triangle that can connect three points (Figure 4.9a,b).[41,58] We set the location of the beads as our coordinate points. The lengths of each arm of the triangles was then plotted as a histogram. We compared the bead distribution to a randomly generated set of coordinates. The average concentration of beads per image was matched between the experimental and simulated conditions.

This measurement allowed us to discern if the beads were being delivered to the tissue in a random manner, or in a more organized way. The randomly generated coordinates had a significantly different distribution than either of the experimental samples (Figure 4.9c). Meaning

that both bead schemes were delivered in a non-random manner. There was no significant difference between the distributions of the antibody only and the antibody and PEG coated beads. This is most likely due to the uniform magnetic field felt by the entire area of the slice and the structure of the tissue itself. Rather than an artifact of the bead such as size or hydrophobicity.

Tissue organization is a highly regulated event and for it to result in a truly random distribution of space would be very surprising.[59] A truly random distribution of beads within the tissue would not be beneficial to the end goal of measuring analytes with spatial precision. This is because a random distribution would introduce sample-to-sample variability beyond biological variability. A non-random distribution ensures that data collected across multiple samples can be more easily compared.

These data show that PEGylation was an important component to the successful delivery of beads to lymph node tissue. PEGylation decreased the apparent size of the beads delivered to tissue, compared to antibody only coated beads. The addition of the PEG also prevented phagocytosis by immune cells. Visually, both types of beads clustered around lymphatic vessels but the antibody and PEG coated beads were more distributed throughout the tissue. PEGylated beads were also more evenly distributed in the z direction than the antibody only beads.

4.4 Conclusions and Future Work

This chapter detailed the early characterization of a bead-based in-tissue assay platform. Carboxylic acid functionalized beads were coated with non-reactive antibodies and 20 kDa polyethylene glycol (PEG). Beads were then reacted with a small-molecule fluorescent dye that had a long stokes shift. Magnetic beads were chosen for delivery to tissue samples because the delivery was could be well-controlled and evenly distributed. The addition of PEG was crucial to evenly distribute singular beads throughout the tissue. PEGylation reduced aggregation and increased the visual distribution of the beads in all directions within the lymph node tissue.

Delivery of beads was not randomly dispersed in the tissue, but was localized to areas near lymphatic vessels.

In order to utilize this platform in tissue the next step would be to validate that the beads can function as an immunoassay platform. Meaning the beads should be able to detect the analyte of interest. Preliminary work with IL-2 resulted in inconsistent signal with smaller beads. This could indicate that either the antibody:PEG ratio or mechanism of adding the fluorophore needs to be optimized. If there was too much PEG, or if the number of fluorophores was too high, this could interfere with the binding of analytes and the detection antibody to the bead surface. An antibody pair with very high selectivity and sensitivity would be ideal as the relevant analytical range within a given area of the tissue for many cytokines is unknown.[23]

The bead platform would function as the base for the sandwich immunoassay, similar to the plate in an ELISA. This would require delivery of a second fluorescent detection antibody to visualize the relative quantity of analyte in the tissue. A true qualitative calibration curve would be difficult to calculate as subtle changes throughout the tissue could affect the overall signal. A semi-quantitative assay, where relative expression is measured, would be more feasible and easily reproducible. The detection antibody should be modified to remove the Fc tail. This will reduce non-specific binding and immune activation by removing the interactions with Fc receptors on immune cells.[60,61]

This platform can be customized by choosing specific clones of antibodies to measure distinct analytes. Based on their location near the lymphatic vessels these beads could act as an anchored platform for secretions from highly motile cell types. As cells enter the lymph node near the lymphatic vessel they then migrate throughout the tissue. The beads would be stationary and could inform on the state of cells as they enter the lymph node. Investigating the state of the tissue deeper in the cell-dense regions such as the paracortex and B cell follicles would be more difficult as the beads did not easily penetrate these areas. Still, mapping these areas through the use of

fluorescent antibodies would be an important step to understanding the detected signals. Lymphatic vessels can run close to B cell follicles or even through the mid-line of the node.[62] Each of these conditions could have distinct secretion patterns, or respond differently to stimuli.[63,64] Monitoring the signal location relative to known structures is an important portion of putting the signal within the biological context.

Looking forward this platform could also carry other types of detectors, other than antibodies. Aptamers, short strands of nucleic acids with very high specificity, are becoming increasingly popular as a detection method.[53,65,66] Synthetic peptides could also be used to detect analytes.[54,67] Some mechanisms also incorporate a FRET-based detection method. These methods involve conformational changes within the structure to separate the fluorophore from a quencher to produce a signal.[68–70] This type of detection can be much more sensitive as it doesn't require the use of a second detection reagent.

A temporal component could be easily added to this platform as old beads could be removed by exposure to the magnet, and new beads added in the same way. There is no guarantee that the new beads would be in exactly the same locations, but with structural mapping the same areas could be investigated over time. This could inform how the tissue changes during an immune response.

Characterizing the distribution of these beads within the tissue was an important first step to customizing an in-tissue immunoassay.

4.5 REFERENCES

1 Genon S, Reid A, Langner R, Amunts K, Eickhoff SB. How to characterize the function of a brain region. *Trends Cogn Sci* 2018; **22**: 350–364.

2 Clevers H. The intestinal crypt, a prototype stem cell compartment. *Cell* 2013; **154**: 274–284.

3 Umar S. Intestinal stem cells. *Curr Gastroenterol Rep* 2010; **12**: 340–348.

4 Grant SM, Lou M, Yao L, Germain RN, Radtke AJ. The lymph node at a glance – how spatial organization optimizes the immune response. *J Cell Sci* 2020; **133**. doi:10.1242/jcs.241828.

5 Knoblich K, Cruz Migoni S, Siew SM, Jinks E, Kaul B, Jeffery HC *et al.* The human lymph node microenvironment unilaterally regulates T-cell activation and differentiation. *PLOS Biol* 2018; **16**: e2005046.

6 Lanzavecchia A, Iezzi G, Viola A. From TCR engagement to T cell activation. *Cell* 1999; **96**: 1–4.

7 Garside P. Visualization of specific B and T lymphocyte interactions in the lymph node. *Science* 1998; **281**: 96–99.

8 Geukes Foppen MH, Rozeman EA, van Wilpe S, Postma C, Snaebjornsson P, van Thienen JV *et al.* Immune checkpoint inhibition-related colitis: symptoms, endoscopic features, histology and response to management. *ESMO Open* 2018; **3**: e000278.

9 Yoshii SR, Mizushima N. Monitoring and measuring autophagy. *Int J Mol Sci* 2017; **18**: 1865.

10 Hilderbrand SA, Weissleder R. Near-infrared fluorescence: application to in vivo molecular imaging. *Curr Opin Chem Biol* 2010; **14**: 71–79.

11 Fuhrmann M, Oertel W, Hegemann P. A synthetic gene coding for the green fluorescent protein (GFP) is a versatile reporter in Chlamydomonas reinhardtii. *Plant J Cell Mol Biol* 1999; **19**: 353–361.

12 Ross AE, Belanger MC, Woodroof JF, Pompano RR. Spatially resolved microfluidic stimulation of lymphoid tissue ex vivo. *The Analyst* 2017; **142**: 649–659.

13 Catterton MA, Dunn AF, Pompano RR. User-defined local stimulation of live tissue through a movable microfluidic port. *Lab Chip* 2018; **18**: 2003–2012.

14 Groff BD, Kinman AWL, Woodroof JF, Pompano RR. Immunofluorescence staining of live lymph node tissue slices. *J Immunol Methods* 2018. doi:10.1016/j.jim.2018.10.010.

15 Budai D. Carbon fiber-based microelectrodes and microbiosensors. *Intell Biosens* 2010. doi:10.5772/7158.

16 Ledo A, Barbosa RM, Frade J, Laranjinha J. Nitric oxide monitoring in hippocampal brain slices using electrochemical methods. In: *Methods in Enzymology*. Academic Press, 2002, pp 111–125.

17 Ao X, Stenken JA. Microdialysis sampling of cytokines. *Methods* 2006; **38**: 331–341.

18 Chefer VI, Thompson AC, Zapata A, Shippenberg TS. Overview of brain microdialysis. *Curr Protoc Neurosci Editor Board Jacqueline N Crawley Al* 2009; **CHAPTER**: Unit7.1.

19 Vasicek TW, Jackson MR, Poseno TM, Stenken JA. In vivo microdialysis sampling of cytokines from rat hippocampus: comparison of cannula implantation procedures. *ACS Chem Neurosci* 2013; **4**: 737–746.

20 Lane JD, Montaigne D, Tinker A. Tissue-level cardiac electrophysiology studied in murine myocardium using a microelectrode array: Autonomic and thermal modulation. *J Membr Biol* 2017; **250**: 471–481.

21 A. Soscia D, Lam D, C. Tooker A, A. Enright H, Triplett M, Karande P *et al.* A flexible 3-dimensional microelectrode array for in vitro brain models. *Lab Chip* 2020; **20**: 901–911.

22 Kellar KL, Kalwar RR, Dubois KA, Crouse D, Chafin WD, Kane B-E. Multiplexed fluorescent bead-based immunoassays for quantitation of human cytokines in serum and culture supernatants. *Cytometry* 2001; **45**: 27–36.

23 Stenken JA, Poschenrieder AJ. Bioanalytical chemistry of cytokines – A review. *Anal Chim Acta* 2015; **853**: 95–115.

24 Buttigieg J, Ali H, Sharma A, Halawa A. Positive Luminex and negative flow cytometry in kidney transplantation: a systematic review and meta-analysis. *Nephrol Dial Transplant* 2019; **34**: 1950–1960.

25 Lynch HE, Sanchez AM, D'Souza MP, Rountree W, Denny TN, Kalos M *et al.* Development and implementation of a proficiency testing program for Luminex bead-based cytokine assays. *J Immunol Methods* 2014; **409**: 62–71.

26 Wu D, Voldman J. An integrated model for bead-based immunoassays. *Biosens Bioelectron* 2020; **154**: 112070.

27 Luminex assay principle. www.rndsystems.com. https://www.rndsystems.com/resources/technical/luminex-assay-principle.

28 Hamsher AE, Xu H, Guy Y, Sandberg M, Weber SG. Minimizing tissue damage in electroosmotic sampling. *Anal Chem* 2010; **82**: 6370–6376.

29 Belanger MC, Kinman AWL, Catterton MA, Ball AG, Groff BD, Melchor SJ *et al.* Acute lymph node slices are a functional model system to study immunity ex vivo. *bioRxiv* 2019; : 865543.

30 Finnerty CC, Herndon DN, Przkora R, Pereira CT, Oliveira HM, Queiroz DMM *et al.* Cytokine expression profile over time in severely burned pediatric patients. *Shock Augusta Ga* 2006; **26**: 13–19.

31 Savina A, Amigorena S. Phagocytosis and antigen presentation in dendritic cells. *Immunol Rev* 2007; **219**: 143–156.

32 Gray EE, Cyster JG. Lymph node macrophages. *J Innate Immun* 2012; **4**: 424–436.

33 Junt T, Moseman EA, Iannacone M, Massberg S, Lang PA, Boes M *et al.* Subcapsular sinus macrophages in lymph nodes clear lymph-borne viruses and present them to antiviral B cells. *Nature* 2007; **450**: 110–114.

34 Champion JA, Walker A, Mitragotri S. Role of particle size in phagocytosis of polymeric microspheres. *Pharm Res* 2008; **25**: 1815–1821.

35 Siepmann J, Faisant N, Akiki J, Richard J, Benoit JP. Effect of the size of biodegradable microparticles on drug release: experiment and theory. *J Control Release Off J Control Release Soc* 2004; **96**: 123–134.

36 Huang P, Wang X, Liang X, Yang J, Zhang C, Kong D *et al.* Nano-, micro-, and macroscale drug delivery systems for cancer immunotherapy. *Acta Biomater* 2019; **85**: 1–26.

37 Mi Y, Hagan CT, Vincent BG, Wang AZ. Emerging nano-/microapproaches for cancer immunotherapy. *Adv Sci* 2019; **6**: 1801847.

38 Jokerst JV, Lobovkina T, Zare RN, Gambhir SS. Nanoparticle PEGylation for imaging and therapy. *Nanomed* 2011; **6**: 715–728.

39 Suk JS, Xu Q, Kim N, Hanes J, Ensign LM. PEGylation as a strategy for improving nanoparticle-based drug and gene delivery. *Adv Drug Deliv Rev* 2016; **99**: 28–51.

40 Schneider CA, Rasband WS, Eliceiri KW. NIH image to ImageJ: 25 years of image analysis. *Nat Methods* 2012; **9**: 671–675.

41 Delaunay Voronoi. ImageJ. https://imagej.net/Delaunay_Voronoi.

42 Lerman MJ, Lembong J, Muramoto S, Gillen G, Fisher JP. The evolution of polystyrene as a cell culture material. *Tissue Eng Part B Rev* 2018; **24**: 359–372.

43 Qu J-B, Xu Y-L, Liu Y, Wang Y, Sui Y, Liu J-G *et al.* Inherently fluorescent polystyrene microspheres for coating, sensing and cellular imaging. *Colloids Surf B Biointerfaces* 2017; **152**: 475–481.

44 Yu SS, Lau CM, Thomas SN, Jerome WG, Maron DJ, Dickerson JH *et al.* Size- and charge-dependent non-specific uptake of PEGylated nanoparticles by macrophages. *Int J Nanomedicine* 2012; **7**: 799–813.

45 Ge J, Wood DK, Weingeist DM, Prasongtanakij S, Navasumrit P, Ruchirawat M *et al.* Standard fluorescent imaging of live cells is highly genotoxic. *Cytom Part J Int Soc Anal Cytol* 2013; **83**: 552–560.

46 Gonçalves MST. Optimized UV/visible fluorescent markers. In: Demchenko AP (ed). *Advanced Fluorescence Reporters in Chemistry and Biology I: Fundamentals and Molecular Design*. Springer Berlin Heidelberg: Berlin, Heidelberg, 2010, pp 27–64.

47 Van de Lest CH, Versteeg EM, Veerkamp JH, Van Kuppevelt TH. Elimination of autofluorescence in immunofluorescence microscopy with digital image processing. *J Histochem Cytochem* 1995; **43**: 727–730.

48 Croce AC, Bottiroli G. Autofluorescence spectroscopy and imaging: A tool for biomedical research and diagnosis. *Eur J Histochem EJH* 2014; **58**. doi:10.4081/ejh.2014.2461.

49 Rosal B del, Benayas A. Strategies to overcome autofluorescence in nanoprobe-driven in vivo fluorescence imaging. *Small Methods* 2018; **2**: 1800075.

50 Hong G, Antaris AL, Dai H. Near-infrared fluorophores for biomedical imaging. *Nat Biomed Eng* 2017; **1**: 0010.

51 Jensen IJ, McGonagill PW, Lefebvre MN, Griffith TS, Harty JT, Badovinac VP. Worry and FRET: ROS production leads to fluorochrome tandem degradation and impairs interpretation of flow cytometric results. *Immunity* 2020; **52**: 419–421.

52 Niki H, Hosokawa S, Nagaike K, Tagawa T. A new immunofluorostaining method using red fluorescence of PerCP on formalin-fixed paraffin-embedded tissues. *J Immunol Methods* 2004; **293**: 143–151.

53 Tombelli S, Minunni M, Mascini M. Analytical applications of aptamers. *Biosens Bioelectron* 2005; **20**: 2424–2434.

54 Wang P, Liu L, Zhou P, Wu W, Wu J, Liu W *et al.* A peptide-based fluorescent chemosensor for multianalyte detection. *Biosens Bioelectron* 2015; **72**: 80–86.

55 Zhang Q, Dong F, Li H, Wang Z, Liang G, Zhang Z *et al.* High-numerical-aperture dielectric metalens for super-resolution focusing of oblique incident light. *Adv Opt Mater*; **n/a**: 1901885.

56 Numerical aperture and image resolution. Nikon's Microsc. https://www.microscopyu.com/tutorials/imageformation-airyna.

57 Bellomo A, Gentek R, Bajénoff M, Baratin M. Lymph node macrophages: Scavengers, immune sentinels and trophic effectors. *Cell Immunol* 2018; **330**: 168–174.

58 Reese BE. 1.22 - Mosaics, tiling, and coverage by retinal neurons. In: Masland RH, Albright TD, Albright TD, Masland RH, Dallos P, Oertel D *et al.* (eds). *The Senses: A Comprehensive Reference*. Academic Press: New York, 2008, pp 439–456.

59 Blum KS, Pabst R. Keystones in lymph node development. *J Anat* 2006; **209**: 585–595.

60 Swanson JA, Hoppe AD. The coordination of signaling during Fc receptor-mediated phagocytosis. *J Leukoc Biol* 2004; **76**: 1093–1103.

61 Luo Y, Pollard JW, Casadevall A. Fcγ receptor cross-linking stimulates cell proliferation of macrophages via the ERK pathway. *J Biol Chem* 2010; **285**: 4232–4242.

62 Ohtani O, Ohtani Y. Recent developments in morphology of lymphatic vessels and lymph nodes. *Ann Vasc Dis* 2012; **5**: 145–150.

63 Bovay E, Sabine A, Prat-Luri B, Kim S, Son K, Willrodt A-H *et al.* Multiple roles of lymphatic vessels in peripheral lymph node development. *J Exp Med* 2018; **215**: 2760–2777.

64 Girard J-P, Moussion C, Förster R. HEVs, lymphatics and homeostatic immune cell trafficking in lymph nodes. *Nat Rev Immunol* 2012; **12**: 762–773.

65 Guthrie JW, Hamula CLA, Zhang H, Le XC. Assays for cytokines using aptamers. *Methods* 2006; **38**: 324–330.

66 Sefah K, Phillips JA, Xiong X, Meng L, Simaeys DV, Chen H *et al.* Nucleic acid aptamers for biosensors and bio-analytical applications. *Analyst* 2009; **134**: 1765–1775.

67 Sharma V, Wang Q, Lawrence DS. Peptide-based fluorescent sensors of protein kinase activity: Design and applications. *Biochim Biophys Acta BBA - Proteins Proteomics* 2008; **1784**: 94–99.

68 Nutiu R, Li Y. Structure-switching signaling aptamers. *J Am Chem Soc* 2003; **125**: 4771–4778.

69 Coleman RA, Trader DJ. Development and application of a sensitive peptide reporter to discover 20S proteasome stimulators. *ACS Comb Sci* 2018; **20**: 269–276.

70 Cummings RT, Salowe SP, Cunningham BR, Wiltsie J, Park YW, Sonatore LM *et al.* A peptide-based fluorescence resonance energy transfer assay for Bacillus anthracis lethal factor protease. *Proc Natl Acad Sci* 2002; **99**: 6603–6606.

5 FINAL REMARKS

5.1 CONCLUSIONS

In this dissertation I have detailed the foundational work for developing novel analytical platforms to study immunity. As detailed in **Chapter 1** immunity is a systemic combination of many cell types that work to clear pathogens from the host. In order to fully understand the chemical signals required to initiate and fulfill a successful immune response we must look closely at the lymph node, a secondary organ of the immune system where much of the adaptive immune response is generated. Measuring these signals within the spatial organization of the tissue will provide a greater biological context and be more accurate to *in vivo* models.

In **Chapter 2** I characterized the use of live slices of murine lymph node tissue as a platform to study immunological functions. Lymph nodes were embedded in agarose and sliced on a vibratome. The slices that were collected were viable and able to report on immunological functions. These tissue slices are the foundation for the rest of the work in this thesis. By developing this platform as an acute method to study immunity we are able to visualize dynamics within the tissue with standard microscopy read-outs.

Chapter 3 described the optimization of a novel cell labelling reagent to visualize cell dynamics. This work was completed in collaboration with the Fraser lab at UVA. Nanoparticles fabricated from different polymers and containing a boron-based fluorophore were delivered to lymphocytes for labelling. Phagocytic cells were more effectively labelled with these nanoparticles, and the labelling process did not affect cell viability or function. The cells labelled with the nanoparticles exhibited bright blue fluorescence and were easily visualized against the tissue background with the DAPI filter set. This nanoparticle-based labeling method would allow for more effective use of the remaining filter sets in a traditional fluorescent microscope.

In **Chapter 4** the beginnings of a bead-based in-tissue immunoassay were discussed. Magnetic polystyrene beads were functionalized with antibodies, polyethylene glycol (PEG), and a long stokes shift small molecule dye. The distribution of the functionalized beads within the lymph node tissue was characterized. PEG was essential to achieving an even distribution of the beads within the tissue. These beads would be able to act as a stationary surface for an analytical immunoassay within the tissue matrix.

Overall, this work sets the foundation for future investigations into the dynamics of immune signaling within the lymph node.

5.2 FUTURE DIRECTIONS

A future goal of using the lymph node slices would be to monitor and characterize a full immune response from initiation to antibody formation. As the immune response can take up to a week to fully develop the ability to culture these slices long-term is an important consideration. One concern with long-term culture of lymph node tissue is the motility of the lymphocytes. Cell exodus from the slices has been observed, especially after 48 hours of culture. We hypothesize that the lymphocytes are exiting the tissue due to a lack of retention signals rather than responding to an “exit” signal. One target for this signal is CCL21, a chemokine expressed by the stromal cells that is crucial for the development and organization of the paracortex of the lymph node.[1] Production of this chemokine can be induced by fluid flow within the tissue.[2] Future work with this project includes the development of a gravity-driven fluid flow culture platform to help induce CCL21 expression. The addition of fluid flow is more appealing than simply supplementing the media with CCL21 because the fluid flow is closer to the *in vivo* environment. However, media supplementation should also be considered to maintain cell viability.

Labelling the lymphocytes with nanoparticles to study their dynamics within the lymph node would allow for facile cell-tracking in the blue fluorescence channel. Future applications of this labelling reagent, in its current form, would focus on the dynamics of B cells within the germinal

center. B cells were effectively labelled with these nanoparticles, so tracking B cell motility as they move through the different areas of a germinal center would be a natural transition. A long-lived labelling mechanism could also be investigated to prevent the dye from being broken down or exported by the cells. This would require modifying the surface of the nanoparticles, potentially with a reactive ester group. This group would interact with active esterases within the cells to add a charge to the particle and prevent exit through the cell membrane. Adjusting the surface of the nanoparticle could also help to target different cell types, such as T cells, in the future.

The embedded beads in tissue would act as a spatially-defined immunoassay platform in the future. With this platform the signals from the lymphatic vessels can be measured in response to different stimulants. Stimulants such as lipopolysaccharide (LPS) would result in activation of the more innate-like cells that line the lymphatic vessels.[3,4] Cell-specific stimulants, such as T cell receptor binding, would result in a different response in the same areas. With a live slice platform, not only can secreted signals be placed in their spatial context, but also in time with the inclusion of repeated measures. Different surface chemistries or delivery mechanics can also be applied in an attempt to change the distribution of the beads. In order to get the beads in areas of the tissue that are denser a longer exposure with the magnet could be beneficial. Changing the surface chemistry to be slightly hydrophobic could help the beads penetrate to areas with a high lipid content, such as dense areas of cell membranes. This would have to be tested with high precision to avoid bead-uptake by the cells.

In the future, these platforms can be used to investigate signaling dynamics within the lymph node during the immune response. Current focus of the Pompano lab has been on the effect of different vaccine adjuvants on the immune response. Adjuvants are components of vaccines that initiate the response against the antigen.[5] However, as immunology, as a field, progresses I anticipate more questions about lymph node dynamics to be asked. Our slices would be a crucial platform to analyze these dynamics in a meaningful way.

Monitoring genetic profiles over development and implementation of immune responses has informed a new wave of immunological understanding. Fate mapping has allowed immunologists to track the origin of cells during development.[6–8] Epigenetics has elucidated the elasticity of the immune system showing how the immune system can change over time.[9–11] These approaches have allowed immunologists to determine the source of many circulating cells. This kind of data would not be collected in our slice platform. The fate mapping requires genetic modification, which we could monitor in our slices but the data collected in an *in vivo* setting is much more informative. Epigenetics requires access to the interior of the cells that would not be accessible in a live tissue setting. However, the information generated by these data will give us a greater understanding of how cells populate and further change within the lymph node. Which will allow us to generate more complete hypotheses about cellular profiles. Moving into tissue would allow for a further understanding of how the spatial distribution of these cells can change and will influence the response.

Immunologists have also increased the data load by moving to single-cell resolution including single cell cytokine expression[12–14] and gene expression analysis.[15–17] These data have allowed new connections between cell types to be determined and explored. Further understanding of how cells change during an immune response may allow the Pompano lab to generate more complete hypotheses. However, as we move up in complexity from single cells to tissue, we do expect to measure distinct differences. These large data sets will more likely inform our understanding of immunology on a large scale but not the specific cellular interactions. These interactions are what the Pompano lab is more interested in observing.

I expect the Pompano lab to take advantage of new advances in technology, especially in the field of microscopy. As more sensitive detectors and precise light sources become readily available interactions within the tissue will be easier to measure with high precision. The high cell density and complex cell matrix can make isolating cellular interactions from one another difficult.

Immune cells can also be in complex shapes, making the identification of cells such as dendritic cells problematic. These two artifacts of imaging may be solved with increased resolution and the addition of more stains; both of which could be introduced with more complex microscopes.

Deconvolution of widefield images can improve the signal to noise ratio and clarify structures within the tissue.[18] Images of the spatial distribution of signals collected with low magnification could be analyzed with confocal-like resolution. These experiments also generate large quantities of data. As computers are able to handle large data sets with increasing ease analyzing this data will become easier as well.

In conclusion, this work provides the foundation for many new investigations within the Pompano Lab. I have high hopes for the future of this research.

5.3 REFERENCES

1 Lian J, Luster AD. Chemokine-guided cell positioning in the lymph node orchestrates the generation of adaptive immune responses. *Curr Opin Cell Biol* 2015; **36**: 1–6.

2 Tomei AA, Siegert S, Britschgi MR, Luther SA, Swartz MA. Fluid flow regulates stromal cell organization and CCL21 expression in a tissue-engineered lymph node microenvironment. *J Immunol* 2009; **183**: 4273–4283.

3 Poltorak A. Defective LPS Signaling in C3H/HeJ and C57BL/10ScCr mice: Mutations in Tlr4 gene. *Science* 1998; **282**: 2085–2088.

4 Junt T, Moseman EA, Iannacone M, Massberg S, Lang PA, Boes M *et al.* Subcapsular sinus macrophages in lymph nodes clear lymph-borne viruses and present them to antiviral B cells. *Nature* 2007; **450**: 110–114.

5 Mosca F, Tritto E, Muzzi A, Monaci E, Bagnoli F, Iavarone C *et al.* Molecular and cellular signatures of human vaccine adjuvants. *Proc Natl Acad Sci* 2008; **105**: 10501–10506.

6 Poltorak MP, Schraml BU. Fate mapping of dendritic cells. *Front Immunol* 2015; **6**. doi:10.3389/fimmu.2015.00199.

7 Yona S, Kim K-W, Wolf Y, Mildner A, Varol D, Breker M *et al.* Fate mapping reveals origins and dynamics of monocytes and tissue macrophages under homeostasis. *Immunity* 2013; **38**: 79–91.

8 Legue E, Joyner AL. Genetic fate mapping using site-specific recombinases. *Methods Enzymol* 2010; **477**: 153–181.

9 Dunn J, Rao S. Epigenetics and immunotherapy: The current state of play. *Mol Immunol* 2017; **87**: 227–239.

10 Li G, Zan H, Xu Z, Casali P. Epigenetics of the antibody response. *Trends Immunol* 2013; **34**: 460–470.

11 Suárez-Álvarez B, Baragaño Raneros A, Ortega F, López-Larrea C. Epigenetic modulation of the immune function. *Epigenetics* 2013; **8**: 694–702.

12 Saxena A, Dagur PK, Desai A, McCoy JP. Ultrasensitive quantification of cytokine proteins in single lymphocytes from human blood following ex-vivo stimulation. *Front Immunol* 2018; **9**. doi:10.3389/fimmu.2018.02462.

13 Ogunniyi AO, Thomas BA, Politano TJ, Varadarajan N, Landais E, Poignard P *et al.* Profiling human antibody responses by integrated single-cell analysis. *Vaccine* 2014; **32**: 2866–2873.

14 Varadarajan N, Julg B, Yamanaka YJ, Chen H, Ogunniyi AO, McAndrew E *et al.* A high-throughput single-cell analysis of human CD8+ T cell functions reveals discordance for cytokine secretion and cytolysis. *J Clin Invest* 2011; **121**: 4322–4331.

15 Hwang B, Lee JH, Bang D. Single-cell RNA sequencing technologies and bioinformatics pipelines. *Exp Mol Med* 2018; **50**: 1–14.

16 Gaublomme JT, Yosef N, Lee Y, Gertner RS, Yang LV, Wu C *et al.* Single-cell genomics unveils critical regulators of Th17 cell pathogenicity. *Cell* 2015; **163**: 1400–1412.

17 Kalisky T, Quake SR. Single-cell genomics. *Nat Methods* 2011; **8**: 311–314.

18 Lee J-S, Wee T-L (Erika), Brown CM. Calibration of wide-field deconvolution microscopy for quantitative fluorescence imaging. *J Biomol Tech JBT* 2014; **25**: 31–40.